1-1-2005

A study of bubble entrainment as related to runner velocity in aluminum sand castings using the Cosworth process.

John C. Burford
University of Windsor

A Study of Bubble Entrainment as Related to Runner Velocity in Aluminum Sand Castings using the Cosworth Process

By

John C. Burford

A Thesis
Submitted to the Faculty of Graduate Studies and Research
Through Engineering Materials in Partial Fulfilment of the
Requirements for the Degree of Master of Applied Science at the
University of Windsor

Windsor, Ontario Canada

2005

Your file Votre référence
ISBN: 978-0-494-57558-1
Our file Notre référence
ISBN: 978-0-494-57558-1

Abstract

Traditional gravity pour down-sprue methods of filling moulds in the making of aluminum castings inherently lead to oxide and air bubble entrainment. The reason for this is found in the high velocities the metal flow experiences during the filling of a mould. The Nemak Windsor Aluminum Plant (WAP) produces 3.0L aluminum cylinder blocks using the low-pressure Cosworth process, which includes low velocity up-hill filling of the sand mould. This doctrine is followed in all except one part of the process: the runner system. The nature of the resulting defect is generally bubbles known as Head Deck Porosity. A solution to this issue represents a substantial economic opportunity.

The current research deals directly with the design of the running system and the speed at which it is filled. Runner samples were cast in open WAP 3.0L production runners at three different velocities, with the resulting quickly chilled castings analyzed using X-ray radioscopy, tensile testing and Scanning Electron Microscopy. Results reveal that the subject bubble porosity is indeed the result of air entrained during initial transient flow within the production runner system whose velocity is higher than the critical value of $0.5ms^{-1}$. This theoretical value is corroborated by experimental results. In addition, a new "sessile" runner of optimized shape, filled at a velocity slower than the critical value, is proposed and analyzed using Magmasoft mould fill modelling software. This design can potentially replace the existing runner design, providing a casting fill system free of entrained air thereby reducing or possibly eliminating the quantity of scrap due to head deck porosity.

Dedication

To God, to the love of my life Pam, to my precious children Marie, Christopher and Amanda, and to my wonderful parents Catherine and George...

Thank you for your love and support.

Acknowledgements

To Dr. Jerry Sokolowski, thank you for your enthusiastic optimism and firm belief in this project, and to Ellen Moosberger thank you for both your critique of this manuscript and the thorough, timely answers you always provide.

Thanks also to Nemak of Canada Inc. for their financial support and access to production equipment in order to conduct this research, and to the staff at the Nemak Engineering Centre; Long Dinh, Bao Tran, Austin Letcher, Bob Patrick, Ben Lane, Tariq Malik, Andy Rivera, Maria Grenados, Antonietta Vespa, Anthony LaPorta and Dr. Robert MacKay for their eager assistance with experimentation, tooling modifications and sample preparation and evaluation.

Thanks to the Ford Motor Company Casting Division Simulation Team of Eban Prabhu and Anthony Canestrelli for the high quality Magma simulation work they performed.

Thanks to Dr. W. Kasprzak for his advice and expert SEM analysis, and to Dr. G. Byczynski for the inspiration required to attempt such a project as this.

Table of Contents

List of Tables

List of Figures

List of Appendices

Nomenclature

ABB	Asea Brown Boveri (7 axis servo robot)
AlTAP	Aluminium Thermal Analysis Platform
ASTM	American Society for Testing and Materials
C_d	Coefficient of drag, dimensionless
d	Distance – linear dimension of the flow path (m)
$d_{critical}$	Length of runner ramp necessary for the melt flow to achieve (0.5 ms^{-1})
F(j)	Cumulative density function
Fr	Froude number: Ratio of inertial pressure disturbing the surface to the restraining pressure affected by gravity, dimensionless
F(x)	Weibull density function
g	Acceleration due to gravity (9.8ms^{-2})
h	Height (m)
$\Delta h_{critical}$	Free-fall height necessary to achieve a flow velocity of (0.5 ms^{-1})
Hg	Mercury column (mm)
IT	Initial Transient: The initial metal to flow into the mould, specifically into the runner
K	Weibull distribution shape parameter
n	Viscosity (centipoises)
r	Radius (m)
Re	Reynolds number, dimensionless
RPT	Reduced Pressure Test

SDAS	Secondary Dendrite Arm Spacing
SEM	Scanning Electron Microscopy
T	Surface tension (Nm^{-1})
UTS	Ultimate Tensile Strength: Maximum force (in tension) able to be achieved before sample fracture (MPa)
V	Velocity (ms^{-1})
V_{avg}	Average velocity (ms^{-1})
$V_{critical}$	Critical Velocity: velocity at which a flow of aluminum contains enough momentum to rise to the sessile height of 12.5 mm (0.5 ms^{-1})
V_{IT}	Initial Transient Velocity: velocity of the initial flow of metal into the mould, specifically into the runner (ms^{-1})
$V_{IT\,B}$	Initial Transient Velocity- Baseline: velocity of the initial flow of metal into the mould during Phase I - a production mould fill (ms^{-1})
$V_{IT\,P}$	Initial Transient Velocity- Production Benchmark: velocity of the initial flow of metal into the mould during a production mould fill (ms^{-1})
WAP	Windsor Aluminium Plant (Nemak of Canada)
We	Weber number: Ratio of inertial pressure disturbing the surface to the restraining pressure affected by surface tension, dimensionless
x	UTS value (MPa)
λ	Weibull Modulus, dimensionless
μ	Lower strength boundary (MPa)
ρ	Density ($Kgcm^{-3}$)
σ	Weibull modulus Position parameter, dimensionless

Chapter 1
Introduction

1.1 Head Deck Porosity

The casting of the highest quality aluminum cylinder blocks in the world is currently the sole function of the Nemak Windsor Aluminum Plant (WAP) (Windsor, Ontario, Canada). The casting plant, its management and employees have established themselves as the gem in the worldwide business of automotive cylinder block casting facilities. It is important to note that the author does not use the word "foundry", because this plant is far different than the traditional concept one maintains of a foundry where metal is melted and poured into a mould to produce a casting. What separates this facility from the "normal" concept of the foundry is the high degree to which the latest technology has been applied. At the time of this writing the casting plant is 15 years old, and the equipment, individually considered, can no longer be called the most up to date, but the application of advanced automation as a whole to the business of making castings is still unsurpassed in the industry, and this is proven by the fact that all 4 cylinder blocks cast at the WAP achieved "Best in Class" status in 2004.

Of all the technology that makes this plant a first class operation, the process by which the castings are made is the centrepiece. The Cosworth Precision Sand Process incorporates the best methodology in all casting processes to yield the highest quality sand castings found in the high volume automotive industry. The process as it is applied at WAP is not without its imperfections however, and the one with the greatest impact on the plant is a defect known as "Head Deck Porosity". This defect is of greatest concern because it is

responsible for the majority of the scrap parts (59.9%) detected at the customer's point of use. To put this scrap rate into perspective, it represents only 0.21% of the 600,000+ parts shipped to the customer in 2004, however the cost of the raw materials, labour and equipment use expended on the scrapped part results in a significant cost loss approaching one-half million dollars per year.

Head Deck Porosity is the condition where one or more pores or bubbles have come to be frozen near the head deck surface of the cylinder block, at such a depth as to be exposed during the final machining of the part. The reason this presents a scrap condition is that the surface no longer presents a contiguous mate for the cylinder head gasket to rest against. In effect, the pore will become a leak path for hot exhaust gas to pass through causing eventual failure of the gasket that will subsequently worsen engine performance and increase emissions output.

Since this problem represents significant lost revenue to the Windsor Aluminum Plant, reasonable efforts and expense to solve the problem are justified. With the aid of NSERC/Ford-Nemak/University of Windsor Industrial Research Chair in Light Metals Casting Technology (IRC) and the Auto 21 supported research program therein, the research at hand is an attempt to determine the root cause of head deck porosity via experimental methods using production moulds, and to propose a solution based on the application of the most current literature on the subject of aluminum casting technology. Chapter 4 will lead the reader through the experimental phases of this project and the results will be presented in Chapter 5. In Chapter 6 the data will be discussed, with conclusions drawn in Chapter 7. A solution to the problem and further recommendations will be presented in Chapter 8.

Chapter 2
Research Objectives

2.1 Experimental Discovery – Current Runner Design

Hypothesis: The current 3.0L cylinder block mould runner design is flawed in that it facilitates the entrainment of air into the lead metal, which subsequently comes to rest and solidifies at or under the rear / head deck area of the casting – a defect known as "Head Deck Porosity". A new design in accordance with the latest research will reduce or eliminate this casting defect.

The main objective of this body of work is to offer objective evidence that at least one cause of head deck porosity bubbles is the design of the runner system used in the 3.0L Duratec aluminum cylinder block casting currently in production at the Windsor Aluminum Plant. The project has two main thrusts of effort:

a) To develop a procedure wherein aluminum is poured into the current runner design at various velocities. The procedure will be employed to quantitatively determine if a correlation exists between the velocity of the molten aluminum streaming along the runner, and the resulting bubble/oxide entrainment damage to the liquid melt.

b) To design a running system based on current research that minimizes or even prevents the production of bubbles and thus presents a solution to the head deck porosity scrap issue.

2.2 Proposed Runner Design

This phase of the project was accomplished with the assistance of the Ford Motor Company Casting Division Simulation Team using casting simulation software to engineer a running

system fit for production that will yield the same quality cast component in all aspects except head deck porosity. As the engineering and purchasing of tooling to make castings for evaluation is beyond the scope of the current work, the proposed solution was designed and modelled in a simulation to explore metal velocities and mould fill characteristics.

The work of Professor Campbell will be drawn on heavily as his is most directly applicable to the subject at hand, as he is the inventor of the Cosworth Precision Sand Process. To date, no running system being filled by the Cosworth Precision Sand Process has been studied in the manner undertaken herein, but there are several works that, while applied generically to low pressure fill methods, nevertheless offer generic insight into the nature of aluminum behaviour while flowing down a long passage on its way to becoming the largest cast component in the automobile industry today – the cylinder block.

Chapter 3

The State of the Science- Literature Review

3.1 Prior Work – A Summary of In-House Problem Solving

Problem solving efforts have been and continue to be one of the keys to the success of any business, whether the problems are technical, relational, or financial, and within the business of making complicated, high-volume automotive casting there are no shortage of issues to be remedied, each requiring the ingenuity and creativity of people devoted to the honourable task of making castings. Several problems have presented themselves at the Windsor Aluminium Plant, and each has been addressed with results that some have been solved, others mitigated, and yet others remaining at large. Among the opportunities posed by process and part issues at the plant have been the completion of several master's and doctoral degrees each focused on a specific troubling, or unknown aspect of the process. Many research papers and reports have been published by the Industrial Research Chair (IRC) at the University of Windsor in cooperation with the plant engineering staff, each adding depth of understanding the complex casting process. Subject matter ranging from the study of the metallurgical properties of the castings such as solidification and fatigue life [1, 2] and insoluble titanium/aluminium/silicon crystals [3], to process capability studies entailing the design of artificial neural networks for the prediction of silicon modification levels [4], and production related issues such as the fading phenomenon seen in strontium modified melt [5] and electromagnetic pump clogging [6]. More specifically related to this thesis, various aspects of porosity have been studied since the plant started production, including the study of microporosity levels affected by copper, manganese and iron levels in

the melt, the study of hydrogen related porosity and subsequent development of a hydrogen content measurement system for the molten aluminium [7-9], and numerous reports aimed at characterizing porosity type defects found in daily production (i.e. bulkhead macro porosity [10]).

The Head Deck Porosity defect is a unique category of "casting porosity", and is one of the unsolved issues affecting the castings. The issue has seen a great deal of study by the plant engineering staff (the author and colleagues) and leads to the point where this thesis begins. The results of thesis will be the first published data set with regard to Head Deck Porosity.

The current research leaves off at an experiment in which tracers, placed in the runner before pouring, appear in the casting at precisely the same location as head deck porosity is seen in scrap blocks returned from the customer. The tracers were various types of debris – loose crushed aluminum oxide, Part I liquid resin drops placed down the runner, crushed potato chips, and liquid boron nitride drops placed down the runner five minutes prior to casting. In all cases (11 castings) the tracers and associated gas bubbles (in the case of the liquids dripped into the runner) came to reside in the extreme rear of the casting, with some making their way to the ceiling of the mould – the head deck surface of the casting. The control sample (regular production condition) in this group did not have the same symptom. The conclusion reached from this work was that the first metal to flow down the runner system is the metal that contains the bubbles that are eventually found at the rear head deck area of the casting. Where the bubbles were being formed in their journey down the runner and into the rear of the casting is the subject of this thesis, however it must be brought to the reader's attention that accompanying this "first metal down the runner" discovery is another important piece of the puzzle. It was discovered by the author using moulds that had probes

installed at 80 locations, and confirmed by Ford Casting Division's CAE simulation group, that the molten aluminum was being pumped into the mould so fast that there was a plume created at the top of the rear risers (in-gates). This, according to all the literature was a condition favourable to the creation of bubbles, thus steps were taken to reduce the mass flow-rate of the molten aluminum at the point where the risers were nearly full. This action reduced head deck porosity scrap by roughly 50%.

Now that the reader has some background understanding, the application of current research must be brought to bear on the subject. Although there is a great deal of literature published about filling/running systems, very little applies to the type of process used to produce the subject castings. Professor John Campbell's recent work "10 Rules of Castings" [15] details the casting process and design do's and don'ts for making castings, and when applied to the subject at hand, lead to the exploration of the runner system as one possible source of air entrainment resulting in head deck porosity. When combined with the prior WAP work the logical connection between runner design and head deck porosity materialized.

For the reader to gain a broad enough understanding of the elements contributing to the problem at hand, some discussion on the basics of the aluminum behaviour and its interaction with the mould environment are discussed prior to any current runner-based research discussions.

3.2 The Cosworth Casting Process (Precision Sand Casting Process)

The making of castings has been referred to both as an art and a science. In the opinion of this author, the installation of the Cosworth Process at the Windsor Aluminum Plant brings the business of making castings as close to a science as exists in the industry

today. This is because, unlike any other process be it high pressure die casting, gravity casting or low pressure process, the WAP Cosworth Process employs methods that when added together, result in a very robust system for making quality castings. Generically these process characteristics may be defined as; handling of the melt in such a way as to provide clean metal to the mould, sand type, quiescent mould design, casting orientation, mould feeding system, mould inversion and full automation of the process including filling of the mould.

3.2.1 Handling of the Melt

Since aluminum alloys have the propensity to oxidize so readily to form many different oxides, care must be taken to avoid conditions leading to their creation. Since it is next to impossible to completely eliminate oxide formation in a melting operation there will always be oxides present in a bath of molten aluminum. The first unique feature of the Cosworth Process is known as "residence time". The rule of thumb is: any metal entering the pouring furnace must reside in that furnace for a minimum of 10 hours before being moved into the mould. In this way, the oxides of the melt that are more dense than the bulk density, such as oxides of Fe/Mn/Mg (sludge), will sink to the bottom and the lighter oxides such as aluminum oxide, magnesium & titanium oxide etc. will float to the surface leaving the "centre" of the bath relatively clean. It is from this "clean" zone that aluminum is drawn for injection into the mould. It has been shown however that this method of cleaning is not a catch-all, as it was found that strontium-chloride and other salts have survived the residence time and come to reside on the surface of the ceramic wall within the electromagnetic pump [11].

3.2.2 Sand Type

Another important distinguishing feature of this process is the type of sand used in making the moulds. Zircon sand has a coefficient of thermal expansion less than that of silica sand, which means that a core made of zircon sand will change shape less than one made of silica sand once surrounded by molten aluminum. This enables the casting of oil galleries and other small and delicate shapes into the part with high confidence that the core will not distort and wander during solidification causing thin walls within the casting. Additionally, since the coefficient of thermal conductivity of zircon sand is greater than that of silica sand, the zircon sand mould is able to absorb heat from the liquid casting faster than a mould made of silica. Thus the microstructure achieved in a part cast in zircon sand has a finer grain structure than the identical part cast in silica sand due to a faster cooling rate which yields higher mechanical properties. In addition to this benefit, individual sand grains are much less likely to crack and fragment upon contact with the hot molten aluminum (which would render them too fine to reuse), allowing repeated re-use of zircon sand. It must be mentioned here that cost is a severe penalty one must pay to purchase a specific quantity of zircon over silica, however because of the recyclability of Zircon, the cost is awash in the end.

3.2.3 Mould Basics

The interlocking sand mould is completely recyclable within the process. The mould consists of a series of eighteen phenolic urethane resin bonded zircon sand cores which when fitted together form a self contained recyclable mould, with the exception of the resin binder.

The whole assembly starts with a "base" core, onto which a "journal" core is placed to provide riser shape, followed by the crankcase, front, rear, sides, left and right cylinder bore/head deck banks, and seven more internal cores that form breathing, cooling and oil flow passages for lubrication. A clamp within the casting machine acts to hold the assembly together, ensuring the cores will not move during the casting process. All venting accommodations, casting shrink allowances and sand traps (spaces for rubbed sand to fall during assembly of cores) are all designed into the shape of the cores to allow a robust assembly process that yields a high success rate despite some acceptable mould-to-mould variance in the assembly process. The base core is the subject of this research, in that it provides the runner cavity shape which directs the aluminum to the gates, risers and eventually to the casting itself, and thus will be the focus of this research. Since the filling system (i.e. runner, gates and risers) and the metal flow therein is paramount to the discussion; the following section is dedicated to its description.

3.2.4 Filling System

The filling system is that part of the mould cavity responsible for directing the molten metal to the casting cavity – where the product is generated. In this study, the filling system consists of the runner – a channel that carries the aluminum the total length of the mould package, followed by the in-gates, which allow liquid to flow from the runner into each of the eight in-gates/risers, which then pass the aluminum on to the casting cavity. The speed or rate of metal movement is important, as is the degree of cooling while the metal is flowing. The shape of the different system components can be used to regulate the flow, which is an important parameter in the making of a casting, but the systematic analysis and discussion of

the initial stage of the pouring process have been rare [12, 13]. The "initial transient", is the event of the first metal meeting air within the runner. After the initial transient has occurred, the runner fills and achieves a steady state where it is passively guiding metal to the next cavity within the mould (risers). Isawa and Campbell [12] have performed work on reducing the impact of the runner on the quality degradation due to the initial transient, where they concluded that the rate of bubble removal, and the estimated time of complete disappearance of bubbles could be used to measure the optimization of the shape of the running system. These metrics proved useful in their work, which involved pouring the metal down a sprue, which in turn fed the rest of the system. The current work is aimed at the same goal, however the metrics will be the quantity of bubbles captured in a quickly chilled runner sample.

The first of six requirements of a good runner design, according to the American Foundry Society publication Aluminum Casting Technology [14], reads as follows:

> "...flow through the gating system with the least amount of turbulence to prevent the aluminum oxide film from breaking and, thereby, allowing the entrapment of air; mould and core gasses; and inclusions such as dross, sand and other foreign materials".

This is the same requirement put forth by Professor John Campbell as his 2nd rule of making good quality castings [15] as will be discussed in more detail in later sections of this review. It is important to note that just under half of this book by Professor Campbell is devoted to the subject of avoiding bubble entrainment in the gating system. It is also important to note that these two casting industry authorities recognize the gating system as a major source of air entrainment into the melt.

Another major consideration in examining the design of the running system is thermodynamics. Slow filling and high loss of heat result in misruns and cold-shuts within the casting. Rapid rates of filling can produce erosion of the gating system or even the mould cavity itself resulting in entrapped mould material (sand) within the casting. Simulations have been performed in various applications, (Sulaiman et al. modeled the runner system for the die casting process to determine the angle at which the gates are best attached to the runner with success), however the low pressure Cosworth process produces flow of an entirely different nature [13] and the running/gating systems have not been adequately studied.

3.2.5 Mould Feeding System/Casting Orientation

The next important strategy is the orientation of the runner, risers and casting with respect to each other, and to the world (i.e. gravity). In order of sequence, the molten aluminum entering the mould fills the runner system, which is the lowest point in the entire mould cavity. The runner then delivers the melt to the risers, then to the thicker sections of the casting, and finally to the thinner sections of the casting nearest the top of the mould. As the first metal into the mould is pushed further up into the cavity, it loses heat to the surrounding sand mould walls. While losing heat the metal is simultaneously being pushed further up into the mould cavity where the wall thickness is becoming smaller. In this way, once the mould is full, the coldest metal is at the top (thinnest walls) and as one examines the temperature of the metal further and further down into the casting and finally the risers, the temperature of the metal, being the last metal in, is higher. It is at this point that the mould is

inverted or turned upside down i.e. "rolled-over" which is the next point of importance in this process.

3.2.6 Mould Inversion (roll-over)

Once inverted the coldest metal is now at the bottom of the mould where the thickness of the cast sections are at a minimum, and the hottest metal is at the top of the mould (thickest sections). Directional solidification from cold (thin sections) to hot (thick sections) result in the last metal to solidify in the riser/feeder cavity as must be the case in all-successful casting schemes. The inversion of the mould enhances the directional solidification by taking advantage of gravity and the temperature/density related physics presiding over the cooling melt as the hot liquid rises continually to where the casting most needs hot metal to feed the shrinking cooler sections. Additionally, the propensity for damaging convection loops to form within the solidifying casting is eliminated by the inversion of the mould as is discussed in Professor Campbell's 7th rule for making castings [15].

3.2.7 Electromagnetic Pump Mould Filling -Getting the Melt into the Mould

Electrohydrodynamics embodies the physics behind the movement of the liquid aluminum into the mould, and will not be discussed herein, but the fact that the aluminum does move into the mould with a controlled velocity is critical to this discussion. From a casting process point of view, the freedom this equipment provides from the reliance on gravity to fill the mould is the feature of interest. The electromagnetic pump provides control

over the flow-rate of aluminum entering the mould according to the design of the casting engineer. As the pump is activated (i.e. voltage is applied), molten aluminum enters the mould via the runner. The "program" or desired flow rate as a function of either time or metal level within the mould is followed until the mould is full. A capacitive sensor outside the mould provides feedback to the controller regarding the height of aluminum within the package. This actual level is then compared to the programmed or desired level, and the proportional – integral – derivative (PID) control system then raises or lowers the voltage to the pump to bring the actual metal level closer to the desired – is a classical case of closed loop feedback control. Once the mould is full, the liquid metal is then held under mild pressure from the pump during the roll-over process [16]. Although the pump provides an improved method (compared to gravity) of moving molten aluminum into the mould, it cannot compensate for a) poor casting practices (i.e. mould design), b) inertial effects of the molten flow or c) the casting engineer's programming skills. The basic rules in making castings must be followed to take advantage of the unique capabilities that the electromagnetic pump offers.

This research takes aim directly at the first metal to enter the mould, or the "initial transient" as it is referred to by Isawa and Campbell [12]. It is this metal that, when subjected to a poorly designed runner system, reaches uncontrolled velocities imparted by gravity. The speed of this metal is beyond the control of the electromagnetic pump, leaving it to be entrained with folded oxides and air bubbles, later to be carried to the rear head deck area of the casting. Before presenting any further conjecture however, the most recent casting and runner technology will be explored in order to set the stage for the logical progression from conjecture to fact. Figure 3.1 depicts the current runner system used to make cylinder block

castings, and though this design has been used to make nearly five million castings with only 0.21% (~11,000) scrapped due to head deck porosity, there is room for significant improvement.

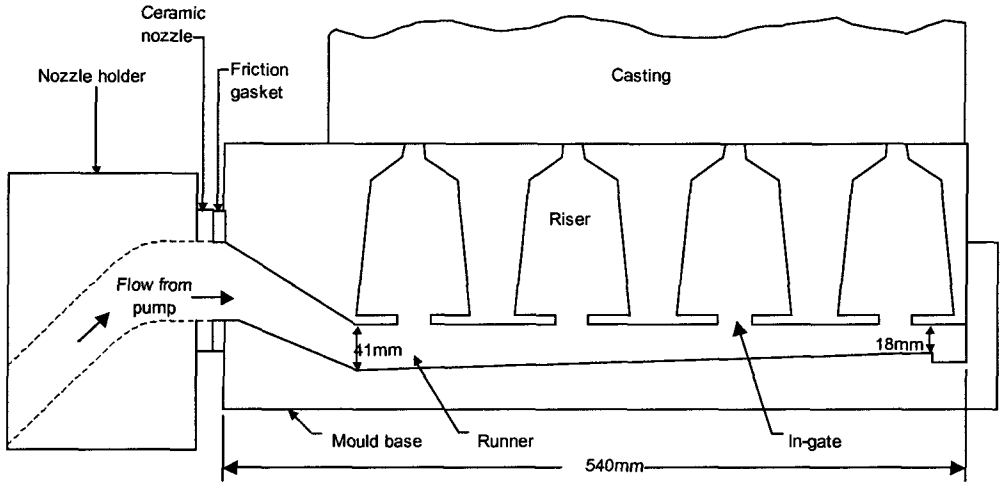

Figure 3.1: Cross section of the current mould (sectioned through runner, in-gates and risers).

3.2.8 Current Runner & Gating Methods

There is only one way to get liquid metal to flow into a mould, and that is to induce flow by applying a force – either pushing or pulling the metal into the cavity, or both. The source of this force varies according to the casting "process" one is using. The "Gravity Pour" system allows gravity to cause the liquid metal to seek an equilibrium elevation between the metal within the mould cavity with that in the sprue (Figure 3.2a). The "Low-Pressure" system utilizes some sort of "push" to force the liquid metal into the mould against the ever-present force of gravity (Figure 3.2b). Aluminium castings are made using both Gravity and Low-Pressure Processes, each rendering a different effect on the cost and quality of the part. The nature of the part being cast is also a large factor in determining which process is best suited

for use. In either process, the velocity and associated turbulence of the flow must be controlled so that excess oxide formation and air entrainment is avoided.

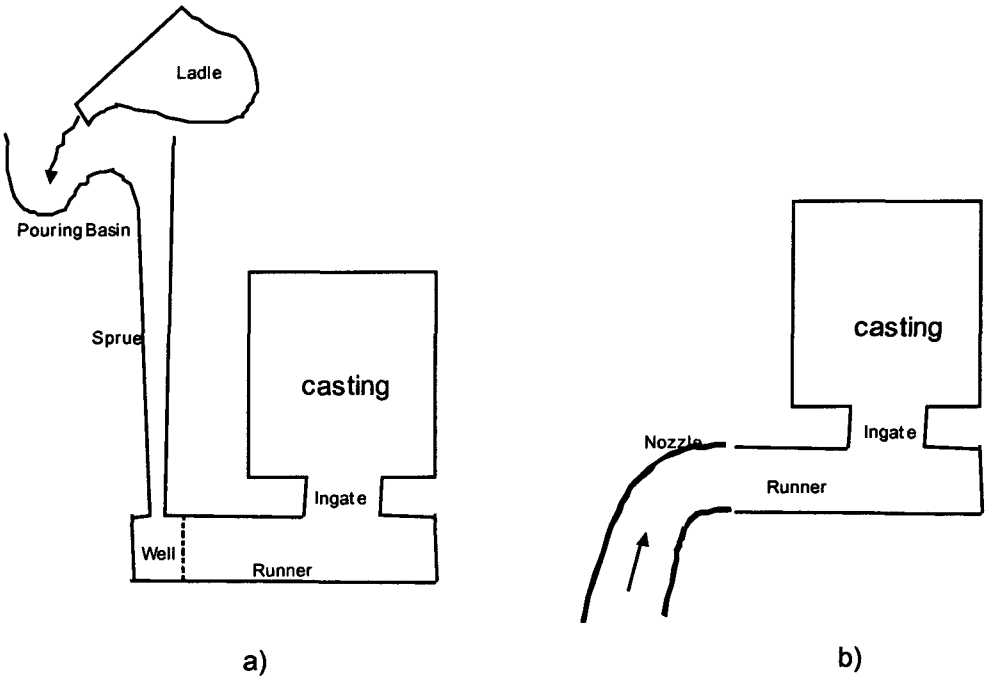

Figure 3.2: Cross section of a simple mould filled by a) gravity, b) low pressure.

Regardless of the method of introducing liquid metal into the mould, the gating system is responsible to direct the liquid into the casting cavity. There are two types of gating systems: pressurized and non-pressurized. The difference between these two types of gating systems lies in where the choke is placed. The choke is the smallest cross sectional area of the system and sets the rate of flow of the molten metal into the casting cavity [17] (at least in a Gravity Pour system). The choke in the pressurized gating system is normally the in-gates (the passages leading directly to the casting or the risers prior to the casting) hence the runner system is "pressurized" due to the downstream flow restriction. The characteristic advantage of the pressurized system is improved yield (since the runner will hold less metal in total), however a disadvantage is that the liquid metal is subjected to higher velocities than in a non-

pressurized system, which results in more turbulence and hence oxide formation and air entrainment. The choke in a non-pressurized system is upstream of the in-gates, usually at the beginning of the runner, and is designed as such to facilitate quick filling of the sprue, and slow, quiescent filling of the runner. The runner itself can be set in the drag or in the cope with the ingates being set in the opposite part of the mould depending again upon the application and economics of the situation. There are a large number of metal flow-path design options available to the casting engineer to allow her or him to achieve the highest quality part at the lowest cost, and the common thread linking all of them is velocity and turbulence of the liquid. This parameter is of extreme importance. The runner has been and continues to be an item depended on to solve several types of casting defects such as gas porosity, shrink porosity, bubbles, oxide discontinuities, cold-shuts and laminations. The runner can contain filters to reduce flow velocity and act like a choke while straining out large oxides, it can be extended past the last ingate to allow the "first pour" or "initial transient" to pass all the ingates and carry its bubbles and oxide films into a dead end, there to solidify harmlessly. The runner can be shaped to reduce turbulence; it can be sloped, tapered or necked down after each ingate to maintain equal pressure at the entrance of each ingate to ensure equal flow-rate into each ingate. In short, the runner design is critical in the delivery of unharmed liquid metal to the casting cavity. In the Low Pressure Process the runner is usually a pressurized system, which partially allows the low-pressure source to control the rate of runner fill. Provided the controls are sufficiently robust and the design of the runner is sound, the runner of each mould will be filled identically and quiescently resulting in few entrained oxides or bubbles. The runner design being studied in this thesis is a pressurized runner system filled by a Low Pressure Process, and is also one that is

associated with castings that suffer from bubbles near the head deck surface. With this in mind the direction of study will turn to examine the characteristics of flow within the runner, its velocity, turbulence and propensity to form oxides.

3.3 The State of the Industry in Casting Technology

3.3.1 The 10 Rules of Castings

Professor John Campbell (University of Birmingham U.K. 2004) has published work [15] that outlines 10 rules to be followed by the casting engineer, each of which plays a critical role in the creation of a sound casting.

1. Achieve a good quality melt
2. Avoid turbulent entrainment (the critical velocity requirement)
3. Avoid laminar entrainment of the surface film (the non-stopping non-reversing condition)
4. Avoid bubble damage
5. Avoid core blows
6. Avoid shrinkage damage
7. Avoid convection damage
8. Reduce segregation damage
9. Reduce residual stress (the 'no water quench' requirement)
10. Provide location points

The two rules that most apply to the current research are Rule 2 (Avoid turbulent entrainment) and Rule 4 (Avoid bubble damage). Each is elaborated upon in the following two sections.

3.3.2 Rule 2: Avoid Turbulent Entrainment (the critical velocity requirement)

"The avoidance of surface turbulence is probably the most complex and difficult rule to fulfill when dealing with gravity pouring systems" [15]. Since at least "80% of all casting defects are directly caused by turbulence" [15]. This statement is derived from the fact that molten aluminum, upon flowing along at speeds of greater than 0.5 ms^{-1} or falling from a distance greater than the sessile height (~12.5 mm) [15] may have the surface oxide film disrupted and included into the bulk liquid. "The surface film is not harmful while it continues to be a surface film. In fact, in the case of the oxide on liquid aluminum in air, it is doing a valuable service in protecting the melt from catastrophic oxidation" [16]. Equipped with this information, the casting engineer must strive to see the mould filled without achieving a flow front velocity of greater than 0.5 ms^{-1} to avoid casting defects such as entrained bubbles and oxide films. This concept is the most critical to the study at hand and will be discussed at length in future sections of this thesis. Rule 4 also deserves to be treated as another major player in the formation of bubbles, bubbles that end up within the casting, especially at the head deck of the cylinder block casting.

3.3.3 Rule 4: Avoid Bubble Damage

"Entrainment defects are caused by the folding action of the (oxidized) liquid surface" [15, 16]. As the oxide surface film is disrupted (broken) by surface turbulence, a piece may be folded over onto itself, dry side to dry side [18-20], encapsulating the atmosphere (air) between two oxide layers as depicted in Figure 3.3. Since the non-wetted or dry surface of each of the oxides is rough, the sandwiching of these two surfaces entraps air on both a

macro and a micro scale, depending on the roughness of the surface and the magnitude of the fold event.

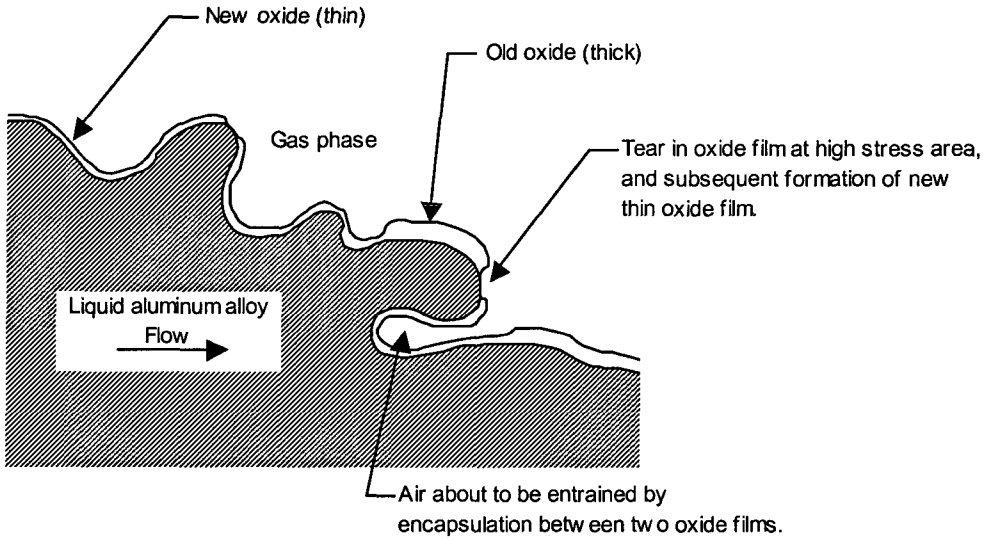

Figure 3.3: Schematic of a splash of molten aluminum showing the formation of a folded (double) oxide film, which might consist of old thick film, new thin film, or both, all likely to occlude air in the folds. After Campbell 1991.

Since the liquid flow is encapsulated beneath the film of oxide, it may become turbulent without having any additional liquid aluminum or its alloying agents exposed to the air above the film. This protection will last only up to the point where the strength of the surface oxide film can withstand the forces put on it not only by the turbulent liquid beneath beating, pushing and otherwise causing the film to bulge and distort, but also by movement of the flow along the mould passage.

The Reynolds number (*Re*) can quantify the turbulence beneath the oxide film covered surface:

$$\boldsymbol{Re} = V\varrho d/n \qquad (1)$$

where V is the velocity of the liquid, ϱ is the density of the liquid, d is a characteristic linear

dimension of the geometry of the flow path, and n is the viscosity. The ***Re*** number is the result of a comparison between inertial pressures $V^2\varrho/2C_d^2$ (where C_d is the drag coefficient) and viscous pressures nV/d. The inertial pressures related to the mass and velocity of the liquid flow "own" a momentum that will exert certain distorting forces on the constraining surfaces of the flow (oxide surface, mould wall), while the viscous pressures are the result of drag from the walls of the passages and film surface containing the flow. For values of *Re* below 2000, viscous forces prevail, while above this the flow "degenerates into a chaos of unpredictable swirling patterns" [16] all of which take place beneath the covering oxide film. The flow near the boundary will still be laminar in nature, but decreasingly so as the R*e* increases beyond 2000, hence the oxide layer forming the boundary is protected from the bulk of the turbulence. Above 20,000 the flow is completely turbulent [16]. This "bulk" turbulence then only applies to the liquid beneath the film, and has little bearing on the surface oxide layer. The concept of surface turbulence is the real mechanism by which the surface film finds itself submerged and incorporated into the bulk of the melt [16]. This effect is better represented by the Weber number than the Reynolds number, which describes bulk turbulence beneath the surface. Surface turbulence is generated by poor handling of the melt at any of the venues in which it is moved or disturbed (i.e. moving molten aluminum from the holding furnace to the ladle, from ladle to casting furnace, or in the case of the Cosworth Process, from pump to mould, and so on). Of key interest, in fact the reason for this work, is the study of the movement of the melt down the runner system of the mould. Here the aluminum first enters the mould and immediately flows down a 19° grade ramp which induces such high speed that the surface becomes turbulent, tossing, folding and braking up the oxide film with such energy that creation and subsequent entrainment of air

generates bubbles. As Nyahumwa states, "this failure to control the filling process results in the advancing liquid front becoming unstable and entraining folded oxide-to-oxide film into the liquid" [21]. These bubbles are then carried along in the flow, finally to come to rest (in solidification) within the casting. In Figure 3.4, it can be seen that the head deck porosity bubbles mostly come to freeze in the rear of the casting, near the head deck surface.

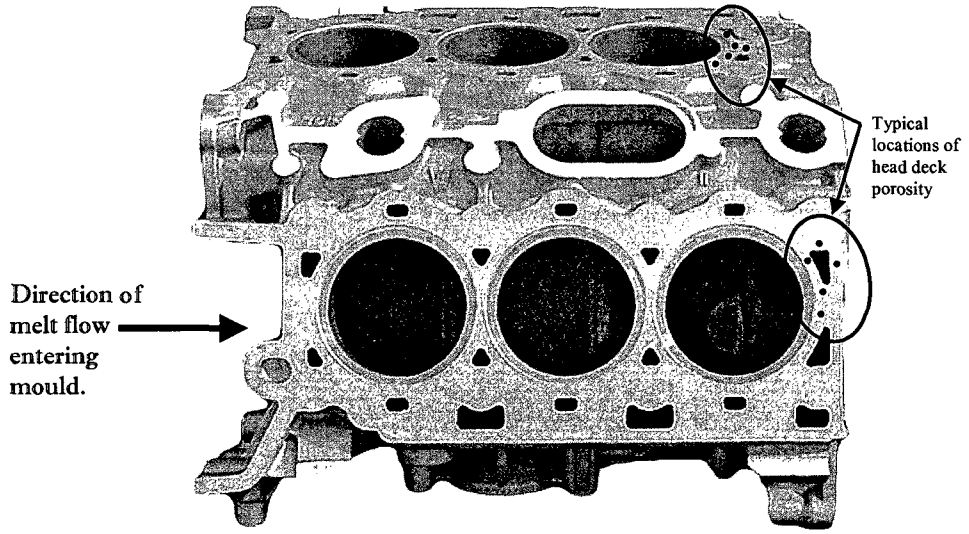

Figure 3.4: Concentration Diagram of the Ford 3.0L Duratec cylinder block for location of head deck porosity.

As stated at the outset of this chapter, the earlier work conducted by the author and one of his colleagues Dr. G. Byczynski, has shown that the first metal to run down the runner in fact comes to be the metal residing in the rear of the casting which includes the head deck surface. Rule 2 is being broken in the making of the castings that contain head deck porosity, and it is the intent of this thesis to examine the role of the runner in this rule-breaking activity.

The entrainment of folded oxide films into the bulk of the liquid metal occurs for a number of reasons: 1) meniscus damage as a result of surface turbulence during filling. 2) bubble

damage due to priming of a running system where air bubbles and attached oxides are entrained into the liquid metal and 3) temporary arrest of an advancing liquid metal meniscus during horizontal and downward flow of liquid metal when it is submerged by the melt [16]. There are as yet no universal design rules for gravity filling systems that are able to guarantee defect-free aluminum alloy castings, even though it is known that different running systems have different propensities to entrain folded oxide films in the castings. Mould filling systems are known to be the primary source of oxide film defects into aluminum alloy castings[16].

Further discussion is required of the surface oxide and its role in the process of making quality castings.

3.3.4 Surface Oxides

The oxide of pure aluminum is known as aluminum oxide Al_2O_3. This oxide is formed as atoms of aluminum are exposed to oxygen. Freshly exposed aluminum liquid will immediately grow an aluminum oxide covering, film or skin. In the case of an alloy of aluminum containing Magnesium as a predominant example, the oxide will be a combination of MgO and Al_2O_3, or spinel ($MgO.Al_2O_3$). The film growth takes place "atom by atom, as each metal atom combines with newly arriving atoms or molecules of the surrounding gas", the gas in our case being air [16]. In the case of pure aluminum, the initial stage of film growth is thought to start with the rapid formation of an amorphous alumina layer. This amorphous [22-24] structure then becomes crystalline in structure known as gamma (γ) alumina, a cubic spinel [25] which is has little or no plasticity, and inhibits further oxidation of the liquid below. The film then changes in nature to become alpha (α) alumina or

corundum which is a rhombohedralin structure [25, 26]. The volume of the oxide decreases by 24% but oxidation is able to occur at a faster rate through this covering because the shrinkage effect has broken the brittle surface exposing the liquid below [20, 25]. It has been suggested that oxide films fall under two broad categories; new and old [16]. New films are formed during pouring of the molten aluminum and their formation can be observed on the liquid stream as the melt is poured. New oxide films can also form in the runner system and mould cavity due to surface turbulence and the interaction with air. New oxide films are characteristically thin and folded when seen on a fracture surface [21]. Old films form on the surface of molten aluminum held in a furnace or ladle. These films are thick, often extensive in area and able to retain their size and shape due to their strength. Table 3.1 shows one concept of oxide categorization by age.

Table 3.1: Forms of oxide in liquid aluminum alloys. After Divandari & Campbell [20].

Growth Time	Thickness	Oxide Type	Description	Possible Source
0.01-1s	1 μm	New	Confetti-like fragments	Pour and mould fill
10s to 1 min	10 μm	Old1	Flexible, extensive films	Transfer ladles
10 min - 1 hr	100 μm	Old 2	Thicker films, less flexible	Melting furnace
10 hr - 10 days	1000 μm	Old 3	Rigid lumps and plate	Holding furnace

For the intent and purpose of this research it can be assumed that for the case of aluminum flowing down a runner, newly exposed aluminum surfaces form skins instantly [25]. The tensile strength of this film, or skin, as depicted in Figure 3.5, is quite extraordinary, as a film less than 30 seconds old will withstand a steel probe pushed to a depth of roughly 6mm while remaining intact (319 alloy at 760° C, air atmosphere). When pushed beyond this depth the oxide film tears and surprisingly the depression does not fill with liquid. The oxide film seems to reform so quickly that it is able to hold the surface liquid at bay even while the probe is pushed further into the bath – the depression is maintained up to 6 mm below the

rest of the bath. This highlights how quickly the oxide forms on the surface, faster than the time it takes for the head pressure to push the liquid back into the depression. Thusly stressed, the young 0.1 μm thick oxide layer maintains integrity until breaking stress at approximately 148 MN/m^2 (MPa) [25].

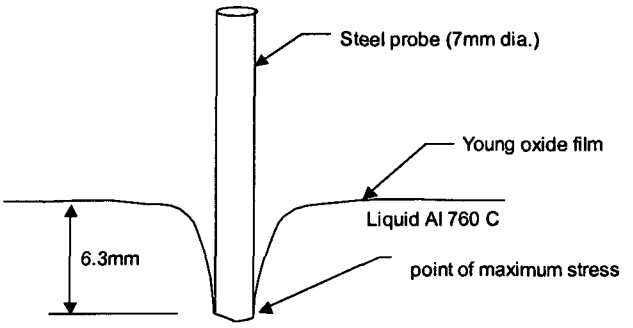

Figure 3.5: Probe being pressed into the film of aluminum oxide on the surface of molten aluminum – demonstrating the capability of the film to withstand tensile loading.

Because the film has such strength, it can "contain" a column of liquid aluminum poured onto a flat horizontal surface. As described in Section 3.3.3, if the action of the liquid, in a flow for example, is turbulent enough to overcome the film strength, the film will tear. If, on the other hand, the liquid is not in the dynamic or flowing state, but is still or quiescent as the case would be while sitting on a flat steel plate, the only danger to the film becomes the head height of the aluminum applying its weight to push against its captor (the film), while the film itself acts to try to keep the aluminum together in a puddle. An analogy can be drawn from the beads of water forming during a rainstorm on the nicely waxed roof of the family car. Depending on the strength of the surface film (i.e. the surface tension of the outermost molecules of water of the droplet), the vertical size (depth) of the drop is supported to a certain value before the film tears, the system breaks down and the bead spreads out to lower the depth of the liquid droplet – in effect lowering the head height. As more liquid is added,

the height again increases until the maximum is again reached, and so on. So it is with an aluminum alloy, in this case 319, the maximum depth of the "droplet" being approximately 12.5 mm [16]. Figure 3.6 shows a typical pour of a small (0.1 kg) amount of aluminum onto a steel surface. The same pour was repeated onto different surfaces, ceramic & concrete, and in each case the depth of the droplet remained approximately the same 12.5 mm as can be seen in Figure 3.7. This same approach was used by A. Halvaee and J. Campbell to determine the critical velocity of Aluminum Bronze Cu-10Al alloy, and a very close correlation was found for the theoretical value of $V_{critical}$ derived from the measured sessile height [27].

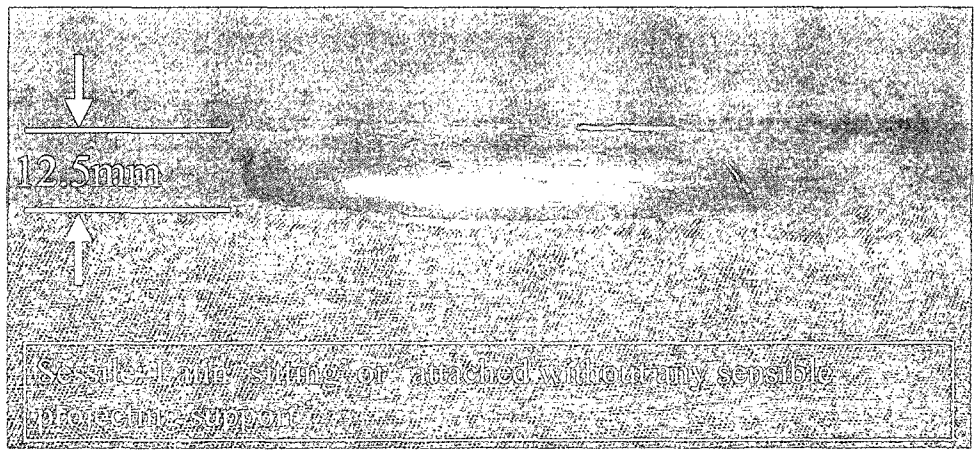

Figure 3.6: A typical self-supported column of 319 aluminum: the sessile height of 12.5 mm would have been maintained even if the poured volume of liquid in making the sample above was doubled or quadrupled. (Part of the author's experiments)

3.3.5 Critical Velocity Requirement

Rules 2 and 4 can both be satisfied if the velocity of the advancing liquid wave front can be kept below the value of 0.5 ms^{-1} ($V_{critical}$). The value for $V_{critical}$ can be derived as follows;

Suppose that a disturbance within a volume of liquid aluminum caused a force to be applied up against the oxide film surface. The surface will deform subject to the inertial pressure of

the disturbance, to form the beginnings of a wave. The value of the inertial pressure is

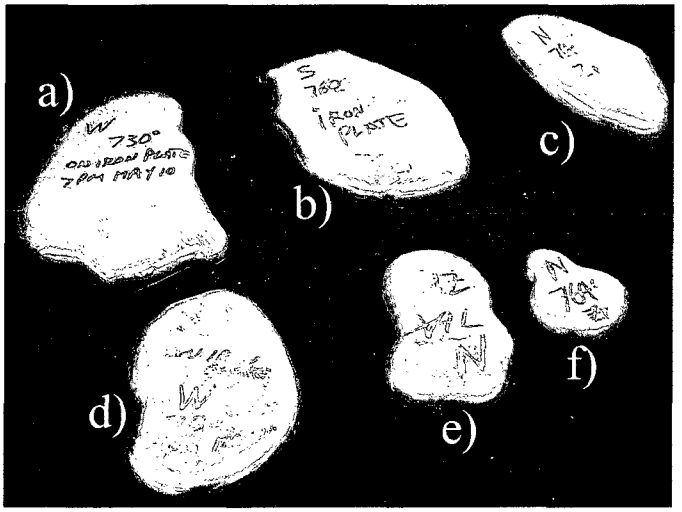

Figure 3.7: Sessile drops formed from different volumes poured onto different substrates at different temperatures; a) 730°C on Iron plate, b) 760°C on iron plate, c) 764°C on zircon sand, d) 730°C on iron plate, e) and f) at 764°C on zircon sand core. All samples measured between 12 and 12.5 mm in height.

approximately ρ (density of the liquid) x V^2 (velocity of the disturbance). Under ideal conditions, the wave will take the shape of a droplet of radius r, but its formation is restrained by the surface tension T in Figure 3.8.

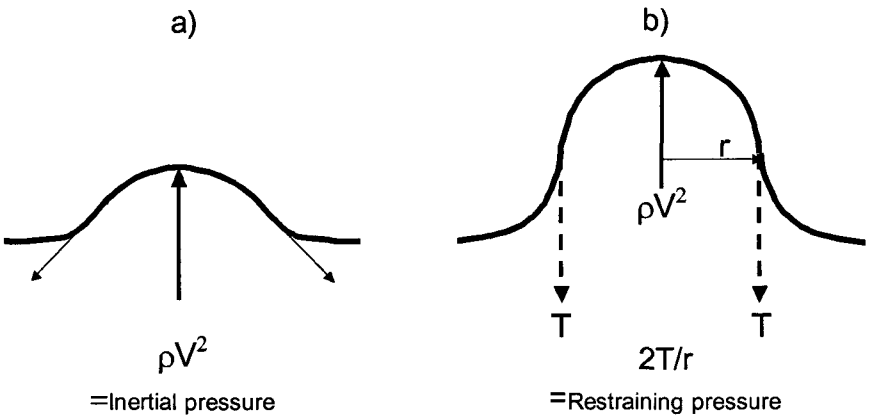

Figure 3.8: Inertial pressure vs. restraining pressure at the surface of the molten film forming metal (advancement of time- a to b).

The ratio of the inertial pressure to disturb the surface to the restraining pressure affected by

the surface tension is known as the Weber number We. If we assume We=1, then balance exists, or $\rho V^2 = (2\ T)/r$, which yields

$$V_{critical} = (2T/r\rho)^{1/2} \quad (2)$$

For aluminum, the value of T is approximately 1 Nm^{-1}; ρ is 2500 kgm^{-3}, and r is between 2.5 to 5 mm in diameter. Substituting, the result is $V_{critical}$ = 0.4 to 0.6 ms^{-1} [28]. Once this velocity is exceeded, the surface of the metal will behave in a turbulent manner leading to the break-up, folding and entrainment of folded oxide and potentially bubbles.

Another parameter that is useful to assess the possible break-up of the surface is the Froude number Fr [28]. The Froude number is the ratio of the inertial pressure to disturb the surface, to the restraining pressure effected by gravity. Since $Fr=\rho V^2/\rho gh$, and at balance Fr=1, then $\rho V^2=\rho gh$, or

$$V^2 = gh \quad (3)$$

Using equation (3) we find that for a wave h=12.5 mm high (sessile height), $V_{critical}$ = 0.35 ms^{-1}. The predictions made by these two calculations (Fr and We numbers) are nearly the same, both predicting a critical velocity somewhere between 0.35 and 0.6 ms^{-1}.

If the concept of surface oxide breakup and entrainment occurring at and above some critical velocity is true, then plans must be made to prevent such a condition during the filling of a casting.

To gain an appreciation of the conditions under which this velocity can be obtained, consider a stream of metal, free falling in a mould cavity. By the time the stream has fallen height Δh, the potential energy $E_g = mg\Delta h$ has become kinetic energy $E_k = \frac{1}{2}\ mV^2$ [29]. Solving for V we obtain

$$V = (2\ g\ \Delta h)^{1/2} \quad (4)$$

Where g is the acceleration due to gravity. Substituting $V_{critical}$ from (2) into (3) yields the critical drop height, or the height fallen at which V becomes critical (0.5 ms^{-1})

$$\Delta h_{critical} = V_{critical}^2/2g = 12.7 \text{ mm} \quad (5)$$

The liquid metal only needs to free fall 12.7 mm before it has reached the velocity that will lead to surface turbulence enough to damage the oxide layer. Note that this value is nearly the same as the sessile height referred to in the last section found by pouring molten aluminum onto a flat surface and allowing only the surface tension of the oxide skin to determine the depth of the droplet.

In dealing with an inclined surface, say the entrance of a runner, whose slope is 19°, where the molten aluminum is allowed to accelerate under the influence of gravity, the Δh becomes

$$\Delta h_{critical} = V_{critical}^2/[2g \sin(19)] = 39.2 \text{ mm} \quad (6)$$

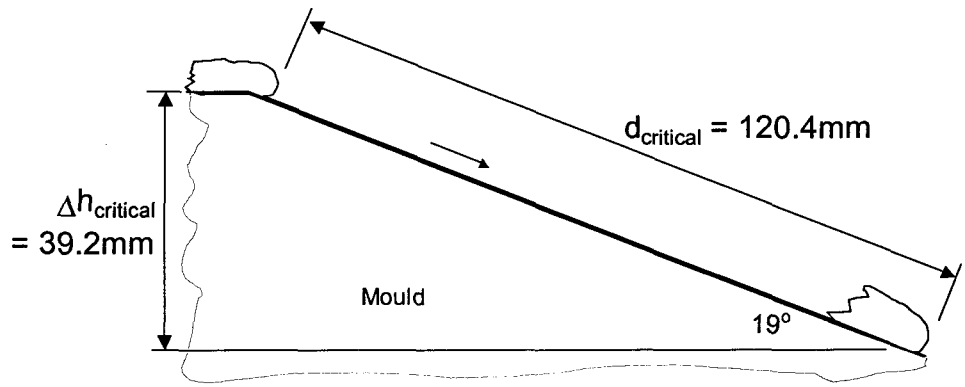

Figure 3.9: $\Delta h_{critical}$ & $d_{critical}$ for a flow down a ramp

As shown in Figure 3.9 above, the aluminum flowing down the slope will reach $V_{critical}$ in only 120.4 mm of travel assuming that the initial velocity of the liquid at the top of the ramp was zero. The runner under study in this thesis is represented in Figure 3.10. It is similar to the runner depicted in Figure 8 except d = 142 mm and Δh =50.2 mm. With these dimensions, the velocity of the flow upon reaching the bottom of the ramp is 0.56 ms^{-1},

which is already above $V_{critical}$ without accounting for any initial velocity at the top of the ramp! Add to this figure an initial mould entry velocity of .20 ms^{-1} (an estimate drawn from experience) and one ends up with a velocity at the bottom of approximately 0.76 ms^{-1}.

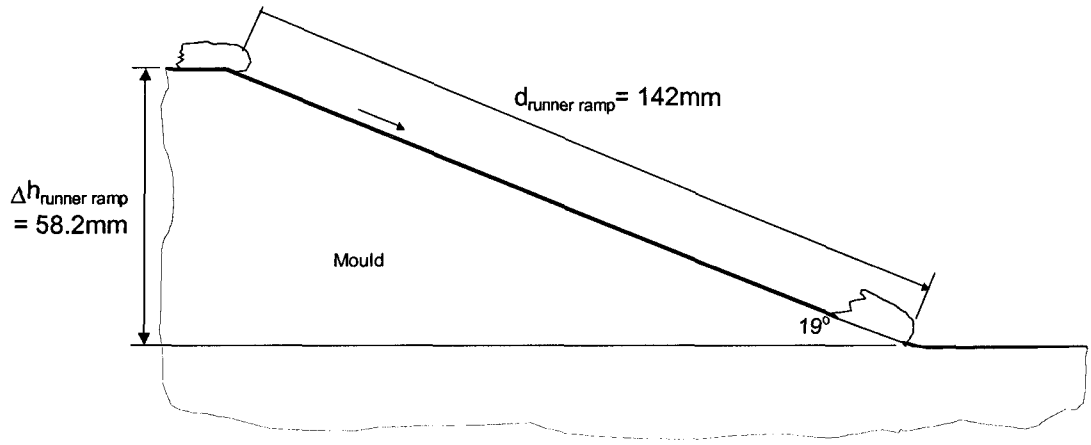

Figure 3.10: Sketch of the runner ramp under study. Dimensions result in velocities in excess of $V_{critical}$.

This simple design flaw can account for not only film defects in the cast part, but more severe defects such as bubbles, or bubbles accompanied by long bubble trails – essentially cracks – in the casting [16].

While in the dynamic state, as in filling a mould, liquid aluminum flows through an infinite variety of shapes, twists and turns in filling the cavity. As depicted in Figure 3.11, during the filling of a riser, as an example, there is a certain velocity of the advancing front above which the liquid column is provided enough energy to exceed the sessile height and result in the liquid falling back down to the height which can be supported by the film strength – the sessile height. Upon falling, the film enveloping the whole plume of liquid will be chaotically broken, folded and submerged as it settles back down into the liquid below creating not only double oxides, but enclosing air to form bubbles. At the critical velocity the liquid can advance with a speed (and therefore momentum) that will not exceed the

sessile height, but will allow the flow to spread out into the horizontal floor of the cavity [27]. During this event, there is much activity at the front of the advancing drop. As the front advances the oxide film must be continually ripped and re-formed in order to expand the volume enshrouded by the once contiguous film.

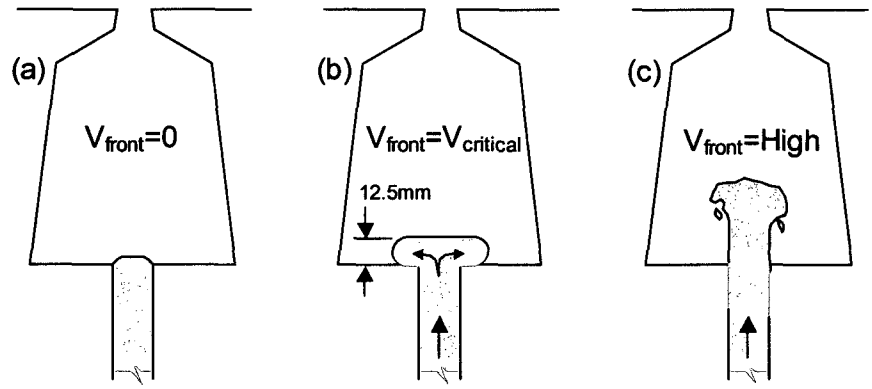

Figure 3.11: At the extremes of liquid front velocity entering a cavity within the mould; a) zero, b) critical and c) high. After Campbell 1991 [16].

Thus, the film will tear at the newest, thinnest/weakest location, which happens to be more flexible amorphous oxide, leaving an opening for the advancing liquid to escape from while the film sheet remains attached and intact with the older stronger portion of the film further behind the advancing front. In this scenario, as illustrated in Figure 3.12, the newly broken film now floating on the top surface is in effect extended or grown by the new film forming on the newly exposed aluminum just rushing out from under this older film. Likewise, the newly broken film that was on the lower side of the break (toward the mould surface) is freed to lie down beneath the advancing front, only to be replaced by newly formed film. It has been submitted (in Section 3.3.4) that by pouring the molten metal out onto a flat plate and measuring the resulting height of the pour, one can obtain an indirect measurement of the

critical velocity [27]. The two, height, and calculated $V_{critical}$, indeed coincide nicely.

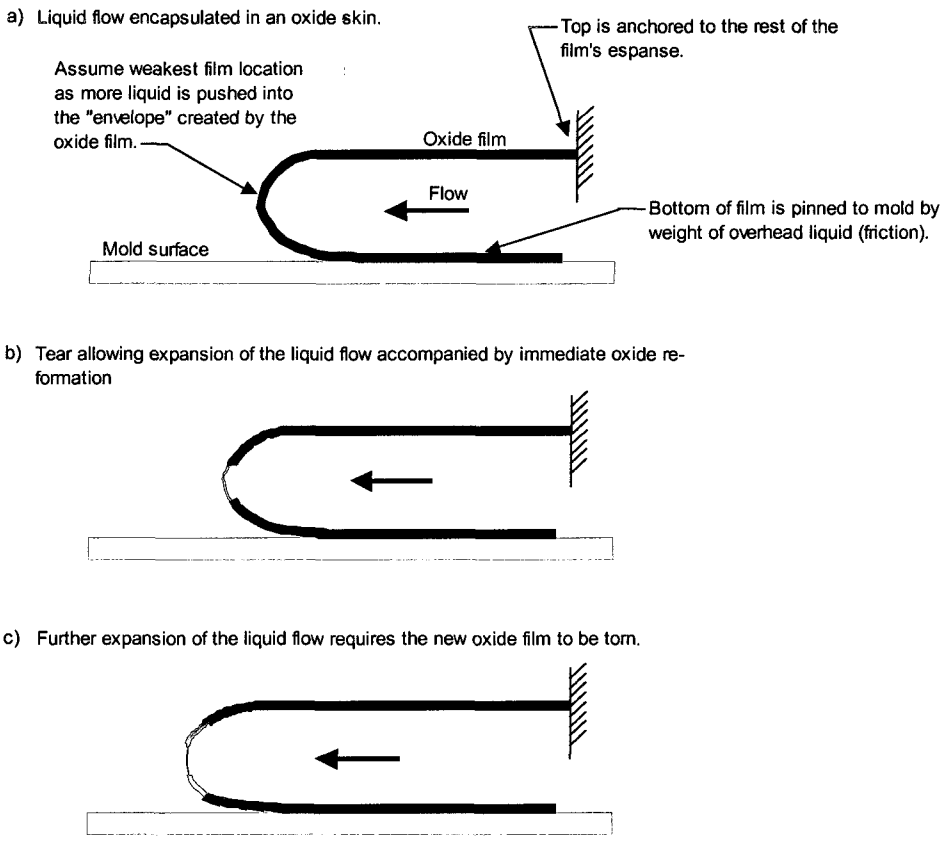

Figure 3.12: Liquid aluminum enveloped in an oxide film a) time zero, thick (dark) oxide film encapsulates the liquid, b) A later moment where the film has been stressed enough to tear allowing liquid to escape and thin new film forms (purple), c) the process is repeated at still a later moment with the oxide layer aging and thickening as it is pushed away from the region of tearing. Note how the original (thick dark) film has not moved with the flow, but is being pushed both to lie on top of and below the flow while new younger and thinner lighter purple oxide extends the layer. The actual location of the tear is unknown and is not the subject of this paper, however the concept applies equally regardless of the tear location.

The velocity of this advancing front again must remain at or below the critical velocity so that the film can be broken/re-grown in a laminar fashion without being subjected to such a degree of surface turbulence that would chaotically break, fold, and draw these pieces of film into the bulk liquid creating even more double films [16]. During the filling of a vertical section, the same sequence of events will occur -oxide tear –liquid emerge – oxide

formation – oxide thicken –oxide tear etc. As long as the critical velocity of 0.5 ms^{-1} is not exceeded, the film will be captured against the walls of the mould to become the surface of the casting where it is harmless, as opposed to being broken into fragments, folded to entrap air then being entrained into the liquid resulting in casting defects [30]. Note that the surface oxide always entrains as a double oxide, folded dry side to dry side. Oxide films can only be introduced into the melt in this state, even if a film is pushed into the melt to try to create a single immersed film, it will be surrounded by two new non-wetting surfaces [31]. Figure 3.13 depicts the process of quiescent filling resulting in surface oxide being placed against the walls of the mould.

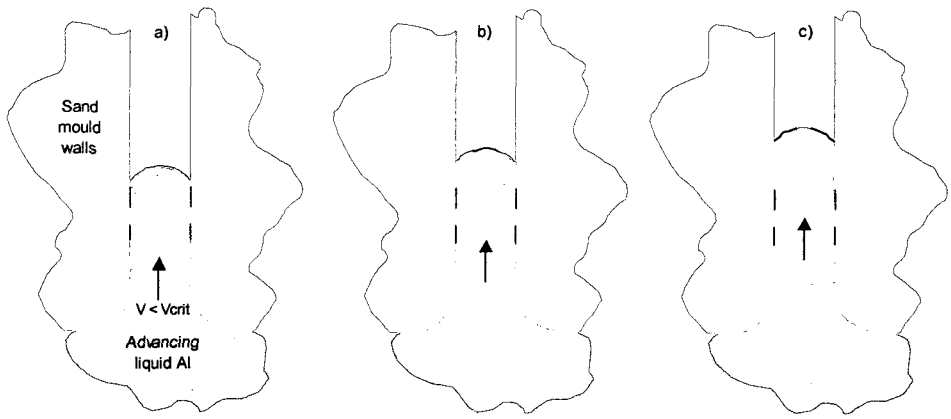

Figure 3.13: Quiescent filling of a vertical passage within a mould. a) The oxide layer atop the liquid (red) is forced to rip open and is then pushed toward the mould wall to accommodate the rising fluid. The freshly exposed aluminum quickly oxidizes to form a new film (blue)which then rips as shown in b), is then is pushed toward the wall while new film (black) is formed, and so on as the process is repeated in c).

3.3.6 Managing the Oxide; Key Role of the Runner

Combining the above quiescent filling phenomenon and the sessile height characteristic leads to the to the heart of this research. A runner designed with the sessile height in mind, (i.e. with a ceiling at the natural height), may be able to avoid oxide

disruption by surface turbulence and thus avoid the air entrainment that accompanies such activity. This would happen because of two supporting factors: 1) The aluminum front speeding down the runner will at all times touch the ceiling of the runner which will preclude surface turbulence from being able to disturb and entrain the oxide film and air associated with it, and 2) Any surface turbulence that may be present just beneath the film would not have any effect on an oxide layer that is "supported" by or even "stuck" to the ceiling. Professor John Campbell presents this concept in his Castings book series; however the method of filling the runners proposed therein uses gravity. The shape of the sprue and runner are the controls over flow velocity which is already well above the critical velocity due to the falling of the metal down the sprue [15]. Figure 3.14 presents the idea of the sessile runner as applied to the Cosworth Process of filling a mould. Since the aluminum velocity is largely controlled by the electromagnetic pump, the runner need not control the velocity, but only deliver the aluminum unharmed to the in-gates leading to the risers.

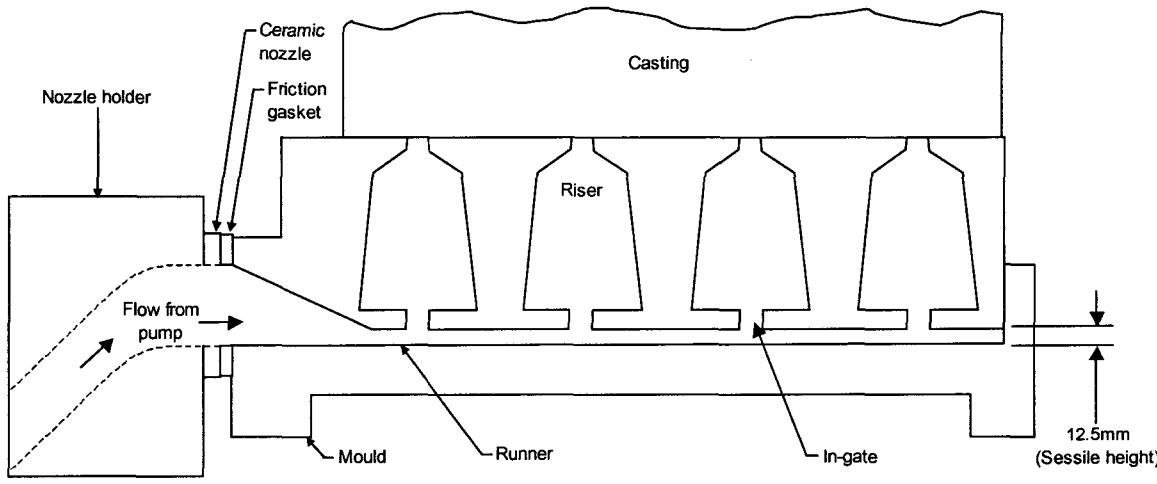

Figure 3.14: Cross-section of a sessile runner.

Fuoco and Corrêa's work [32] approaches the same problem, that is, bubbles in the casting

due to oxide films being disrupted, folded and drawn into the melt along with the air bubbles they encapsulate. They propose different designs of runners as seen in Figure 3.15 to control velocity and thus avoid the entrainment problem. This practice works, as shown in their case histories, wherein the symptom of bubbles disappears with the application of the "thin tapered runner". Again the casting process associated with this work is gravity pour in which the melt purity is already somewhat destroyed by the initial filling of the sprue. The installation of the filter is seen to help remove these newly formed oxides, but more importantly, to slow the flow to below the critical velocity.

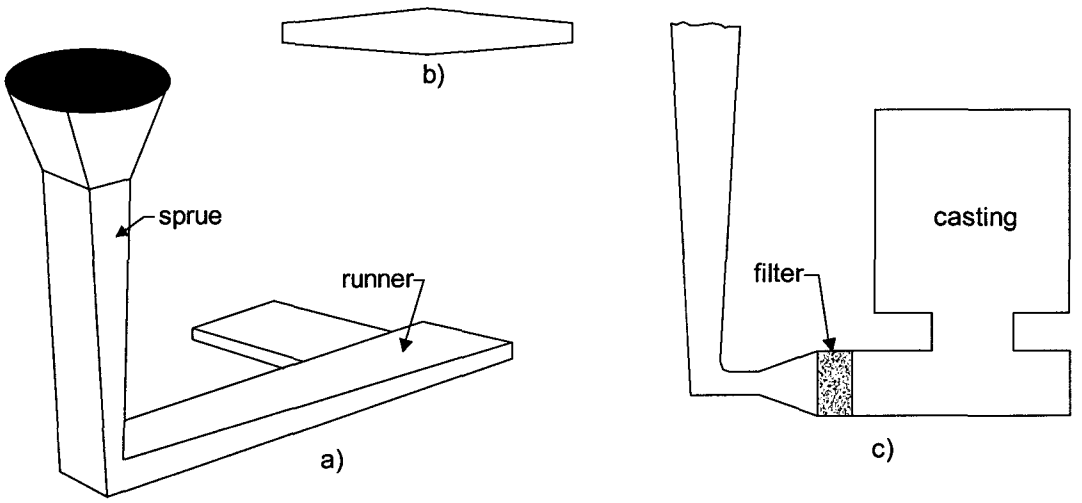

Figure 3.15: Runner designs used by Fuoco and Corrêa; a) tapered thin and wide sprue associated to thin and wide runner -designed to maximize the effect of frictional forces and to reduce the metal flow velocity, b) cross section of runner, and c) schematic of gating system with foam filter with cross section designed to keep the metal flow velocity lower than 50cms^{-1}. After Fuoco and Corrêa 2001.

The filter works because of the liquid aluminum's inherent resistance to penetration of the pores of the filter by the action of surface tension, delaying the entry into the filter until the sprue has at least partially filled [16]. Fuoco and Corrêa [32] achieved success with and without the use of a filter, but always with a thin runner to "control the meniscus" as it is

phrased. Rezvani, Yang and Campbell [33] applied a thin "one-pass" runner to a gravity poured casting series and found the design that most minimized surface turbulence and air entrainment resulting in reduced bubble damage, yielded the strongest castings (i.e. higher mean tensile strength) (300 Mpa) compared to the castings made with traditional running/gating systems (230 Mpa) wherein bubble damage was abundant. The "one-pass" terminology is drawn from the idea that the runner height is low enough to prevent the initial wave of liquid metal from running the length of the passage and reflecting off the end wall to form a returning wave. This phenomenon results in the liquid passing the in-gates twice, once on the way down, and once on the way back. This practice forms relatively huge quantities of double oxide film, all poised & ready to be flushed up into the casting cavity. The "thin runner" concept Rezvani used agrees with the sessile height concept, but at 7 mm high, it is almost half the sessile height of 12.5 mm. The suppression of surface turbulence all the way into the mould cavity was the main purpose of the study, and proved to work. Whether the runner ceiling is the sessile height or a lesser height is irrelevant since the surface turbulence is suppressed [34], surface oxide is trapped, therefore controlled in either case. The drawback is that the thin configuration allows more heat to be withdrawn from the flow than is otherwise necessary. Ideally, the ratio of the area of flow (cross section) to the surface area should be at a maximum in order to avoid chilling the metal more than necessary while on the way to the mould, thus avoiding cold-shut defects. Again we see gravity being used as the vehicle by which the liquid metal is propelled into the mould, where the design of the runner and in-gates is critical in controlling the velocity – hence the need to make use of the larger frictional flow restriction obtained using a thinner runner.

The current work is again distinguished from prior work in that the liquid is

introduced into the mould by the Cosworth Pump in a much more quiescent manner, control of velocity under the control of the pump rather than gravity, with the exception of the section of the runner that ramps downward. This thesis is firstly a study to establish whether or not there is a relationship between liquid flow velocity down the runner of the current WAP production mould and the quantity of bubbles in the cast sample, and secondly an attempt at correcting a flaw in an otherwise robust casting process.

3.4 Methods of Quantification

3.4.1 Weibull Analysis

"The identification of good systems has also been based on sounder experimental techniques, particularly the use of Weibull statistics" [34]. In this statement, J. Campbell is referring to "systems" as the runners, in-gates, sprue design, mould filling methods etc., in short every component of the system used in making a casting. There are many variables involved simultaneously during casting, resulting in limited control over the flow of metal in a mould from one casting to the "identically" poured next. The turbulent nature of flow within the casting has given rise to variable mechanical property test results, even in "identically" cast samples, so that the predicted failure is not according to a standard distribution. Failure in ductile materials is best described by a Gamma distribution, whereas for brittle materials it has been found that the Weibull distribution is a more accurate model. The Weibull distribution (named after Waloddi Weibull) is a continuous probability distribution with the probability density function

$$F(x) = (k/\lambda)(x/\lambda)^{(k-1)}e^{-(x/\lambda)k} \qquad (7)$$

for $x>0$, where $k>0$ is the shape parameter, and $\lambda>0$ is the scale parameter of the distribution

[35, 36].

Since in brittle materials the strengths are determined by a random distribution of defects within the material, one piece of a material may contain only a small defect, while another sample of the same material may contain a significantly larger defect, or quantity of defects, which result in a large reduction in strength. The failure of an individual element of the material is assumed to result in the failure of the entire sample. Therefore a larger specimen of a material is more likely to contain a large flaw (or large numbers of flaws) and therefore is expected to have lower strength. In ductile materials, this is not the case, since the crack blunting process can occur.

Weibull defined a probability of survival, which is skewed, as are many strength and fatigue life distributions. The cumulative density function is given by the expression

$$F(j) = 1 - \exp\left[-(x-\mu)/\sigma)^{\lambda}\right] \quad \text{for } x>0 \tag{8}$$

where F(j) is the cumulative fraction of failures up to a given strength value of x (in this case UTS), σ is a position parameter where 1-1/e of the samples survive (approx 37%), μ is a lower strength boundary below which no specimen fails and λ is a width or shape parameter, referred to as the **Weibull modulus**. The greater the value of λ the more narrow the range of strengths for that population, hence, by inference, the more consistently the samples of that population contain a like quantity and nature of defects causing failure to occur at or near the same load.

The probability of a specimen surviving until a given stress is 1-F(x). Setting the lower boundary to 0, the equation becomes

$$F(j) = 1-\exp\left[(x/\sigma)^{\lambda}\right] \tag{9}$$

To reduce this to a straight-line plot, eliminate the minus sign in the exponential term,

$$1/(1\text{-}F(j)) = \exp\left[(x/\sigma)^{\lambda}\right] \quad (10)$$

Next take natural logarithms twice to obtain

$$\ln\{\ln[1/(1\text{-}F(j))]\} = \lambda \ln(x) - \lambda \ln(\sigma) \quad (11)$$

The expression on the left hand side can be plotted against the natural logarithm of x. A regressed line through this data yields a slope λ (Weibull modulus), and intercept $-\lambda \ln(\sigma)$.

The method of probability plotting described above will be used in dealing with results gained from the present research, as it is most applicable to brittle tensile failure data. This methodology can be applied to compare the Weibull modulus of tensile specimens cast under different casting conditions with confidence that an accurate model in each case encompasses the distribution of failure probability [35].

A Weibull modulus of 11 is approximately that of an engineering ceramic while a modulus of 50 is similar to that of an aerospace forging [37].

3.4.2 Radiography (X-ray) Image Analysis

Radiograph images can be used as a means of "seeing" into a casting to determine not only the magnitude of the defect, but the quantity as well. Discontinuities within a casting can be counted, and rated in size according to published standards [38, 39]. Radioscopy, or real-time x-ray allows the technician to manipulate the part being examined to yield the optimal angle of view to accommodate for part shape. Radioscopy can also be applied to a dynamic process such as the filling of a casting, to allow the casting engineer to view the flow of liquid metal within the mould. This technique has been used to much advantage in understanding the relationship between sprue/runner/ingate designs and air bubbles within the liquid flow of the filling mould [40, 41]. The use of such an instrument presents major

advantages to the casting engineer in the diagnosing of mould filling/casting problems.

3.4.3 Scanning Electron Microscopy (SEM)

Detection/quantification of oxide content in the sample can be performed after samples have been cryogenically fractured to expose the internal structure with negligible deformation involved. The SEM sample location is determined by the x-ray imaging technique for the location of the bubble(s). The sample can then be frozen in liquid nitrogen and fractured at the bubble location. Observation of the fractured surface enables structure characterization including quantification of oxide content, and the nature of the oxide (thickness, new/old etc.) surrounding, attached to or adjacent to the bubble.

3.4.4 Other Quantification Techniques

Eddy current and ultrasonic inspection techniques are also non-destructive and have applicability to the detection of bubbles within a casting, and indeed even within a liquid metal flow. Due to the more complicated nature of the mould design to accommodate on-line ultrasonic monitoring, this technique was not used. Although both inspection techniques were available on site, it was determined that x-ray and SEM analysis of samples was sufficient in producing the necessary data.

3.5 Mechanical Properties

It has been shown that mechanical properties, especially fatigue life, suffer as the casting is filled in a more turbulent manner. Castings whose liquid metal was handled in such a way as to generate and include oxides typically possess tensile properties of Weibull 11, which is

the equivalent of a ceramic. The more the melt remains quiescent as it flows into the casting, the higher the Weibull modulus becomes until that of an aerospace forging is reached, the reason being as less and less oxides are present, fewer defect sites reside within the casting lending themselves to be initiate sites for failure. Fatigue studies revealed that cracks indeed initiate at the site of new or old oxides or entrained pores. In turbulently filled castings it was found that cracks initiate at these 3 characteristic sites. In quiescently filled castings, the new oxide and related pores were absent leaving only the old oxide films as initiation sites [21]. A mould may be designed such that all the cavity shapes promote quiescent fill and non-arresting surface movement and directional solidification characteristics, but with aluminum exposed to an improperly designed runner within the first second of mould fill, the damage is done even before the metal enters the casting chamber.

3.6 Computer Simulation of Mould Filling

Much work is being done currently to develop software that can predict many varieties of casting defects. The advantage of being able to predict a casting defect before any physical tooling or facilities are manufactured is incalculable. Currently, computational fluid dynamics is the term used by the trade in describing the software's method of determining flow characteristics within the mould, to enable prediction of flow velocity, flow path, trapped gas pockets and lapping. The software also incorporates the necessary heat transfer (conduction, convection & radiation) algorithms to allow the successful prediction of cold-shuts and shrink defects [42-44].

The ability to predict flow generated (entrained) bubbles is not, as of the time of this writing, within the capabilities of casting simulation software [45]. The modellers state that this

functionality is needed by industry, desired by casting engineers and under development within software houses, yet does not currently provide reliable results [46].

3.7 Application of the Theory to a Real Process

The data generated, and subsequent analysis performed within this thesis effort will be used to guide the future of mould design within the Nemak Corporation.

3.8 Novel Approach to this Field

This work is different from other runner related work, in that the existing runner system has never been studied scientifically for the contribution it may make to the formation of bubbles. Only generic "rule of thumb" knowledge has been applied to this runner, and that was performed during its design in 1989 [47]. The combination of the electromagnetic pump filling a sessile runner has not appeared anywhere in the literature leaving this the first study of its kind.

3.9 Advancing the Science

The available literature on this topic covers a wide range of running systems, none specifically focused on the WAP design or on any particular design for that matter, and certainly none on cylinder block head deck porosity. Runner work published to date by researchers such as J. Campbell, J. Runyouro, S. Boutorabi, Divandari, T. Isawa N. Green, S. Sulaiman, T. Keen, M. Masoumi, H. Hu, R. Fuoco and E. Corrêa lay a foundation for understanding runner systems that is needed as a platform to launch next steps, and so is

necessarily generic in nature, allowing it to act as a resource, tool, or idea with which the casting engineer can develop an application to his or her own specific case. The work of J. Campbell lays out all the fundamentals with respect to aluminum flow behaviour (oxide skin, flow-ability, runner design etc.) and is also necessarily generic (i.e. "the 10 rules of castings") in nature. No direct applications of all the aforementioned development work has been published to date and so the current work is novel in this respect. This thesis is really the application of Rules 2 and 4 by J. Campbell to the 3.0L zircon sand mould at WAP. This work is advancing the engineering knowledge in this area of study by developing an application to be used in academia and in the production environment, that is a manifestation of Rules 2 and 4. This work adds to the credibility of the rules, for the casting engineer's use, and provides a valuable example that can be generically applied to any mould filled using a low pressure process (not necessarily using an electromagnetic pump) to induce flow. This work is applicable to any mould filled by a low-pressure process, or any process whereby a film-forming alloy must travel horizontally to begin its ascent into a mould.

Chapter 4

Experimental Methods

The experimental work of this project was divided into two streams, the first of which was to determine, using the production tooling from WAP to make "base cores", whether the flow within the runner system of the sand base core was a source of bubble generation. The link had already been established between the initial transient portion of the flow and the location of head deck porosity bubbles, so the scope of this thesis work was to determine the source of the bubbles.

The second stream of research involved developing a runner shape that would avoid generation of bubbles in the initial transient flow of aluminum through the runner by adhering to the principles of Vcritical 0.5 ms^{-1} and sessile flow. This work was performed in collaboration with the Engineering Simulation Department Staff of Ford Motor Company's Casting Division. This process will be discussed in further detail later in this thesis.

Casting experiments conducted in this thesis were designed to be a representation of the production process at the Windsor Aluminum Plant, not a reproduction of the process. Using the electromagnetic pump to make the subject test castings was not feasible. In lieu of the EM pump, a gravity pour system was developed. Though this method of getting molten aluminum into the mould is more prone to entraining air, oxides and the like, care was taken to minimize the distance from the ladle to the mould to minimize this effect. The effect of initial transient velocity down the ramp and throughout the runner length, and not the initial fall from ladle, was to be the controlling variable, and so long as the ladle to mould relationship was held constant for each experiment, the outcomes would be relatively comparable to one another. Since the production process conditions were not duplicated, an

absolute comparison of metrics i.e. mechanical properties, x-ray results etc., would not have been appropriate; however the comparison of casting properties subjected to different initial transient velocities within the experiment could be used as an indication of direction that could later be applied to the production process.

4.1 Experimental Procedures

Ideally, the plant production tools (core boxes) and electromagnetic pump pouring process would have been used for these experiments so that all the real metal flow conditions would apply themselves to the experimental casting process. Since this option was not feasible due to the demands of business, the parameter under study (initial transient velocity and its role in the formation of head deck porosity) was measured in the production casting-making process so that it could be duplicated/studied in an off-line experimental setting.

4.1.1 Establishing Baseline Conditions

The runner cavity is designed into the base core used in the 3.0L core package. One production 3.0L core package was instrumented with wire "probes" and cast in the production environment at WAP in order to establish the baseline values for the velocity of the initial transient down the runner. Figure 4.1 shows the test core package, or "timer" package instrumented with wire probes. Each wire, when touched with the aluminum flowing into the cavity, becomes part of a closed electrical circuit. Once this circuit is complete, the time at which the circuit was completed was recorded with an accuracy of +/- 0.1 s. In this way, the location of the initial transient was known at discrete times, and thus

its speed could be calculated. In order to capture this information during the casting of a saleable production casting, special conditions had to be imposed on the process. As described in section 3.2.7, a capacitive sensor feeds level information to the casting controller. The presence of copper probe wires within the mould affects the sensor, altering the feedback signal, and therefore the filling scheme. The solution was to program the controller to provide identical-to-production voltage to the pump without the feedback signal. Two hundred and thirty eight recent casting records were averaged to yield the voltage curve that would be applied to the pump during the timer package casting. Figure 4.2 shows the

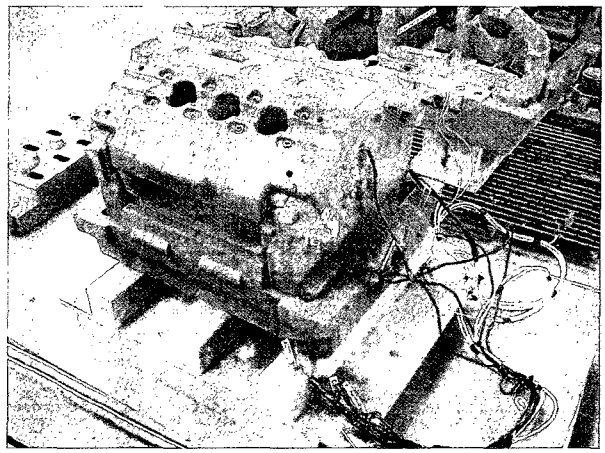

Figure 4.1: Timer Package

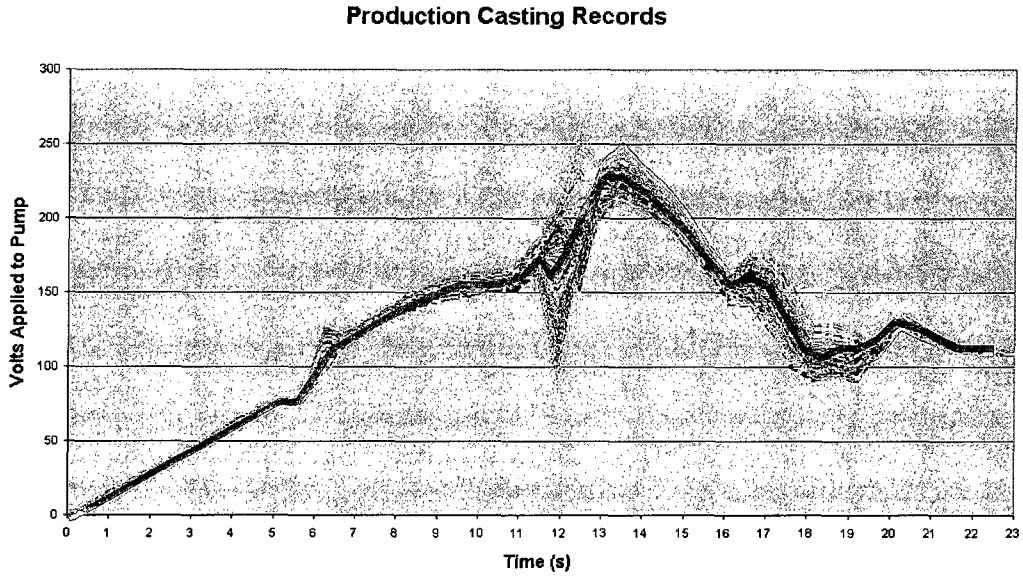

Figure 4.2: Production casting voltage records averaged (heavy line) to yield a timer package voltage profile for casting the timer package without feedback.

result of averaging these casting records. By doing this, the presence of the probe wires had no effect on the filling of the casting, producing the same metal flow in the ""timer" package as in a production casting. Figure 4.3 shows the data-recording instrument developed by the author and colleagues Dr. Glenn Byczynski and Danielle. Roberge, was used to capture all data during the pouring of the test bar castings.

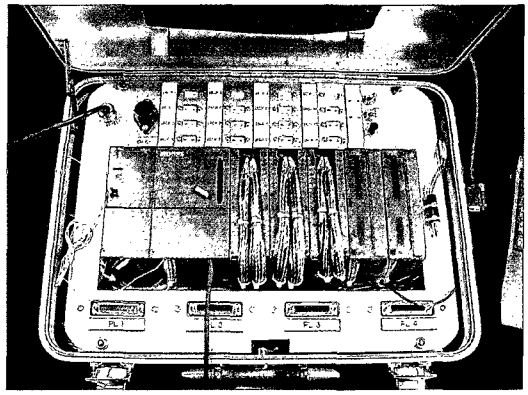

Figure 4.3: Data recorder

Within the package, the runner was outfitted with probes as can be seen in Figure 4.4. The probes were situated at the top of the ramp, bottom of the ramp, and three more probes spanning the remaining distance to the end of the runner. The data collected during casting was sufficient to establish the production casting process baseline initial transient velocity down the runner.

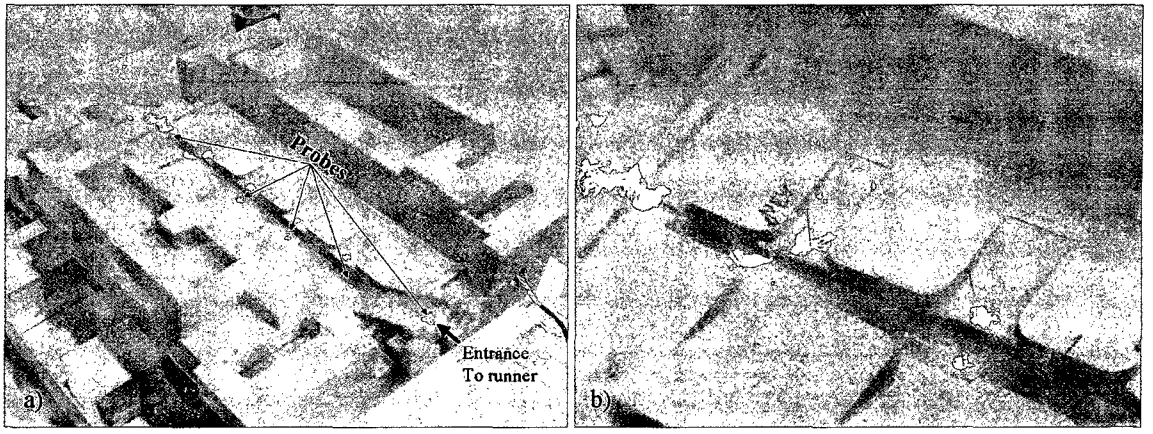

Figure 4.4: a) Base core with probes installed in runner; b) close-up of wire probes near the end of the runner.

To explore the theory that an initial transient whose velocity is less than 0.5 ms^{-1} will result in less bubbles formed within the WAP base core runner system, identical castings were made at both lower and higher velocities within each of the three phases of the experimental setup.

4.1.2 Experimental Runner Castings (Test Bars)

Each phase of the experiment was designed to have a different initial transient velocity down the runner. To accomplish this, the adjustable fixture shown in Figure 4.5 was used to hold the base core during the pouring activity. The fixture enabled the base core to be tilted at any angle from horizontal to 35°.

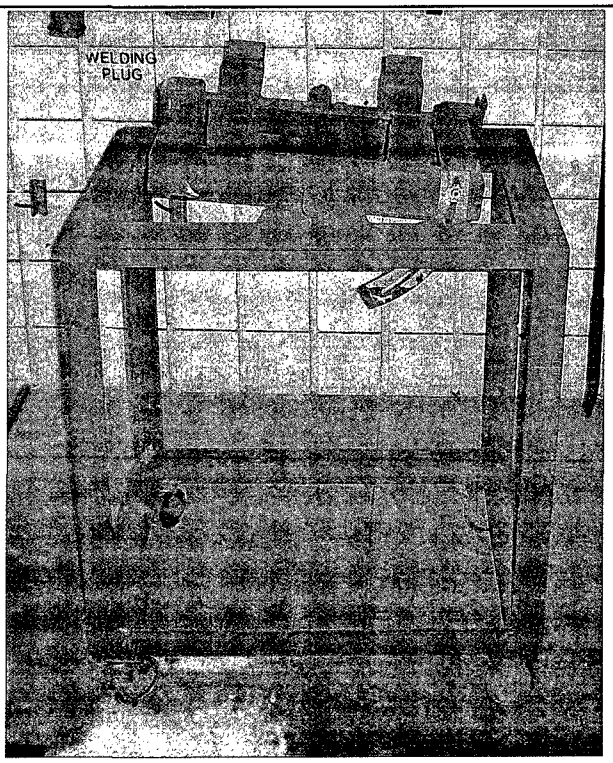

Figure 4.5: Adjustable fixture used to support base core during pouring operation.

Both the rate of metal pour, and the angle of tilt of the base core itself were adjusted until the desired experimental initial transient velocity was obtained. An ABB 5-axis Foundry robot (Figure 4.6) equipped with a ceramic ladle (Pyrotek #CC002192 – 3 lb capacity as seen in Figure 4.7) affixed to the tooling plate was used to handle the molten metal.

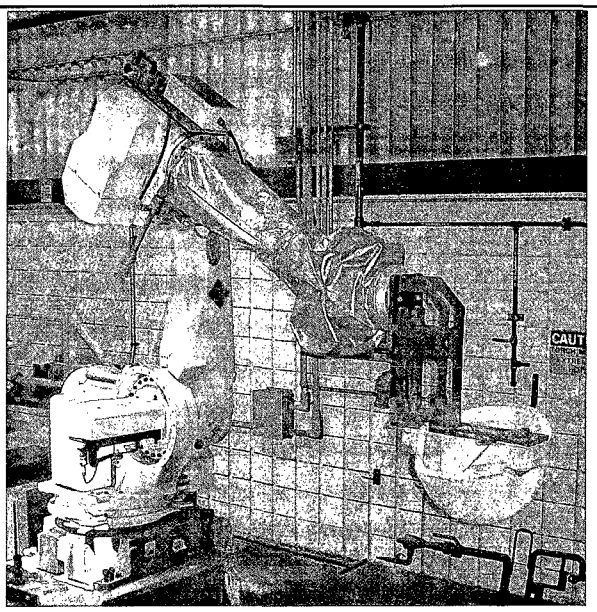

Figure 4.6: ABB robot used to pour test bar castings, shown with a large ladle used in casting cylinder aluminum heads.

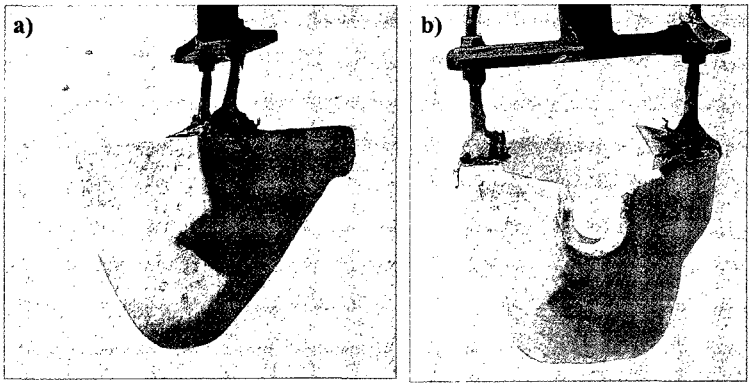

Figure 4.7: 3.5lb capacity ceramic ladle used to pour test bar castings, a) side view, b) front view.

The ladle motion was optimized to half fill the ladle by dipping it into the bath of a 15,000 lb electric holding furnace (Figure 4.8), move to the mould and pour the metal into the base core to produce a "test bar" casting.

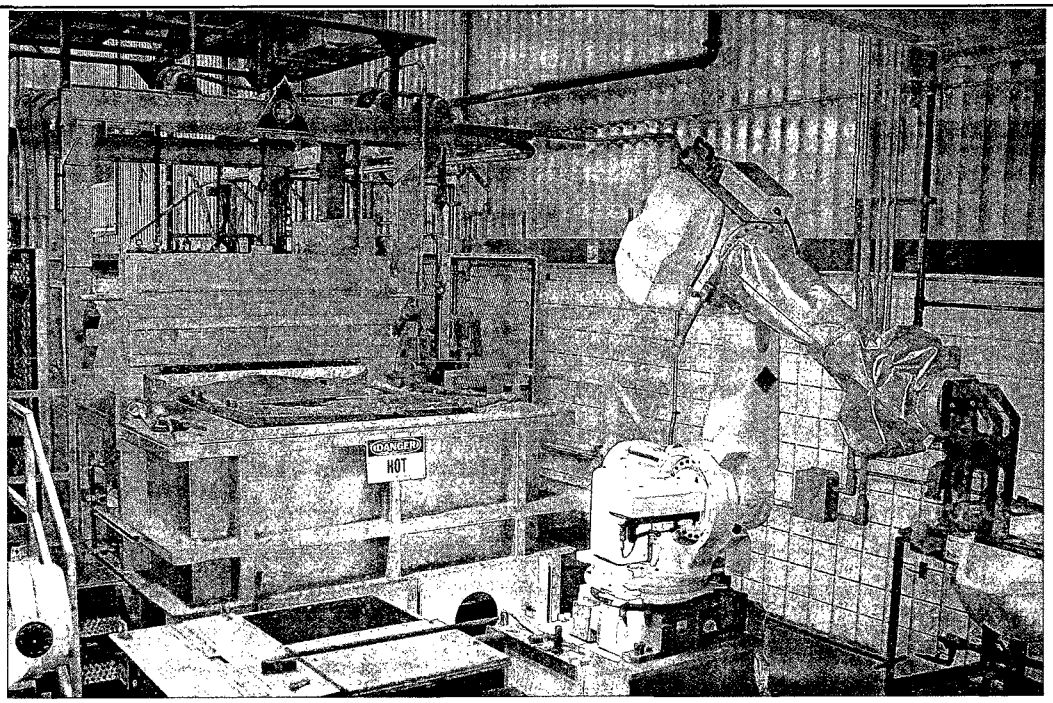

Figure 4.8: Pouring robot and electric holding furnace.

This arrangement was ideal in reducing process variation from sample to sample due to the repeatability of the robot in both filling the ladle the same amount each time, and pouring the sample identically each time.

Phase I testing consisted of pouring twenty test bar samples whose initial transient velocity down the runner was as close to the same as production as could be achieved. This was accomplished by trial and error with the robot tilting the ladle at different rates to pour metal into base core moulds instrumented with probes in the same manner as the timer package was instrumented. Eventually an acceptable rate of ladle tilt was achieved combined with the mold tilt of 0°, so that the velocity of the initial transient of the flow was approximately the same as that in the production poured timer package.

At this point the test bar casting was poured into the open mould, which had the potential to let any bubbles generated in the pour, rise to the surface and possibly disappear. Since the

defect must remain in the interior of the cast section to have an effect on mechanical properties [28] or indeed to be found in x-ray at all, a copper block (25 mm x 25 mm x 178 mm) was placed over the end of the runner cavity to act as a chill, as seen in Figure 4.9, to immediately freeze the surface, trapping any oxides and bubbles in the initial transient metal.

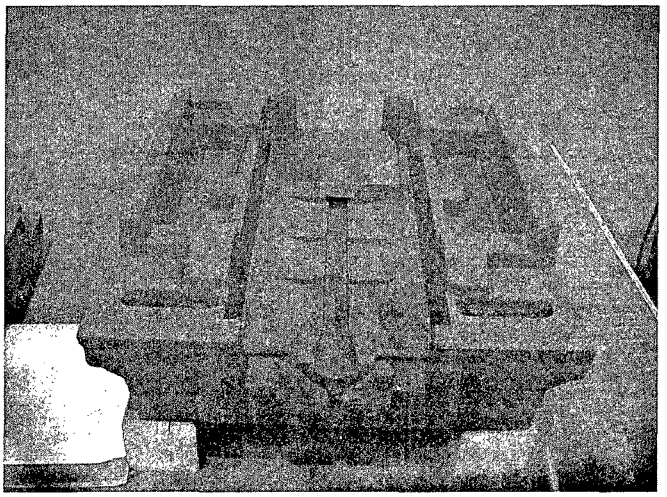

Figure 4.9: Copper plate in place ready for pouring

Subsequent to each pour, the copper plate was submerged in room temperature water to extract the heat gained during the chilling process. By cooling the chill after each use the plates were not only easier to handle, but reduced the effect of the chill plate temperature as an experimental variable.

As the metal poured into the runner behind the initial transient, the liquid elevation rose high enough to overflow the runner channel. This was a favourable condition to apply slight pressure to the metal beneath the copper chill preventing waves or movement of the surface oxide layer and ensuring a full "casting cavity" which would result in a more uniform surface finish on the sample for the benefit of x-ray contrast.

Figure 4.10 shows a typical cast sample. The "test bar" end of the sample shown in Figure 4.11 contained the initial transient of the pour and was sectioned from the rest of the casting for analysis.

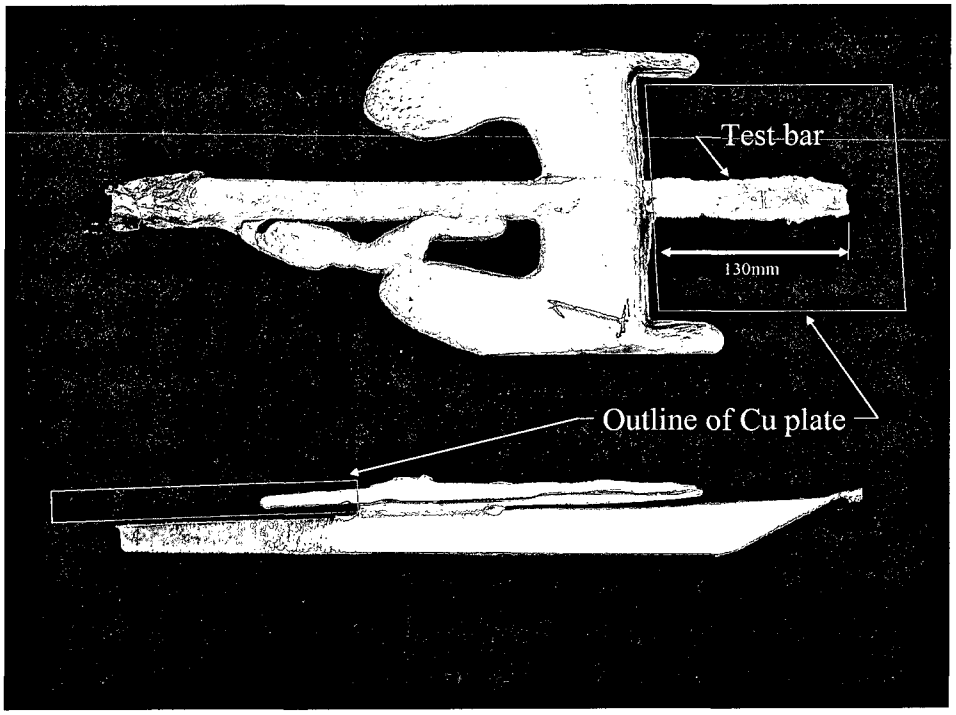

Figure 4.10: Typical cast of the runner system. The outline of the copper plate is outlined. A plan view of the casting is shown in the upper picture, with excess metal overflowing to each side of the runner channel. Sand remaining on the cast surface of the test bar can be seen in the lower picture.

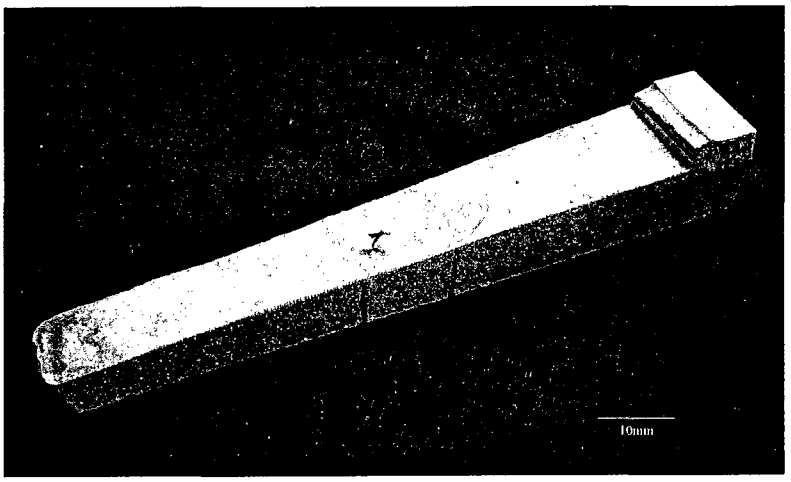

Figure 4.11: Test bar sectioned from the rest of the runner casting.

Phase II started again with experimentation of the tilt of the base core to different angles while keeping the ladle tilt motion identical to Phase I – again to reduce variation in process parameters between Phase I and Phase II results. Through extensive experimentation, an angle of 18° tilt of the base core was found to yield a 60% increase in the initial transient velocity down the runner from the baseline velocity. This velocity was chosen based on observations, since a velocity any higher resulted in such obvious turbulence that it would have surely been outside any reasonable process parameters. Twenty runner bar castings were made under Phase II conditions.

Phase III samples were made at an initial transient velocity slower than the baseline. The tilt of the base core was approximately 5° and the rate of rotation of the ladle was slowed somewhat compared with Phases I or II. This new combination was required to completely fill the runner cavity beneath the copper block. Twenty samples were poured under Phase III conditions.

4.1.3 Other Process parameters

4.1.3.1 Hydrogen Gas Content in the Melt

The RPT (Reduced Pressure Test) system seen in Figure 4.12 was used to semi-quantitatively determine the amount of hydrogen in solution with the melt. Unfortunately there are no techniques or methods that can predict the degree of porosity in cast components [48] so the RPT system was used as is currently done in most casting foundries throughout the world. The Industrial Research Chair at the University of Windsor is engaged in a large project aimed at bringing a device to market that is capable of predicting porosity in castings based on a liquid sample from the furnace. The data from this work shows that there is a higher

accuracy for quantifying percent porosity in a casting when using the proposed Enviro-AlTAP unit with reduced pressure (6 kPa) as opposed to a technique allowing ambient pressure (101 kPa) solidification of the test sample. The solubility limit of hydrogen in the melt is approximately 0.15 ml H_2/100g Al when the sample is subjected to reduced pressure where the same limit is approximately 0.2 ml H_2/100g Al when the sample is left to solidify at ambient pressure. These results show the "magnification" effect that RPT has on the quantification of porosity within a sample [48]. In the RPT procedure, a small sample of the melt is poured into a thin walled steel cup and placed into a vacuum chamber. The pressure is reduced to approximately 50 mm Hg (6 kPa) absolute pressure while the sample solidifies [49, 50]. As the sample loses temperature, the hydrogen comes out of solution to form bubbles. This process is enhanced by the low pressure to facilitate a more reliable visual comparison between a) the sample under examination Figure 4.13, and b) a standard set of pictures [14] as seen in Figure 4.14. Though the standards were made with a different sample shape, the comparison process is valid when comparing on a relative basis. Absolute numbers for hydrogen content within the melt are not used in production once the process is established with reference to the standards chart. To enable comparison levels of hydrogen with production, RPT testing was performed on the experimental furnace bath immediately before each of the casting phases, with two samples taken for each test. In each case, a rating of "1" was obtained, comparable to the standard sample number 1 in Figure 4.14. This same gas rating is seen as the norm for the production process at WAP. Identical results were obtained in each test.

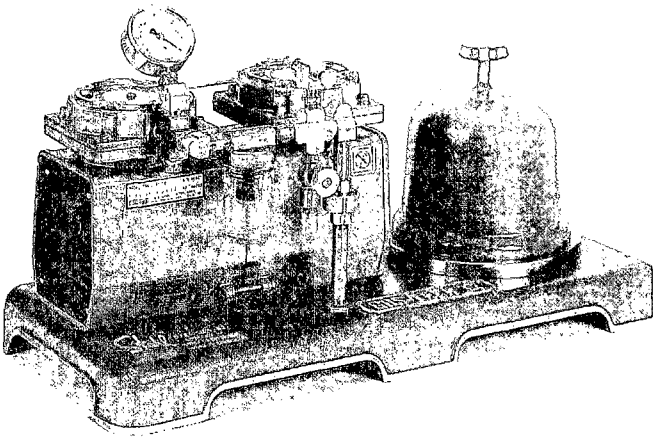

Figure 4.12: Reduced Pressure Test (RPT) equipment for detecting gas in molten aluminum alloys. (AFS 1998)

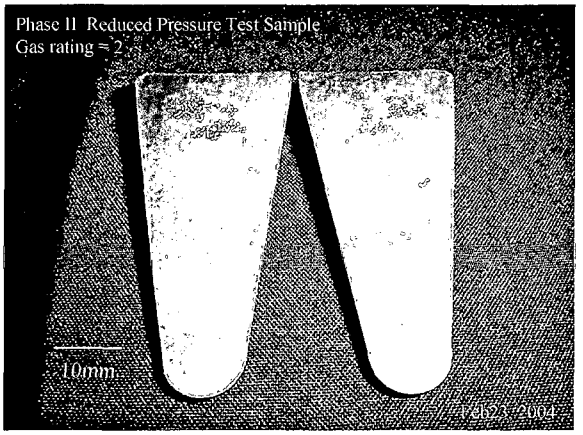

Figure 4.13. Cross-section of the Reduced Pressure Test sample

4.1.3.2 Chemical Composition Measurement

The chemical composition of the melt was tested twice prior to each casting run phase, to ensure the melt conformed to the same material specification as the production castings at WAP. Differences in the levels of silicon or iron for example, could make a difference in the fluidity of the melt, and therefore its behaviour while flowing. The chemistry was analyzed

using the ARL (Applied Research Laboratories) Model 4460 Spark Emission Spectrometer at WAP.

4.1.3.3 Temperature Measurement

The temperature of the furnace bath was checked before and after each casting run to ensure this parameter did not play the role of a variable in the experimentation (i.e. fluidity of the liquid). In each test, the temperature was 760° C as indicated by the Honeywell Temperature controller, which has an accuracy of +/- 2% (Certified March 10, 2004).

4.1.4 Sample Testing

4.1.4.1 Sample Preparation

After casting, each sample was separated from the sand mould (base core). The initial transient portion of the casting ("test bar") was cut from the rest of the runner and numbered for identification. The top and bottom surfaces of each sample were lightly ground using #80 followed by #120 grit paper and water to remove the surface sand. By removing any sand, and the rough aluminum surface that accompanies it, the x-ray images were freed of the artifacts (white specs) seen when sand is present (often mistaken for small bubbles in the aluminum). Care was taken to avoid grinding away the parent material surface, which may contain defects of interest.

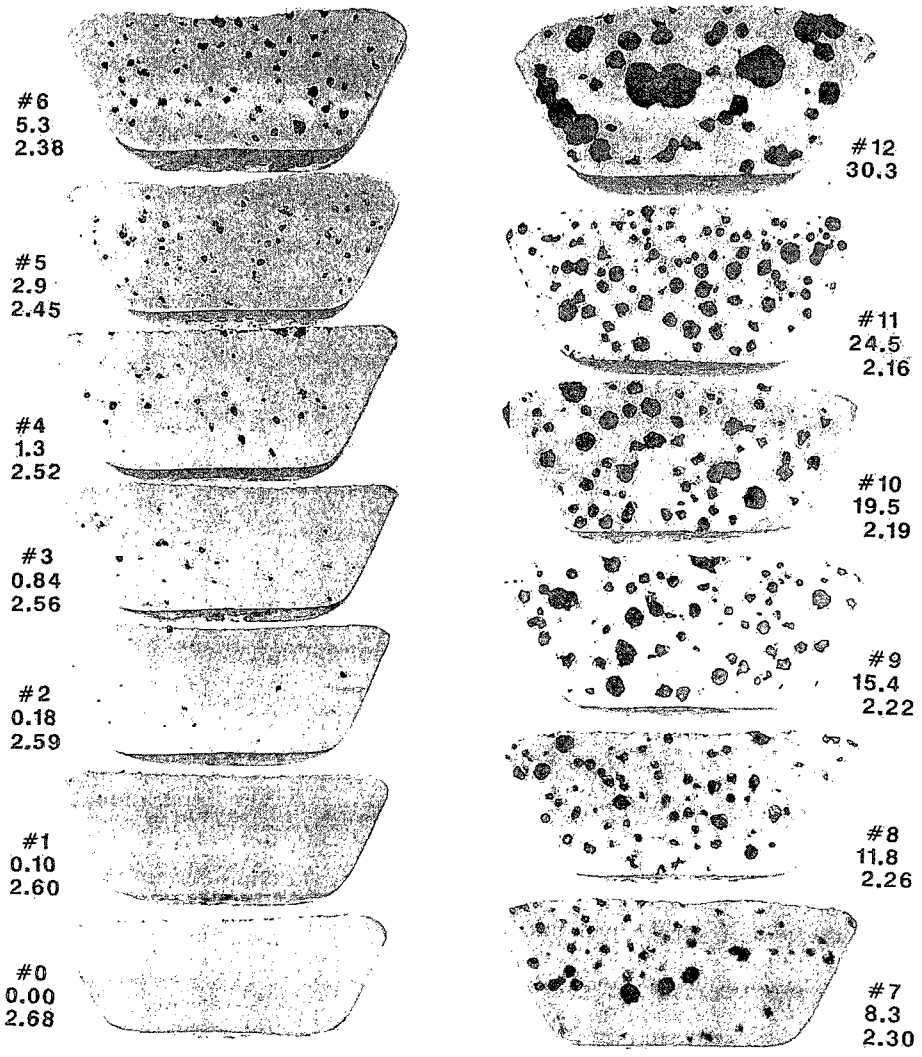

Figure 4.14: Comparison standards of cast A356.0 poured under 100mm pressure, which can be used for porosity quality control. For example, No. 1 above may be specified as the standard for high quality castings, and No. 3 for general commercial quality. The centre number for each indicates percent surface area porosity, the bottom number the density. Stahl Co.

4.1.4.2 X-ray Radioscopy

Each of the sixty test bars were subjected to x-ray radioscopy. The images were captured digitally using a Fuji AC3 digital acquisition unit with Starview software by Virtual media Integration Inc. The images were rated for defects according to ASTM Standard **E155** [38].

Each rating consisted of the size and quantity of round voids (bubbles), areas of gas porosity and shrink porosity, and any other special cause defects i.e. differences in density within the sample due to sand, large oxide particles etc.

4.1.4.3 Tensile Testing

After being subject to the x-ray testing, one half of the test bars (ten) in each phase of the experiment underwent machining to produce tensile samples. The remaining ten test bars were subjected to SEM examination to establish the morphology of the bubble defects seen in the x-ray image.

Each test bar was of sufficient length to allow machining of two round tensile specimens per ASTM Standard E 8-00 [51], each sample located end to end within the sample as depicted in Figure 4.15.

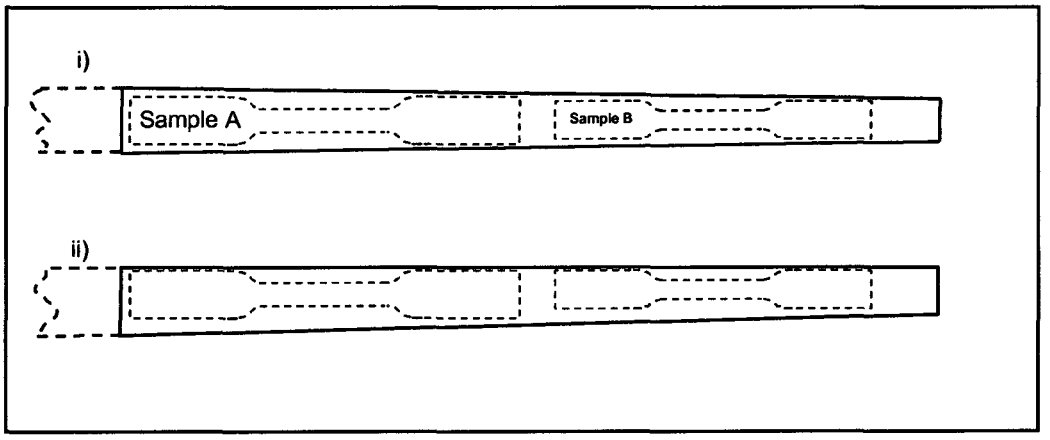

Figure 4.15: Test bar i) plan view, ii) side view, showing tensile specimen locations within. Sample A is 1.4 in. gauge length, 0.350 in. diameter; sample B is 1 in. gauge length, 0.250 in. diameter.

The testing was performed using the United Testing Machine at the Nemak Engineering Centre (calibrated June, 2004). The data was evaluated, and the Weibull modulus was

calculated to determine if the ultimate tensile strength could be used as a descriptor of the integrity of the sample

4.1.4.4 SEM Examination

After radiography, four of the remaining ten test bars were examined by scanning electron microscopy at the University of Windsor. Each of these test bars was compared with the corresponding x-ray to determine the location of an internal defect. The sample was notched at that location and fractured after being cooled in liquid nitrogen. In this way, the fracture surface was likely to contain a sample of the characteristic oxide defect for analysis – to assure that what the x-ray indicated was a bubble defect was interpreted correctly.

Chapter 5

Experimental Results

5.1 Initial Transient Velocity Results

Table 5.1 contains probe locations measured from the top of the ramp, and the calculated average velocities during each phase of test bar casting respectively.

Table 5.1: Table of probe locations and V_{IT} results.

Table of Probe Locations and the Respective Velocites Obtained in Testing						
	Probe no. & Location as Measured from Probe at Top of the Ramp (m)					
Phase	1 Top of ramp	2 Bottom of ramp	3	4	5	6 End of runner
Baseline	0.000	0.148	0.262	0.368	0.507	0.551
I	0.000	0.145	0.263	0.369	0.468	0.541
II	0.000	0.147	0.284	n/a	0.412	0.533
III	0.000	0.126	0.254	n/a	0.395	0.523
	V_{IT} at Respective Probe Locations (ms^{-1})					
Phase	1 Top of ramp	2 Bottom of ramp	3	4	5	6 End of runner
Baseline	0.0	0.7	0.7	0.7	0.7	0.7
I	0.0	0.7	0.7	0.7	0.7	0.7
II	0.0	0.7	0.9	n/a	1.0	1.1
III	0.0	0.4	0.4	n/a	0.4	0.3

A schematic of the runner is given in Figure 5.1 to assist the reader in relating the data to the real event of runner initial transient. A graphical representation of the initial transient data in Table 5.1 is presented in Figures 5.2 through 5.5. Note that the values represent the average velocity, or the total distance traveled by the frontal surface of the pour, divided by the time taken to reach the respective destination probe. The setup was tested until the desired velocity profiles were reached, then one confirmation pour was done to verify the values.

Since there were limited numbers of pours with instrumented runners, no statistical data (i.e. standard deviations) can be realized for average velocities reached at each of the probe locations.

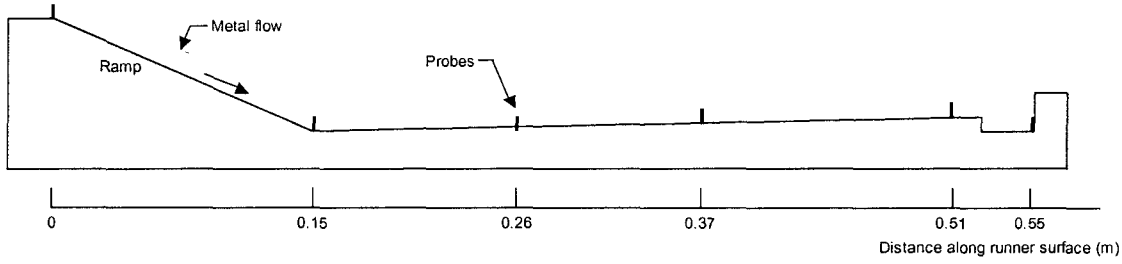

Figure 5.1: Cross-sectional schematic of runner

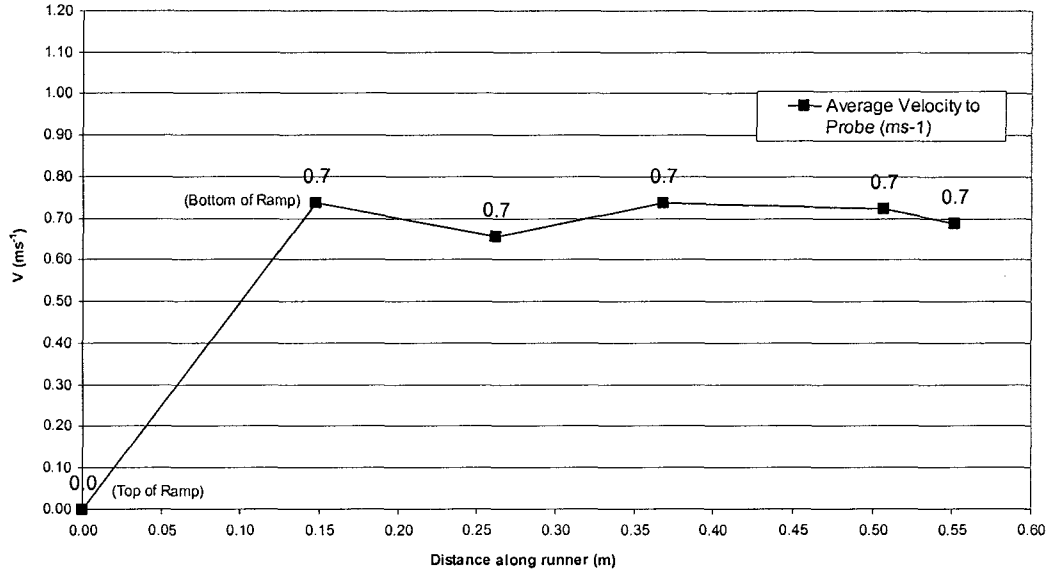

Figure 5.2: Baseline production initial transient velocity results.

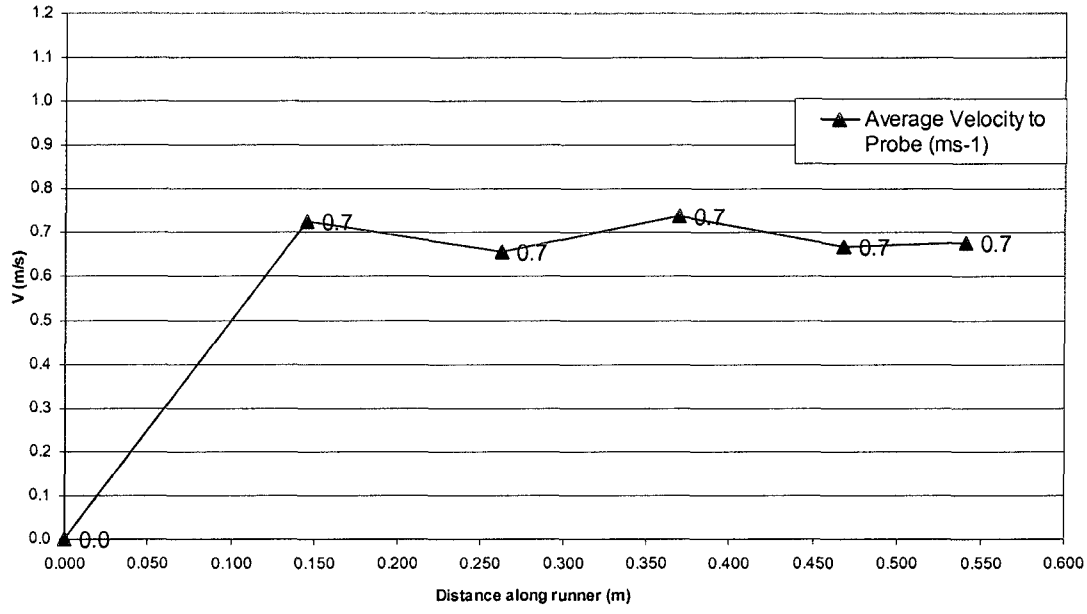

Figure 5.3: Phase I Runner Velocity Results ($V_{IT\,I}$)

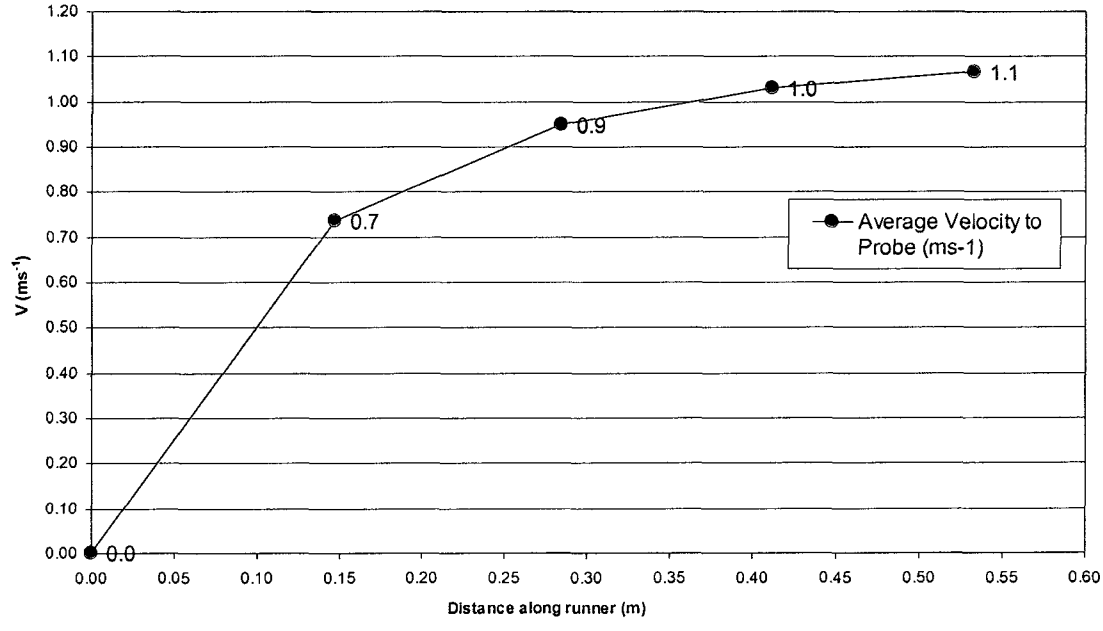

Figure 5.4: Phase II Runner Velocity Results ($V_{IT\,II}$).

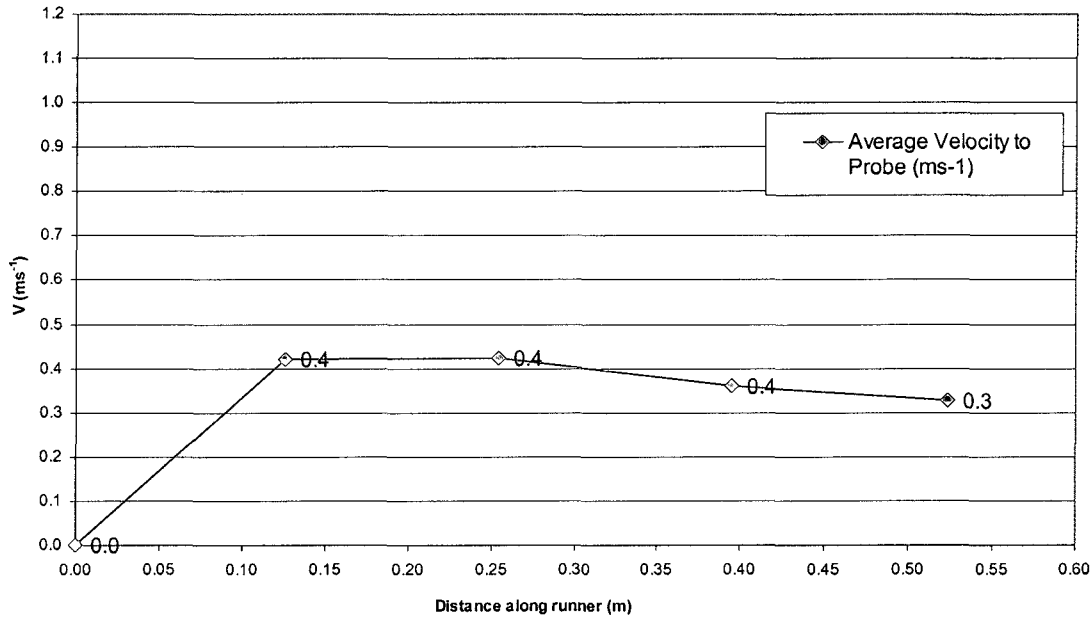

Figure 5.5: Phase III Runner Velocity Results ($V_{IT\,III}$).

5.2 X-ray Radiographic Results

The purpose of the radiographic analysis was two-fold: a) to enable the author to quantify the number and size of bubbles generated within the initial transient under different conditions of velocity, and b) to facilitate fracture sample at the location of a defect for SEM analysis. Table 5.2 contains quantity and size of bubbles entrained within the flow and then frozen within the test bar casting at the end of the runner.

Figure 5.6 displays a histogram of Table 5.2 data showing the quantity and size of bubbles generated in each phase of the experimentation.

Table 5.2: Bubble count results per x-ray examination.

Table of Radiographic Results

Gas (G1-G8) ratings are according to ASTM E-155 standard (G1 =small and G8 =large bubble sizes).
Numbers represent the quantities of bubbles found in the test bar at the respective rating.

	Phase I								Phase II								Phase III							
Sample no.	G1	G2	G3	G4	G5	G6	G7	G8	G1	G2	G3	G4	G5	G6	G7	G8	G1	G2	G3	G4	G5	G6	G7	G8
1	2								4	1	2	3	1											
2									1	1				1										
3									3															
4	2	1							1	1	2		1	1										
5	1								1	1	2	4			1									
6									1	1	3	2	1											
7	3								1	1	3		1											
8		1							3	4	1	1	2		1	1								
9									8	2		2												
10				1					3	3	1	2				1								
11	1		2						4	1	1	1												
12	1	1	2	1					4	3	1	1												
13									4	1	3			1										
14									1	1	1		1	1										
15	1		1						2	3	6													
16									1	1	1		2		1									
17									5	2			1	1	1									
18									7	1	1		1											
19	2	1							1	2	2		1	1										
20	0	1							2		2	1		1										
Total bubbles/size	13	5	5	2	0	0	0	0	57	30	32	17	12	7	4	2	0	0	0	0	0	0	0	0
Total bubble count	25								161								0							
Overall average Initial Transient velocity (ms^{-1})	0.68								1.07								0.33							

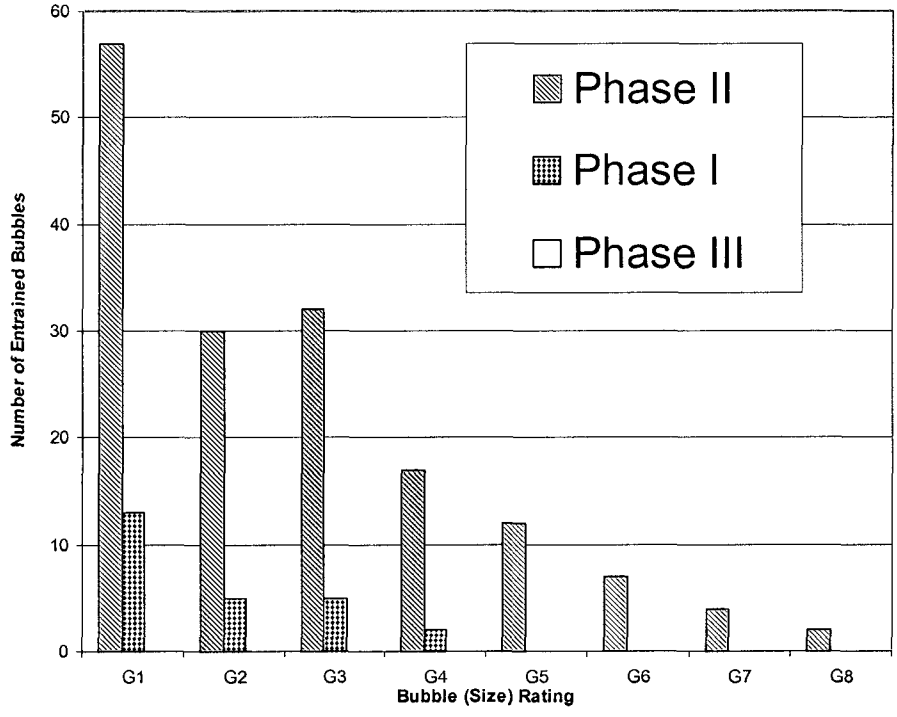

Figure 5.6: Bubble count results per x-ray examination.

Figure 5.7 displays a plot of the quantity of bubbles generated to the average velocity for the pour. Note that the velocity used to plot the data is that of overall average velocity from the top of ramp to the end of runner (i.e. each value in Table 5.1 is calculated by dividing the distance [from the probe at the top of the ramp to the subject probe], by the time taken for the aluminum to flow between the same two probes, and so the overall average velocity is the same calculation between the probe at the top of the ramp and the probe at the very end of the runner).

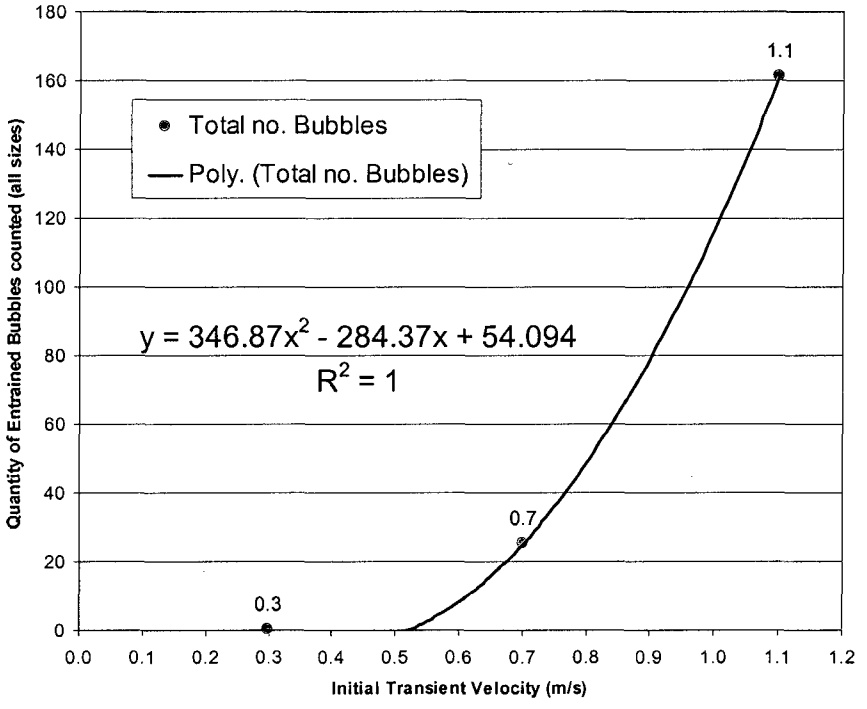

Figure 5.7: Quantity of entrained bubbles as related to runner velocity.

5.3 Tensile Strength Test Results

To test the hypothesis that the ultimate tensile strength of the sample is sensitive to the number of bubbles within a sample, two sample test bars were machined from each casting from each phase, and destructively tested in tension mode. Results are summarized in Table 5.3.

Table 5.3: Ultimate Tensile Strength Test Results.

Tensile Specimen 'A' Results

Phase I

Tensile Sample ID	Phase/ Sample Location	UTS (MPa)
1-16a	1A	260.7
1-15a	1A	266.5
1-20a	1A	264.8
1-12a	1A	265.0
1-1a	1A	249.5
1-19a	1A	272.4
1-13a	1A	255.9
1-15a	1A	236.3
1-2a	1A	255.2
1-14a	1A	263.9
1-3a	1A	243.9
1-8a	1A	270.3
1-5a	1A	257.3
1-7a	1A	261.4
1-18a	1A	271.3

Phase II

Tensile Sample ID	Phase/ Sample Location	UTS (MPa)
11-21a	IIA	152.3
11-5a	IIA	192.2
11-8a	IIA	235.2
11-2a	IIA	235.4
11-20a	IIA	237.0
11-16a	IIA	238.9
11-14a	IIA	243.9
11-4a	IIA	244.3
11-22a	IIA	248.9
11-1a	IIA	251.5
11-13a	IIA	252.4
11-7a	IIA	252.5
11-19a	IIA	254.2
11-9a	IIA	254.7
11-11a	IIA	262.2

Phase III

Tensile Sample ID	Phase/ Sample Location	UTS (MPa)
111-8a	IIIA	208.2
111-6a	IIIA	209.9
111-11a	IIIA	214.2
111-13a	IIIA	216.0
111-10a	IIIA	217.4
111-17a	IIIA	217.9
111-16a	IIIA	218.2
111-19a	IIIA	218.6
111-1a	IIIA	220.0
111-18a	IIIA	220.4
111-12a	IIIA	223.1
111-3a	IIIA	225.5
111-2a	IIIA	226.8
111-7a	IIIA	227.5
111-20a	IIIA	237.7
111-4a	IIIA	238.2

Tensile Specimen 'B' Results

Tensile Sample ID	Phase/ Sample Location	UTS (MPa)
1-3b	1B	284.7
1-8b	1B	271.6
1-5b	1B	236.6
1-14b	1B	268.9
1-16b	1B	260.3
1-2b	1B	269.4
1-1b	1B	273.8
1-13b	1B	273.4
1-19b	1B	265.0
1-12b	1B	276.7
1-7b	1B	278.0

Tensile Sample ID	Phase/ Sample Location	UTS (MPa)
11-7b	IIB	186.2
11-21b	IIB	225.2
11-2b	IIB	238.5
11-13b	IIB	248.1
11-17b	IIB	250.1
11-16b	IIB	251.6
11-14b	IIB	252.4
11-11b	IIB	256.1
11-9b	IIB	257.2
11-22b	IIB	258.5
11-19b	IIB	259.9
11-6b	IIB	260.0
11-5b	IIB	262.0
11-1b	IIB	265.0
11-8b	IIB	268.9

Tensile Sample ID	Phase/ Sample Location	UTS (MPa)
111-11b	IIIB	222.5
111-6b	IIIB	225.9
111-13b	IIIB	233.0
111-18b	IIIB	233.8
111-20b	IIIB	234.0
111-17b	IIIB	234.2
111-1b	IIIB	234.3
111-2b	IIIB	234.3
111-8b	IIIB	238.6
111-16b	IIIB	238.9
111-19b	IIIB	239.9
111-4b	IIIB	240.6
111-7b	IIIB	240.6
111-10b	IIIB	245.4
111-3b	IIIB	263.8
111-12b	IIIB	274.4

Table 5.4 contains a summary of tensile testing on both the 'A' and 'B' portions of the test bars.

In addition, to test the hypothesis that the Weibull modulus of each tensile sample's ultimate tensile strength (UTS) is related to the number of bubbles within a sample, the calculations were performed, plotted and analyzed. Results are found in Section 6.4.

Table 5.4: Summary of tensile testing results.

Summary of Tensile Testing Results - UTS (Mpa)

Phase I		Phase II		Phase III	
'A' Tensile Samples		'A' Tensile Samples		'A' Tensile Samples	
Statistic	Value	Statistic	Value	Statistic	Value
Min	236.3	Min	152.3	Min	208.2
Max	272.4	Max	262.2	Max	238.2
Std. Deviation	10.3	Std. Deviation	28.5	Std. Deviation	8.4
Average	259.6	Average	237.0	Average	221.2
'B' Tensile Samples		'B' Tensile Samples		'B' Tensile Samples	
Min	236.6	Min	186.2	Min	222.5
Max	284.7	Max	268.9	Max	274.4
Std. Deviation	11.6	Std. Deviation	20.5	Std. Deviation	12.9
Average	269.3	Average	249.3	Average	239.6
Average (A & B)	264.5	Average (A & B)	243.2	Average (A & B)	230.4
Overall Avg. V_{IT} (ms^{-1})	0.7	Overall Avg. V_{IT} (ms^{-1})	1.1	Overall Avg. V_{IT} (ms^{-1})	0.3

Figure 5.8 displays the tensile results found in Table 5.4 graphically.

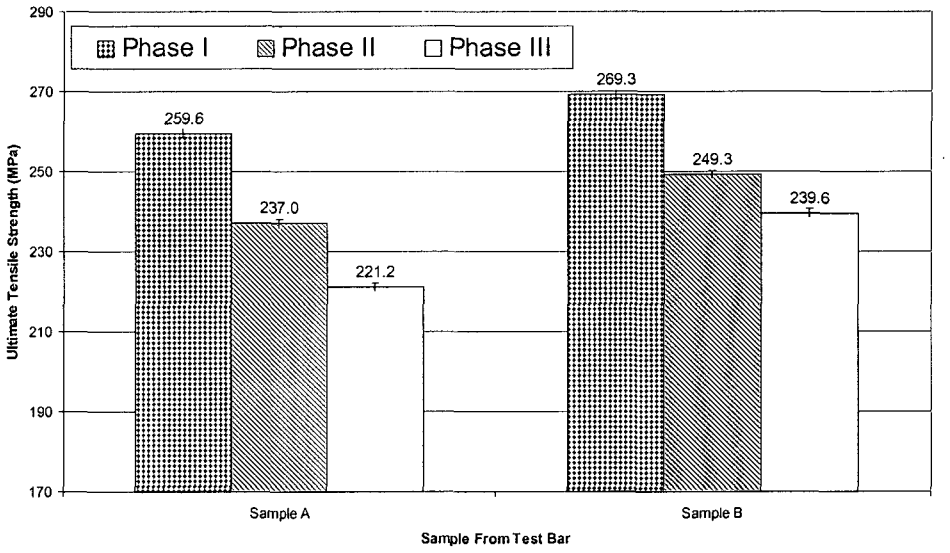

Figure 5.8: Ultimate tensile strength test results for each phase of testing, and each of the two test bars A & B taken from each cast sample.

5.4 SEM Observations

Several test bars were analyzed by x-ray to determine the location of an internal bubble. The location was marked on the bar, and steps were then taken to fracture the bar through the bubble defect. Figure 5.9 shows a typical cryogenic fracture surface studied using scanning electron microscopy. The nature of each bubble was examined and all bubbles observed were found to be lined with thin (new) wrinkled films of oxide, indicating that the bubble was formed by inclusion of air during mould fill. Figures 5.10 and 5.11 represent typical SEM observations of the morphology of the inside of a bubble within the test bar. This oxide morphology is typical of an entrained bubble of air. The morphology of the interior of the cavity was smooth and wrinkly, with some dendrite tips poking into the cavity.

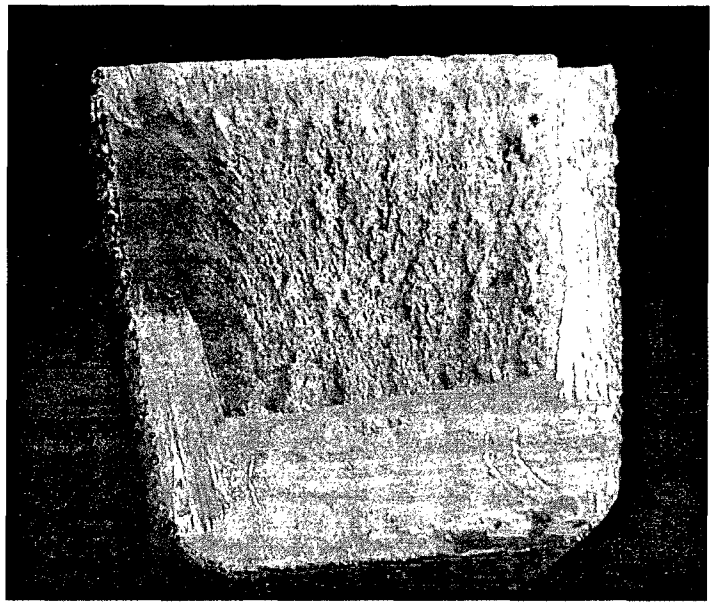

Figure 5.9: Test sample fractured for SEM study.

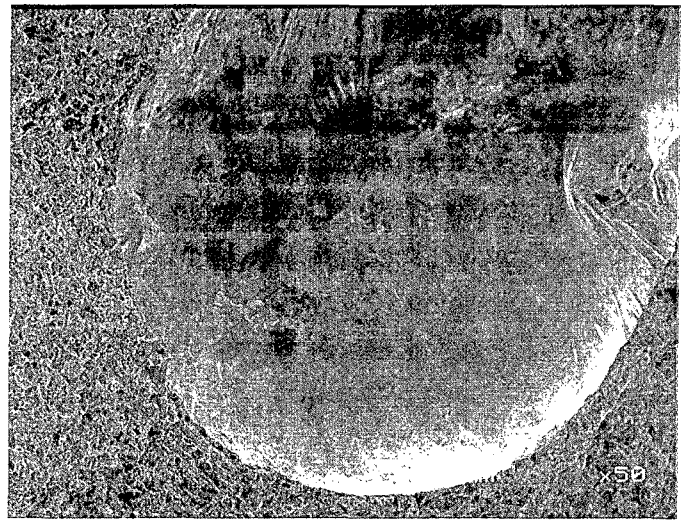

Figure 5.10: Phase I Sample 6 –Smooth oxide film lining the inside of a bubble.

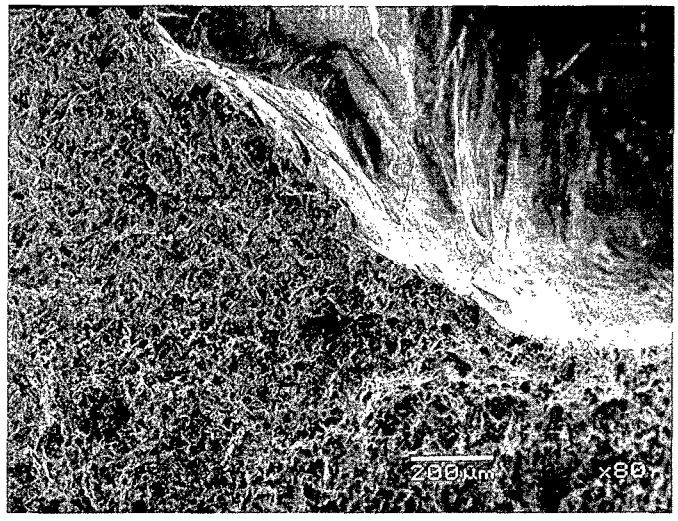

Figure 5.11: Phase I Sample 6 –Slightly wrinkled oxide film lining the inside of a bubble.

5.5 Test Bar Micro-structural Observations

Tables 5.5 and 5.6 contain results of secondary dendrite-arm spacing (SDAS) measurements and the standard deviations thereof respectively, taken at five locations across the cross section of a Phase II test bar, and a Phase III test bar. The measurements taken at location 1 are taken near the surface of each test bar that was in contact with the copper chill plate.

Location 5 measurements are taken nearest the surfaces in contact with the sand of the runner mould (refer to Figures 5.12 & 5.13).

Table 5.5: SDAS Measurements on sectioned test bars (100X magnification).

Phase II Sample SDAS Measurements (μm) (Sample size of 1)						
Location	1 Top of sample (against Cu)	2	3	4	5 Bottom of sample (against sand)	Average
Sample II-7, Surface 1	13.9	16.7	20.2	21.4	19.4	18.3
Sample II-7, Surface 2	12.9	14.0	18.1	19.5	19.7	16.8
Average II	13.4	15.4	19.2	20.5	19.6	**17.6**
Phase III SDAS Measurements (μm) (Sample size of 1)						
Sample III-5, Surface 1	16.1	18.0	19.7	23.2	25.2	20.4
Sample III-5, Surface 2	17.6	21.4	22.3	26.4	26.6	22.9
Average III	16.9	19.7	21.0	24.8	25.9	**21.7**

Table 5.6: Standard deviation of SDAS measurement data.

Std. Deviation of SDAS measurements (μm)					
	1 Top of sample (against Cu)	2	3	4	5 Bottom of sample (against sand)
Sample III-5, Surface 1	1.9	2.2	3.5	3.9	3.8
Sample II-7, Surface 1	1.9	3.3	2.3	3.6	4.5
Sample III-5, Surface 2	2.1	3.0	1.9	4.1	4.3
Sample II-7, Surface 2	1.6	2.4	3.0	2.3	3.2

In addition to the above measurements, metallographic observations (200X magnification) made on each sample revealed the percent porosity to be zero in each case.

Figure 5.15 is a plot of the SDAS data in Table 5.6.

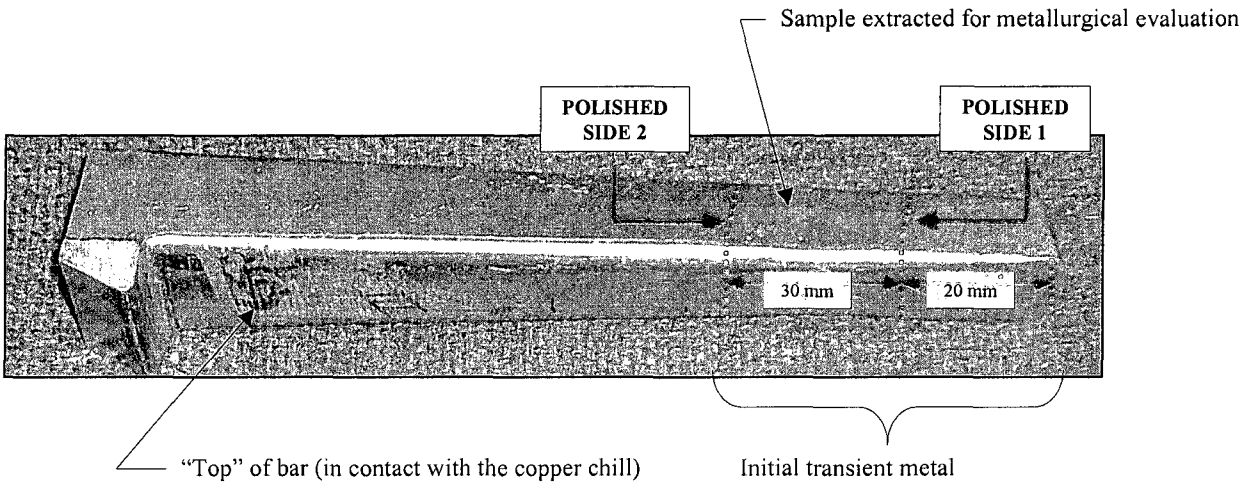

Figure 5.12: Typical test bar cut for DAS micro-structural evaluation.

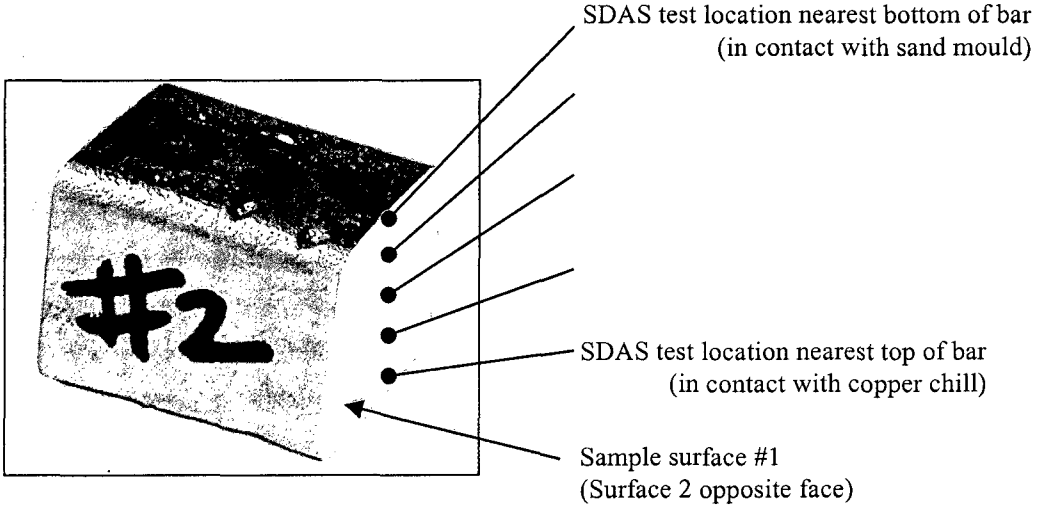

Figure 5.13: Extracted test bar sample for metallurgical evaluation (shown here upside down).

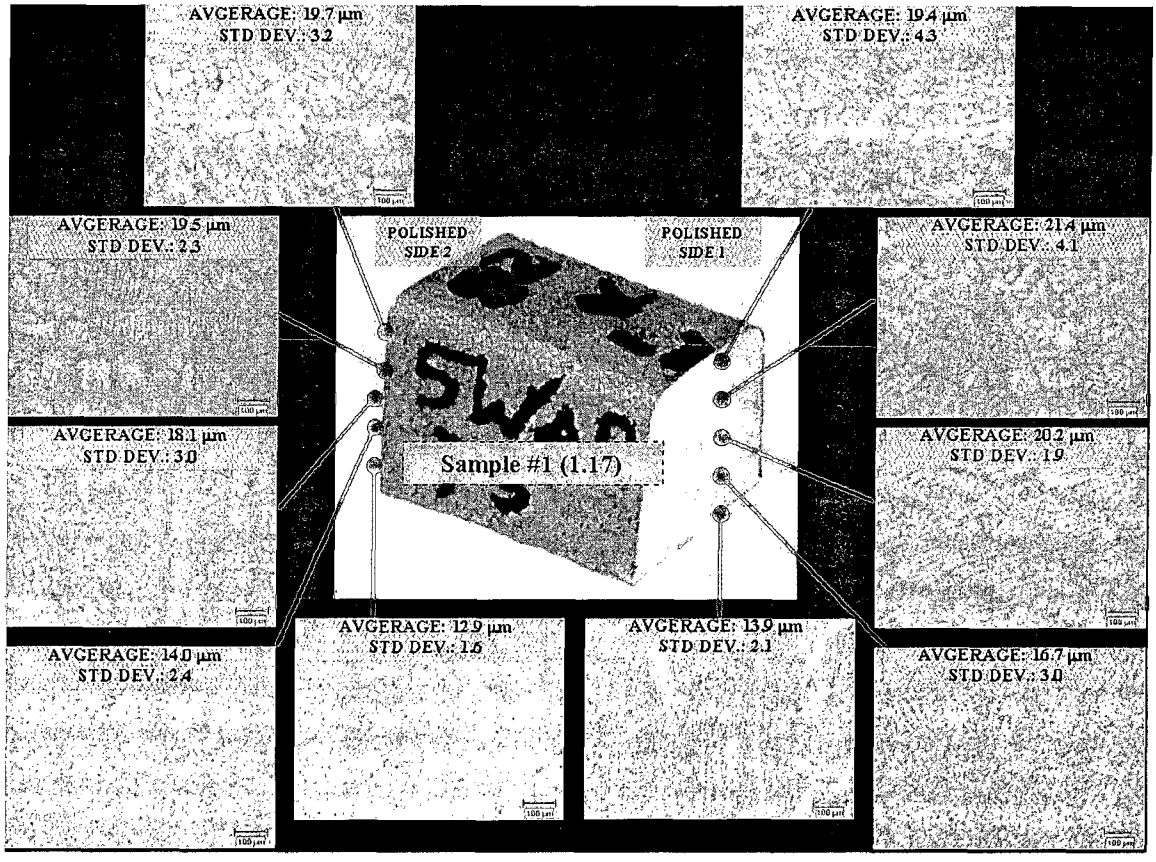

Figure 5.14: SDAS measurements and micrographs.

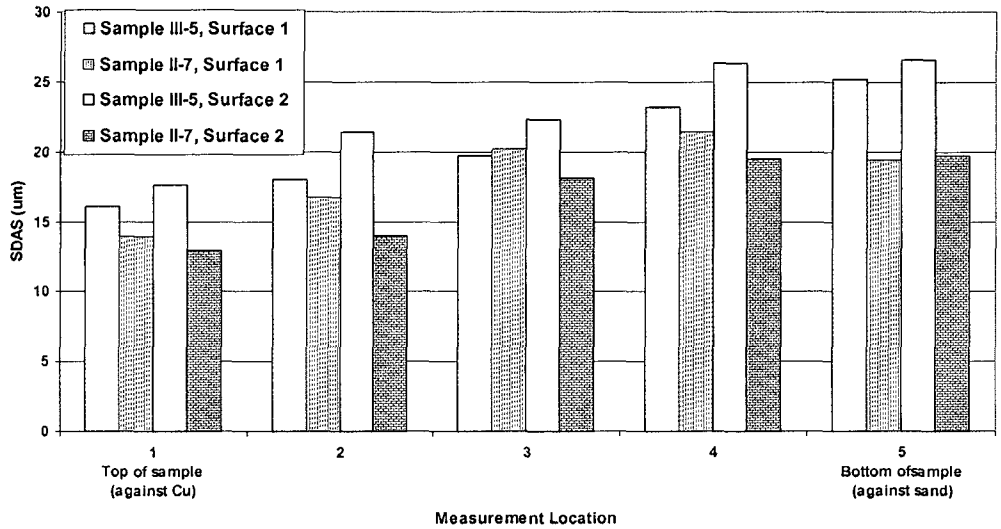

Figure 5.15: SDAS measurement results from five locations (Top=Nearest the surface touching the copper chill, Bottom= nearest the surface touching sand) within each of two sections (surfaces 1 & 2) of test bars from Phases II and III.

5.6 Fill Simulation of Current and Sessile Runner Designs

Figures 5.16, 5.17 and 5.18 show the highest velocity events during fill in the Magma simulation of the current production runner design.

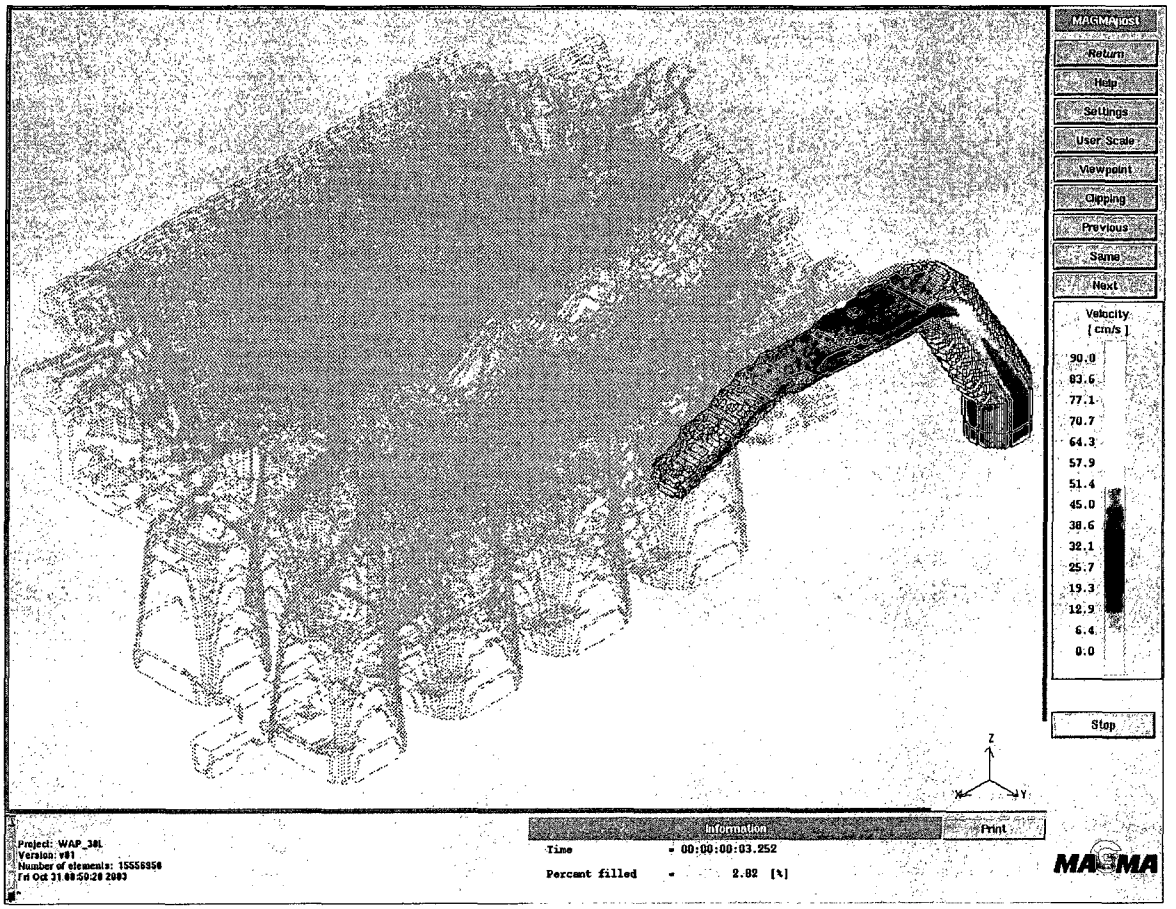

Figure 5.16: MAGMA 3.0L cylinder block fill simulation-current runner@ 3.2 seconds; Initial Transient (IT) is only half way down the ramp and V_{IT} is already nearly 0.7 ms^{-1}.

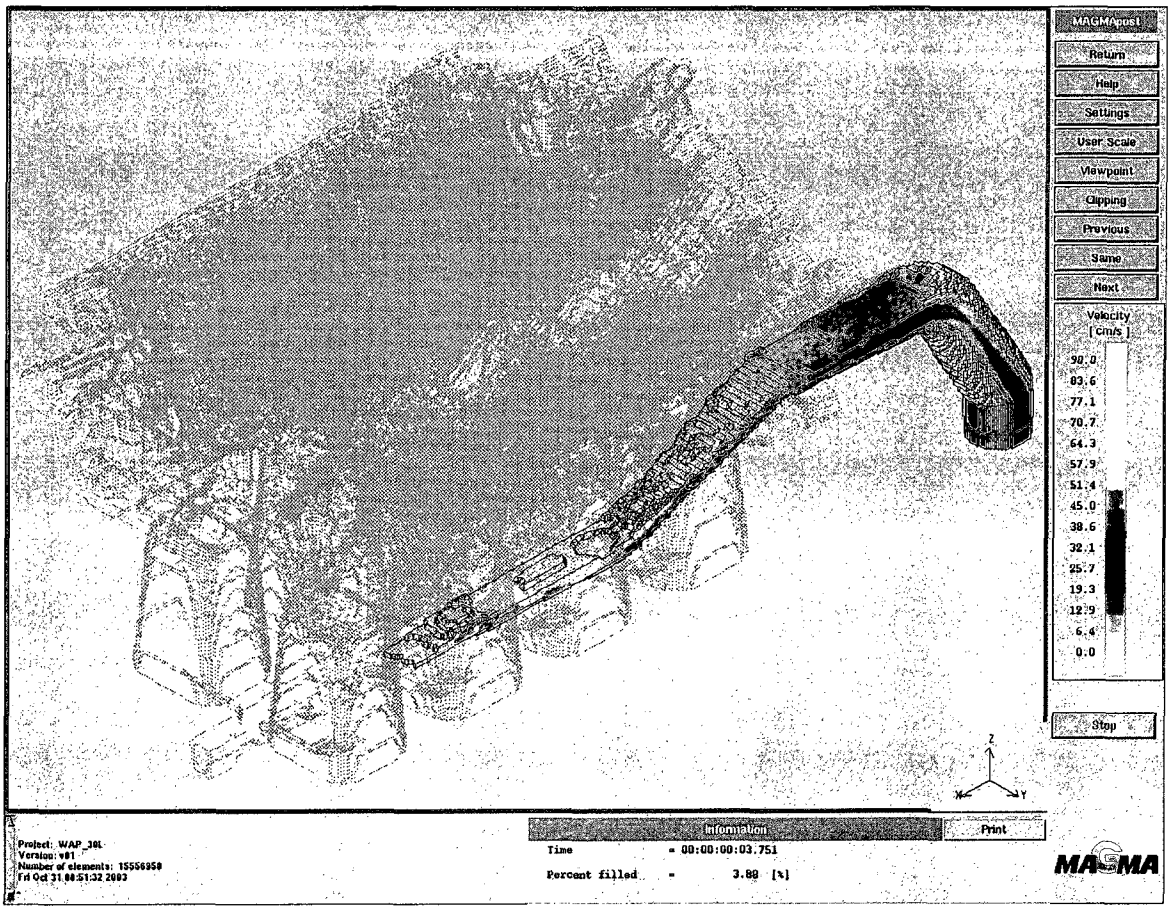

Figure 5.17: MAGMA 3.0L cylinder block fill simulation-current runner@ 3.2 seconds; IT is more than half way down the runner's length. V_{IT} remains at approx. 0.7 ms^{-1}. Note the higher velocity nearest the bottom of the ramp during a time when the aluminum in the runner is exposed to air (white).

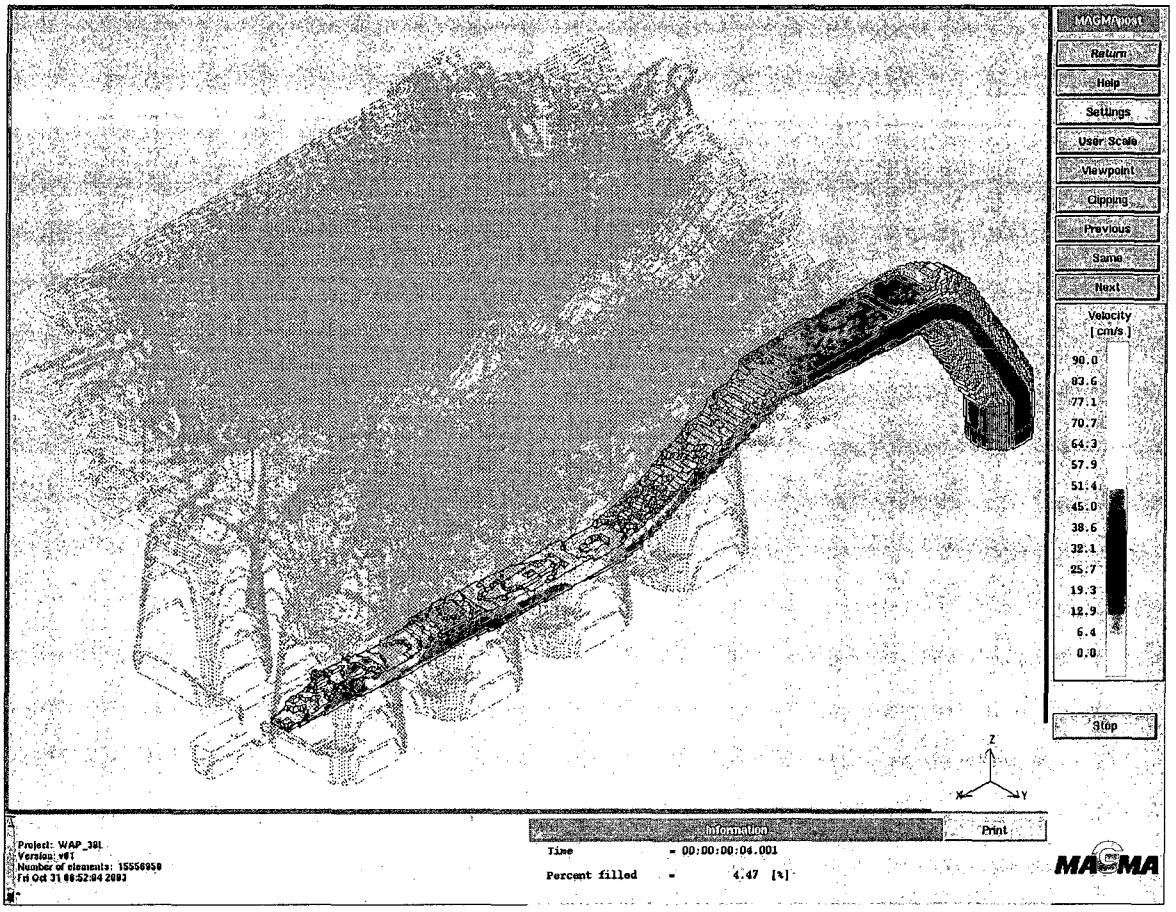

Figure 5.18: MAGMA 3.0L cylinder block fill simulation-current runner@ 4.0 seconds; IT is nearing the end of the runner. VIT remains at approx. 0.7 ms^{-1}.

Figure 5.19 is an image of the sessile runner designed for the 3.0L core package.

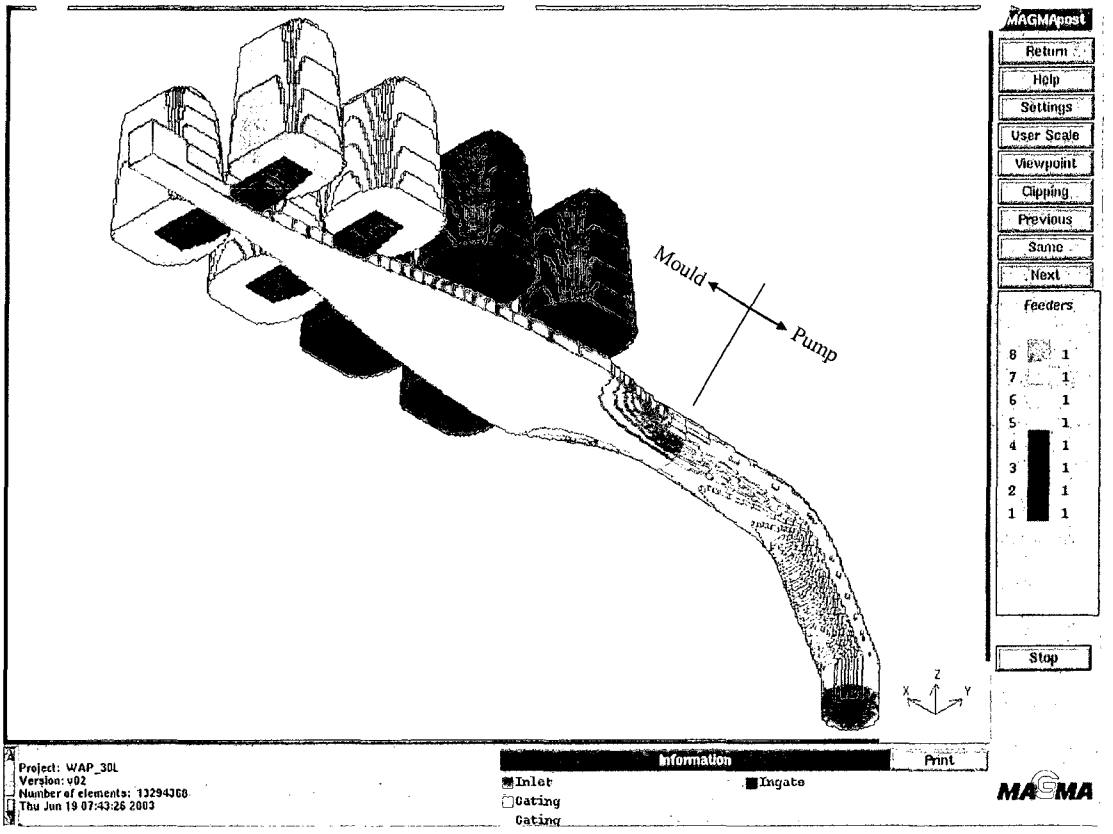

Figure 5.19: Solid Model of Sessile Runner Design (view from beneath).

Figures 5.20, 5.21 and 5.22 show the highest velocity events during fill in the Magma simulation of the sessile runner design.

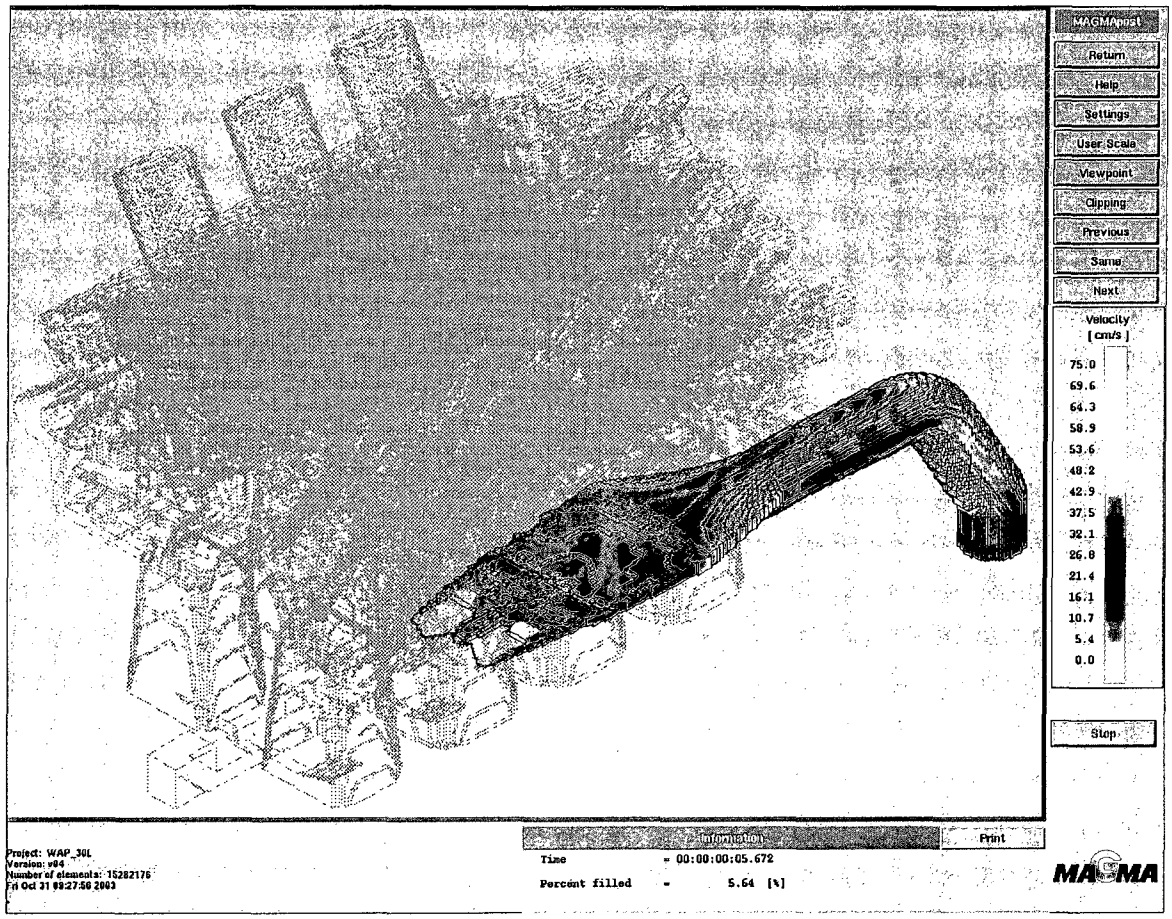

Figure 5.20: MAGMA 3.0L cylinder block fill simulation-sessile runner@ 5.7 seconds; $V_{IT} < V_{critical.}$

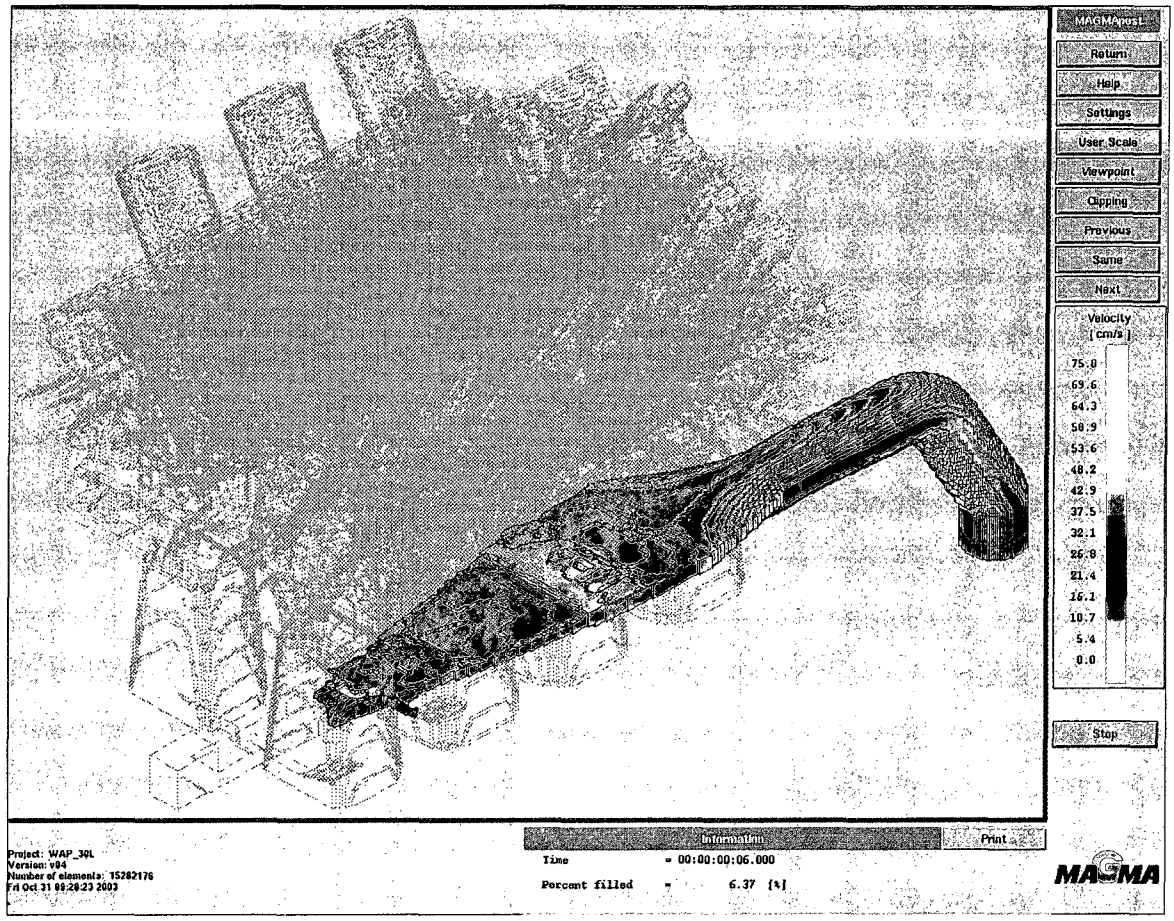

Figure 5.21: MAGMA 3.0L cylinder block fill simulation-sessile runner@ 6.0 seconds; $V_{IT} < V_{critical.}$

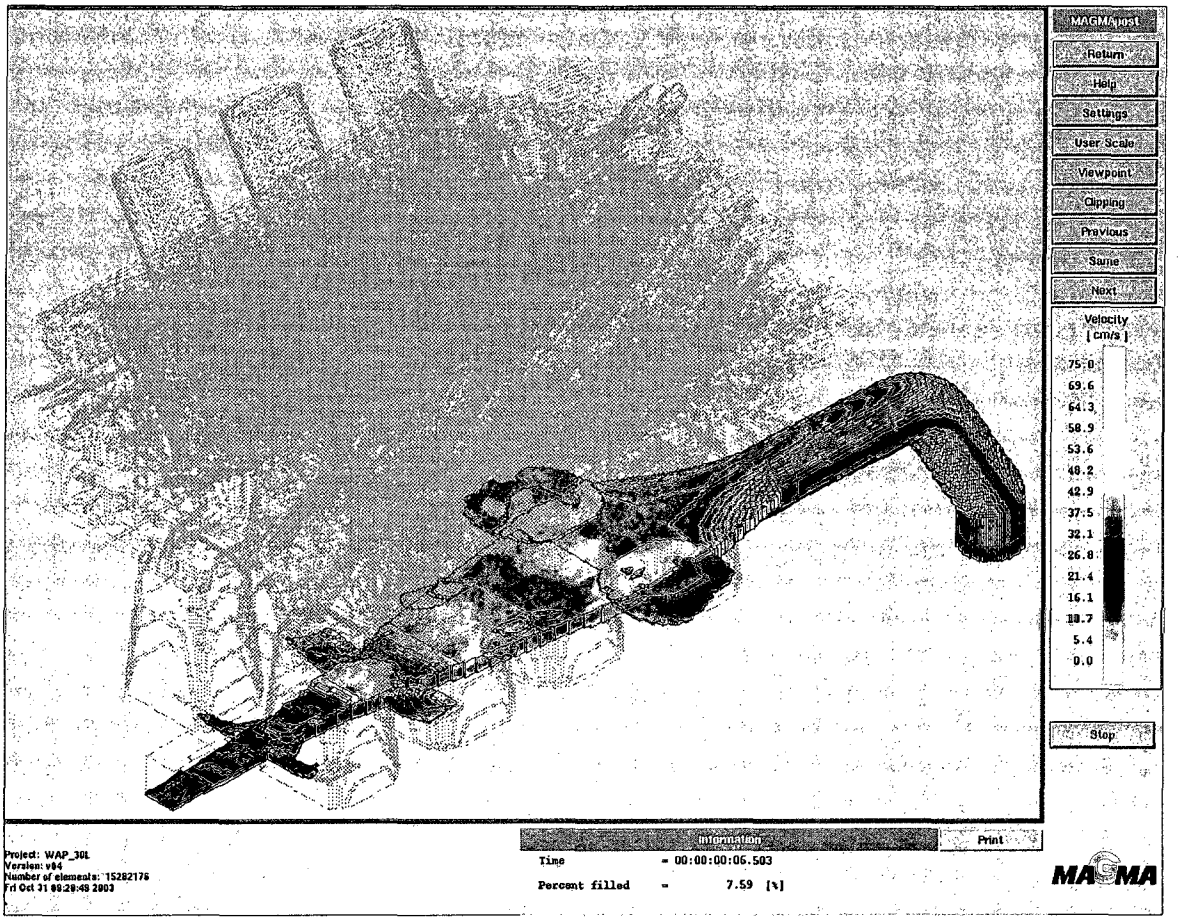

Figure 5.22: MAGMA 3.0L cylinder block fill simulation-sessile runner@ 6.5 seconds; $V_{IT} < V_{critical}$.

Chapter 6

Discussion of Results

6.1 *Initial Transient Velocity (V_{IT})*

The velocities of the initial transients produced in these experiments were purposely designed to be; a) same as production (Phase I), b) faster than production (Phase II), and c) slower than production (Phase III) initial transient velocity. The corresponding velocities down the ramp, and overall average velocities were measured and recorded for each probe along the runner's length. The instantaneous velocities were not calculable, as the necessary additional probes were not installed, nor would the sampling rate have been able to capture the data generated by such an arrangement.

Figure 5.2 shows the velocities in the timer package poured during a production casting cycle. This data set became the baseline to which all-subsequent experimental casting runs were compared. In each case, the velocity stated is the average velocity, or the distance from the probe at the start of the runner (top of the ramp) to the subject probe, divided by the time taken for the aluminum to travel between the same two probes. For the baseline (production condition), the average velocity of the initial transient running down the ramp was 0.74 ms^{-1}. Beyond this point, the average velocity remained relatively constant at approximately 0.69 ms^{-1}.

The V_{IT} generated in Phases I, II and III are graphically presented in Figures 5.3, 5.4 and 5.5. Phase I samples were poured with the resulting average velocities as seen in Figure 5.3. The tilt of the ladle achieved a pour whose average velocity in the ramp portion of the runner was 0.73 ms^{-1}, almost identical to the baseline production speed. Downstream of the ramp, the velocity of the initial transient remained relatively steady at an overall average of 0.68 ms^{-1},

very similar to the baseline case, and note that this velocity is 36% higher that $V_{critical}$ of 0.50 ms^{-1}.

Phase II velocities are shown in Figure 5.4. The average velocity down the ramp was $0.73ms^{-1}$; increasing up to 1.07 ms^{-1} by, the time the metal came to the end of the runner. Again all velocities in this phase exceeded $V_{critical}$, this time by more than 100%.

In Phase III, pours were slowed, intended to be below $V_{critical}$ as seen in Figure 5.5. The value for V_{avg} down the ramp was 0.41 ms^{-1} with the downstream V_{avg} remaining below $V_{critical}$ for the remainder of the runner fill.

Recall that the calculated predicted velocity for the initial transient at the bottom of the ramp was 0.76 ms^{-1} in section 3.3.5. This derived number matches the V_{IT} for the ramp portion of the mould for conditions in Phases I and II , but not for Phase III. The Phase III pour V_{IT} was slower than the predicted value by 46%. In reviewing the nature of the pouring process, it can be seen that the mass flow-rate of Phase I and II pours was substantially higher than that of the Phase III pour. Since the calculations for the predicted V_{IT} do not account for surface tension, it may be that in a small flow-rate situations such as in the Phase III pour, the integrity of the oxide film is being maintained because of a lack of turbulence, and is thus restraining the flow from proceeding down the ramp. If by increasing the mass of the flow inertial energy is increased, and turbulence is increased tending to damage the integrity of the film, the ability of the surface film to retard flow is reduced and is negligible in retarding the initial transient. There may be some threshold value for mass flow-rate below which the surface film can have a significant mitigating effect on V_{IT}.

As for the phase I and II pours, the fact that these V_{IT} numbers match predictions supports the theory that the bubbles found in production castings are generated in the ramp region of

the mould, since both Phase I and II ramp V_{IT} generate bubbles (as does production V_{IT}) and Phase III ramp V_{IT} does not.

6.2 Discussion of Initial Transient Velocity vs. Bubble Count

Figure 5.6 shows data relating distribution of bubble count and bubble size to the velocity of the flow. The graph indicates; a) for the current runner design, both larger bubble size, and a larger quantity of bubbles were produced as the overall average initial transient velocity increased, and b) no bubbles are produced at or below 0.43 ms^{-1} (below the Vcritical of 0.5 ms^{-1}). These two results are consistent with the literature on this subject.

It is evident from x-ray data that as V_{IT} increased, the number of bubbles generated increased. In Phase III, the relatively low V_{IT} (V_{IT}-ramp = 0.42 ms^{-1}, V_{IT}-end of runner = 0.33 ms^{-1}) produced no bubbles, whereas both the increased V_{IT} in Phases I and II (Phase I: V_{IT}-ramp = 0.73 ms^{-1}, V_{IT}-end of runner = 0.68 ms^{-1}, and Phase II V_{IT}-ramp = 0.73 ms^{-1}, V_{IT}-end of runner = 1.07 ms^{-1}) produced bubbles within the test bars.

These results are consistent with the literature citing the 0.5 ms^{-1} critical velocity requirement.

By summing the number of bubbles found in all x-rays of each respective runner velocity trial (Phase I, II and III), it can be seen in Figure 5.7 that a polynomial curve drawn through the data points intersects the abscissa at approximately 0.5 ms^{-1}, again as predicted in the literature on this subject.

6.3 Discussion of Tensile Test Results

Examination of Figures 5.8 and 6.1 show the highest average ultimate tensile strength is

consistently achieved in the Phase I samples, (i.e. those poured with initial transient velocity closest to the production condition). Samples made at the slowest initial transient velocity (Phase III) tested lower in ultimate strength compared with the Phase I and Phase II samples.

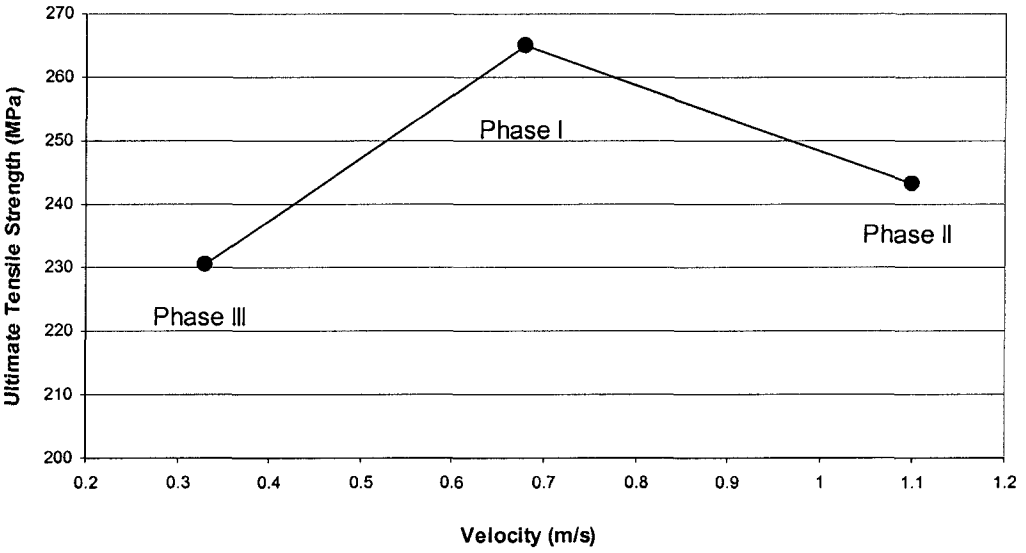

Figure 6.1: Averaged UTS data for each set of test bars (A+B) for each Phase of V_{IT}.

Though unexpected, this result is logical because the Phase I & II test bars were identically poured with the exception of the V_{IT} beyond the bottom of the ramp (i.e. the average V_{IT} down the ramp was identical, and both castings had enough head pressure to fill the mould and press the aluminum against the sand mould and the copper chill), while Phase III samples cooled differently (more slowly) and also contained no bubbles. An explanation for the low Phase III UTS may be found in that the SDAS is 23% larger (Table 6.1) than Phase I samples (and by inference, Phase II samples) because of the lower rate of cooling. The evidence for this is seen in Figure 6.2 where pictures of test bars reveal that the top corner edges of the Phase III castings did not achieve contact with the copper chill, preventing the chill from drawing heat out of the sample at the same rate that Phase I and II samples experienced. The

slow pour rate of the Phase III samples would also have resulted in a casting that filled the mould at a slightly lower temperature than Phase I or II samples. It can also be the case whereupon during solidification, the contraction of the sample away from the heat sink (copper chill plate) would have reduced the total heat flux [16] resulting in an even lower rate of cooling exacerbating the case for slower cooling rate. The phenomenon is noted, but not considered important here, as the focus of this experiment is bubbles, not solidification structure.

Table 6.1: SDAS comparison (Phase II vs. Phase III)

SDAS Measurement Comparison Phases II vs. III (μm) (Sample size = 1)						
Location	1 Top of sample (against Cu)	2	3	4	5 Bottom of sample (against sand)	Average
Average II - Average III	3.45	4.3	1.8	4.3	6.3	**4.03**
% Difference	25.7%	27.9%	9.4%	21.0%	32.1%	**22.9%**

It was thought that sample A data may behave differently than sample B data since the sample A test bar is located further away from the leading portion of the initial transient for all Phases I, II and III. To examine this possibility, the Anderson-Darling normality test was performed (using pooled standard deviation due to unequal sample sizes) to determine normality of each UTS data set followed by a test for equal variances, followed by the Mood Median Test. Results are found in Tables 6.2 through 6.5.

Since the UTS populations were not distributed normally, before testing for population equality the variance required comparison as per Tables 6.3 and 6.4.

Since the P-Value for Levene's test was above 0.05 for all tests, the null hypothesis must be rejected, that is, the variance of each compared population was the same. Once this was established, the UTS populations were compared using the Mood Median Test (Mood's

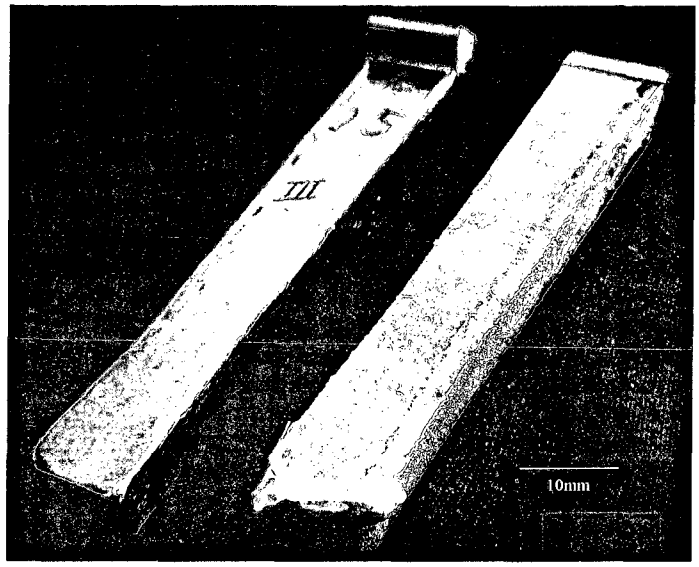

Figure 6.2: Picture of two test bars after being cut from the runner casting. Left: Picture of a Phase III test bar revealing incomplete contact with the copper chill at the edges of the casting (rounded edges). Right: Phase I test bar with sharp edges and even a small amount of flash due to overpressure achieved in the mould cavity upon reaching full condition.

Table 6.2: Test for normal distribution.

Test for Normality of Distribution (UTS Data).			
Tensile Sample	**Phase I**	**Phase II**	**Phase III**
A Data	Normal	Not Normal	Not Normal
B Data	Not Normal	Not Normal	Normal
A+B Data Combined	Normal	Not Normal	Not Normal

Table 6.3: Results of Levene's Test for Equal Variance between A & B samples within Phases.

P-Value of Levene's Test for Equal Variance				
		Tensile Samples		
		Phase I B	**Phase II B**	**Phase III B**
Tensile Samples	**Phase I A**	0.961		
	Phase II A		0.599	
	Phase III A			0.515

Median Test accommodates data whose distribution is non-normal with equal variance of

Table 6.4: Results of Levene's Test for Equal Variance across Phases.

P-Value of Levene's Test for Equal Variance				
		Phases Being Compared		
		I vs. II	II vs. III	I vs. III
Tensile Samples	A	0.207	0.123	0.508
	B	0.498	0.468	0.944
	A+B	0.938	0.580	0.370

compared populations). The population means could not be compared due to the non-normality of the distribution of UTS values. Results of the Mood Median test are found in Table 6.5. Although not strictly applicable, 2 Sample T-Test was applied to the same data to compare the population means as a rough correlation check (the 2 Sample T-Test prefers normally distributed data for most reliable results).

The criteria for determining if a difference exists lies in the P-Value of the Mood's test. If this value lies below 0.05, then there is a difference in the median values of the two populations being compared, by the amount given in the confidence interval.

Examining the comparisons between UTS of tensile specimen A vs. B, there exists a slight to mild difference in the Phase I and II test data and a slightly larger difference in the Phase III data.

Examining the comparisons between UTS of tensile specimens A across Phases, and then B across Phases, the same trend is seen, that is, there is a larger difference between Phase I or II and Phase III data than between Phase I and II data.

Again examining the comparisons between pooled A+B tensile bar UTS data across Phases, it can be seen that the greatest difference in strength is between Phase II samples and the rest.

Table 6.5: Results of Mood's Median Test, and 2 sample T-Test.

Compared Populations Phase/Tensile Specimen	Mood Median Test				2 Sample T-Test					
	P-Value	95% Confidence Interval (MPa)	Result	Comment	T-Value	P-Value	95% Confidence Interval (MPa)	Estimate for Difference (MPa)	Result	Comment
I A vs. I B	0.020	2.8, 18.0	Different	Mild Difference	2.08	0.048	.08, 18.5	9.3	Different	Slight Difference
II A vs. II B	0.068	2.3, 22.9	Same	No Difference	1.35	0.187	6.3, 30.8	12.3	Same	No difference
III A vs. III B	0.000	10.6, 22.2	Different	Mild Difference	4.77	0.000	10.5, 26.3	18.4	Different	Mild Difference
I A vs. II A	0.001	3.5, 28.0	Different	Mild Difference	2.89	0.007	6.5, 38.6	22.6	Different	Different
I A vs. III A	0.000	32.4, 47.2	Different	Strong Difference	11.41	0.000	31.5, 45.3	38.4	Different	Strong difference
II A vs. III A	0.000	13.5, 34.6	Different	Different	2.13	0.042	0.6, 31.0	15.8	Different	Slight Difference
I B vs. II B	0.000	8.6, 23.7	Different	Mild Difference	2.80	0.010	5.2, 34.1	19.6	Different	Different
I B vs. III B	0.000	25.1, 42.5	Different	Strong Difference	5.85	0.000	19.0, 39.6	29.3	Different	Strong difference
II B vs. III B	0.001	10.1, 25.7	Different	Mild Difference	1.58	0.125	2.8, 22.2	9.7	Same	No Difference
I (A+B) vs. II (A+B)	0.001	4.2, 17.8	Different	Mild Difference	3.05	0.004	4.4, 21.3	12.8	Different	Different
I (A+B) vs. III (A+B)	0.000	27.1, 44.4	Different	Strong Difference	9.44	0.000	26.1, 40.2	33.1	Different	Strong difference
II (A+B) vs. III (A+B)	0.000	17.4, 31.8	Different	Strong Difference	4.75	0.000	11.7, 28.9	20.3	Different	Strong difference

There are two trends seen in the data: 1) There is only a marginal difference in UTS populations between tensile samples A and B (in any Phase), and 2) The difference in the average UTS values as presented in Figure 5.8 are only marginally true as far as median testing can substantiate, due to the large variation and small sample size of the UTS data collected.

Based on these results, the hypothesis that UTS is an accurate predictor/descriptor of the velocity at which the initial transient traveled to fill the mould must be rejected.

One method of adding robustness to the tensile testing procedure would be to increase the diameter of the tensile bar to increase possibility of the bar containing a defect, and/or use cycle fatigue tests that is more sensitive to the presence of pores.

6.4 Weibull Modulus vs. Velocity A & B Tensile Specimens

The Weibull Moduli were plotted for each set of UTS values for test bars A and B. Figure 6.3 is a plot of the Weibull Modulus data found in Table 6.6, and it shows how the Weibull modulus varies with the velocity of the initial transient down the runner. Phase III data for test bar B (lowest velocity, and the tensile bar location is closest to the end of the runner per Figure 4.15) yields the highest Weibull modulus. This indicates that the tensile strength of the B samples reflected the low probability of defects occurring within the sample structure (i.e. homogeneous nature of the cast section -no bubbles and less oxide inclusions). This is graphically illustrated in Figure 6.4.

The same trend is seen in the A Sample data illustrated in Figure 6.5, however to a lesser extent. The Weibull modulus for the Phase II A samples is actually larger than the Phase I A samples in this same Figure, and can only be explained by the random placement of bubbles and oxides within the structure of the samples cast at velocities higher than 0.5 ms^{-1}.

As expected, the Weibull modulus for each of the Phase III samples was highest, however the modulus for the Phase II results was higher than the Phase I samples which does not follow logic since the higher velocity Phase II pours resulted in more entrained bubbles. More entrained bubbles set the stage for inconsistent sample properties, so the expected Weibull modulus was that of a low value (shallow slope). This is not the case for either A samples, nor B samples. Due to the inability of the Weibull moduli to coincide with bubble count data, the hypothesis must be rejected, that is, the Weibull modulus has not been found to be a good descriptor of bubble count within the parameters of testing involved herein.

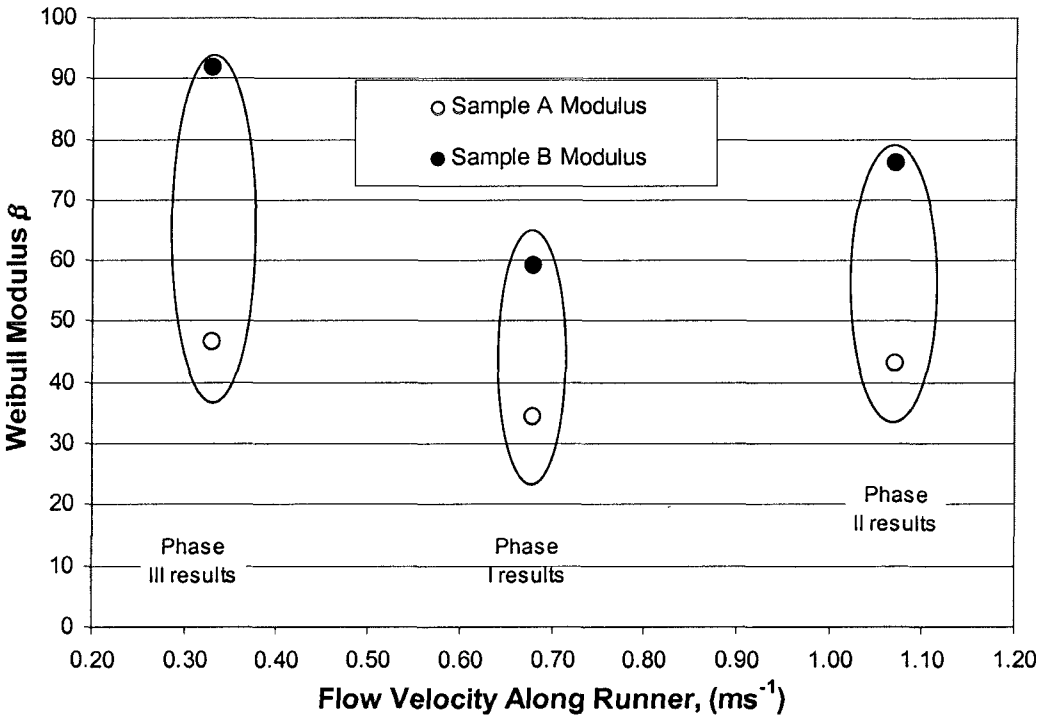

Figure 6.3: Weibull modulus of UTS as a function of velocity of initial transient.

Table 6.6: Weibull modulus of UTS as a function of velocity of initial transient.

Table of Weibull Modulus (λ) Results				
	Condition	Overall Average Runner Velocity (ms^{-1})	Sample A Modulus	Sample B Modulus
UTS	Phase I	0.68	34.40	59.20
	Phase II	1.07	43.10	76.20
	Phase III	0.33	46.70	91.70

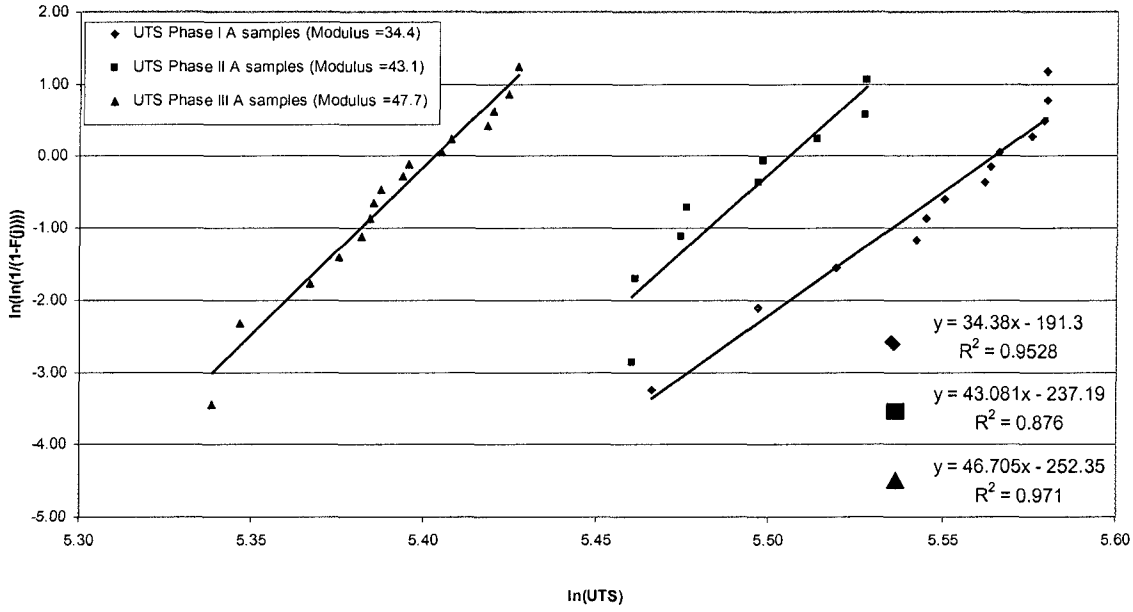

Figure 6.4: Plot of ln(UTS) vs. Weibull density function for A sample data only.

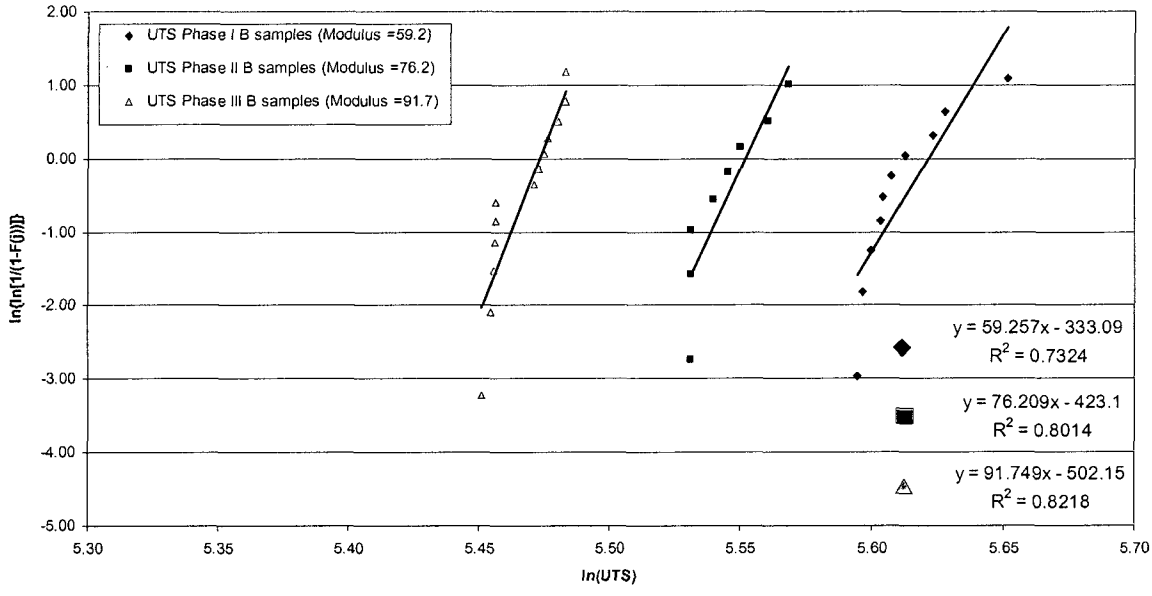

Figure 6.5: Plot of ln(UTS) vs. Weibull density function for B sample data only.

6.5 Simulation Results Discussion

The magma fill simulation for the baseline condition yielded V_{IT} (for the ramp portion of the mould) of between 0.6 ms^{-1} and 0.9 ms^{-1}, values matching what was actually found during baseline (0.74 ms^{-1}), Phase I (0.74 ms^{-1}) and Phase II (0.74 ms^{-1}) experiments. This success validates the Magma model's ability to predict the flow velocity in this application, and thus lends validity to results obtained for the sessile runner velocity prediction. The maximum runner velocity simulated for the sessile runner was between 0.40 ms^{-1} and 0.50 ms^{-1} which satisfies the $V_{critical}$ requirement, and thus will not form a flow entrained with air bubbles as is reinforced in Figures 5.20, 5.21 and 5.22.

Simulation Software MAGMAsoft version 4.2 software equipped with the Cosworth Module (a special module developed by MAGMA GmbH., Aachen, Germany for the Ford Motor Company) was used to simulate the complete filling of the mould in the current design. Before the start of this research project, the author collaborated with a team of simulation experts from the Ford Motor Company Casting Division to work on "calibrating" the mould filling simulation for the 3.0L casting at WAP. This calibration consisted of defining the input to the simulation model in terms of a series of pump curves, which in turn defined the mass flow rate into the mould package at any given level of fill. The timer package described in Chapter 4 was used for this purpose, combined with a map of the area within the casting cavity at any given height above the bottom of the runner. In this way, the cumulative volume of metal and the time it took to fill that volume was known in absolute terms, so that a mass flow-rate could be plotted for the entire filling sequence. The results were incorporated into what MAGMA has named the "Cosworth Module", and have resulted in a more accurate modeling of the Cosworth Process of production mould fill.

Of interest for this simulation was the velocity of the initial transient down the runner.

6.5.1 Current Runner Design Fill Simulation

Figures 5.16, 5.17 and 5.18 show a series of snapshots during the current runner design fill section of the simulation, where the velocity of the initial transient (VIT) is between 0.6 ms^{-1} and 0.9 ms^{-1}. Note that the 0.76 ms^{-1} prediction of VIT at the bottom of the ramp section of the runner in section 3.3.5, and the 0.74 ms^{-1} as measured at the bottom of the ramp in the baseline, Phase I and II data are within 2.7% of each other.

6.5.2 Sessile Runner Design Fill Simulation

In developing a sessile runner, the rules of design, developed over generations by casting engineers, were followed with the addition of one; that the distance from the floor of the runner to the ceiling was to be the same as the sessile height of 12.5 mm. All other shapes/dimensions were guided by the traditional runner/gating system knowledge base gathered over time in this industry [52, 53].

The criterion set forth for the sessile design were as follows:

The sessile runner was to have no detrimental affect on the quality of the casting (shrink, porosity, gas). The time required to fill the mould was to be approximately the same as currently in production (18-22 seconds). VIT must be equal to or below Vcritical (0.5 ms^{-1}) during not only runner fill, but during the entire casting cavity fill sequence.

The result in design is seen in Figure 5.19, where the runner is shown from the left bottom/side view. Figures 5.20 through 5.22 show the runner velocities below or near the critical value of 0.5 ms^{-1}, yet facilitate a full casting in only slightly longer time than the

current model. According to the MAGMA solidification prediction using this design, the runner facilitates flow into the casting cavity that meet the criteria outlined above, and the software predicts not only that the casting has no areas of concern regarding shrink or porosity. This result has yet to be seen in a casting, but the groundwork has been laid. The software as mentioned cannot predict the generation of bubbles earlier, but V_{IT} remains below $V_{critical}$, which is the first step in controlling bubble generation and entrainment.

6.6 Discussion of Experimental Setup

The experimental setup used to produce results for this thesis was successful, though leaves room for improvement. A number of changes must be made to this methodology to yield a more accurate exploration of this topic. These improvements are described below:

1) The method of getting aluminum into the runner. The use of gravity necessitates a free fall of some distance before the aluminum contacts the mould and starts its progression along the runner. Although this distance was painstakingly kept to an absolute minimum, there was, nevertheless a fall involved. The results for all three phases of the experiment were all influenced to the same degree by this fall, which mitigates the effect relatively speaking, however it is the absolute presence or absence of bubbles which were being measured and which determine an acceptable casting vs. a scrap casting.

2) The data recorder used to capture times of aluminum flow contact with the probes was only capable of a 100 millisecond sampling rate (0.1 s) which is an order of magnitude too slow. More accurate velocity results must be obtained in order to more precisely characterize the flow. Due to this relatively slow sampling rate, the velocity pin to pin was not accurately represented. More useful was the average velocity of the flow measured over the entire

length of the runner, measured over a longer period of time thus increasing the accuracy of measurement.

3) The experiment was performed for three different average velocities (Phases I, II & III). This produced results for bubble counts that successfully fit all literature reviewed, however a higher degree of confidence and clarity would have been achieved with five or more different phases of testing.

4) The velocity of the baseline package poured in production was not accurately reproduced using the robot/ladle pouring procedure for Phase I. Although the same average velocity was achieved down the ramp portion of the mould, beyond this the velocity could not be matched. Although this result was not optimal, the difference in velocities between each of the phases was comparable and did result in the predicted outcome.

6.7 Discussion of Hypothesis

The hypothesis put forward earlier in this work was that the runner was responsible for generating and entraining air bubbles which then would go on to become frozen within the casting. Experimentation has provided objective evidence that as the velocity down the runner increases, bubble quantity and size increase. Also, as the velocity is reduced, in fact to below 0.5 ms^{-1}, the generation of bubbles stops. One solution to head deck porosity, then, would be to reduce the velocity of the initial transient during the filling of a production casting. This solution, though simple but expensive to implement, would result in a relatively low temperature initial transient which may lead to cold-shut defects within the casting or poor lay-up or knitting of liquid fronts around the cast iron cylinder bore liners in

the outboard areas of the casting. This statement is supported by the fact that the test bars poured at the slower velocity did not completely fill the corners of the mould.

The solution, then, falls to a runner design that not only facilitates high volume flow but initial transient velocities that are below $V_{critical}$, i.e. the sessile runner.

Chapter 7

Summary and Conclusions

As a result of this study of generation and entrainment of bubbles during various initial transient velocities, 3 conclusions are arrived at.

- Using X-ray sampling, bubble counting was found to be a good descriptor of quantifying the characteristics of initial transient velocity. This is due to the correlation obtained between theoretical value and the frequency of bubbles found. Also, the fact that bubbles are not present below the $V_{critical}$ value, and bubbles were present above this value (per figure 5.7) supports this conclusion.

- The UTS of test bars was not an adequate descriptor of the number or size of bubbles contained within the test bar castings.

- In order to eliminate the runner as a source of bubbles within the studied casting, one has only to ensure that the initial transient velocity remains below 0.5 ms^{-1} during the filling of the runner.

- An initial transient velocity of 0.5 ms^{-1} or below is not possible with the current runner design, as the 19° downgrade ramp at the entrance of the runner induces higher velocity than requested by the fill program. The liquid metal, introduced with the necessary mass flow rate to fill the casting with the required speed, would flow down the existing ramp at a minimum speed of 0.56 ms^{-1}. Add to this an in-rush velocity of even 0.20 ms^{-1} (a realistic value based on experience), and the velocity at the bottom of the ramp becomes 0.76 ms^{-1} and higher –a condition prone to generate bubbles. Recall that the calculated predicted velocity for the initial transient at the bottom of the ramp was 0.76 ms^{-1}, this number matches the V_{IT} for the ramp portion of the mould for each of the test conditions

that would be used to fill a production casting; that is, with enough flow rate that cold-shut will not occur in the runner. The fact that these numbers match supports the conjecture that the bubbles found in production castings are indeed being generated in the ramp region of the mould, since both Phase I and II ramp V_{IT} generate bubbles (as does production V_{IT}) and Phase III ramp V_{IT} does not.

- A sessile runner design will, according to simulation technology, yield the same flow rate but with the initial transient velocity at or below the critical value of 0.5 ms^{-1}.

In summary, objective evidence has been generated that supports the hypothesis that the current 3.0L cylinder block mould runner design is flawed in that it is facilitating the entrainment of air into the lead metal, or initial transient. Adoption of the sessile runner is shown via simulation to reduce the velocity of the initial transient to below 0.5 ms^{-1}. The data indicates that no bubbles would be generated during the runner fill event, in which case there would be no bubbles to come to rest and solidify at or under the rear / head deck area of the casting thus eliminating, or at least reducing the defect known as "Head Deck Porosity".

Chapter 8

Recommendations

The following points outline the recommended actions that will further the current work:

- Pending successful trials with this design, it is the recommendation of the author that the sessile runner design be adopted for use in all future casting programs at Nemak, and indeed for any low pressure filled mould within the casting industry
- A repeat of the test bar castings using the sessile runner is necessary. The theory and simulations all agree that the runner will yield favourable results in reducing or eliminating entrained bubbles, and evidence is needed to support/refute this.
- Further testing with a flat, non-sessile runner filled at different velocities (as opposed to the more complex runner shape used within this study) will add fundamental understanding to the propensity of a flow to include air bubbles.
- The study of ingate velocity (from runner into risers) versus bubble entrainment would serve to complement the current study.
- The study of temperature loss in different runner designs, especially sessile, is a critical body of knowledge that needs development.
- Lastly, it is recommended that the ability of the surface film to impede flow be studied not only for a large section modulus runner shape, but most especially for the 4.0 to 4.5mm thick cavity chambers all throughout a typical aluminum cylinder block casting. There are defects whose origins lie in the interrupted flow of aluminum during mould-fill [16], and the relationship between the film's ability to inhibit flow and the defect will advance the science of casting-making for the benefit of all.

References

1. Byczynski, G.E., *The Strength and Fatigue Performance of 319 Aluminum Alloy Castings*, in *Faculty of Engineering*. June 2002, University of Birmingham: Birmingham England, U.K.

2. Byczynski, G.E., *Quantification of Solidification Characteristics of Al-Si Alloys by Thermal Analysis*, in *Mechanical and Materials Engineering*. 1997, University of Windsor: Windsor Ontario, Canada.

3. Sokolowski, J. and W. Yang, *Insoluble AlTi(Si) Crystals Present in the Pechiney Ingot and in the 356 WAP Cylinder Heads*. 1996, University of Windsor: Windsor, Ontario, Canada. p. 8.

4. Francis, R., *Quality Control and Improvement of Aluminum Alloy Castings for the Next Generation of Engine Block Cast Components.*, in *Dept. of Mechanical and Materials Engineering*. April 22, 2005, University of Windsor: Windsor, Ontario, Canada.

5. Djurdjevic, M., et al., *Evaluation of Strontium Fading in the 319 Aluminum Alloy Using Thermal Analysis.* AFS Transactions, 2000. **20**: p. 485-489.

6. Sokolowski, J., et al., *Electromagnetic Pump Clogging in a Foundry Producing 319 Aluminum Alloy Automotive Castings: Causes and Solutions.* AFS Transactions, 2000. **22**: p. 497-503.

7. Djurdjevic, M., Sokolowski, J.H., and Hasenbusch, R., *Assessment of the Hydrogen Level in 319 Alloy Melts Using the Thermal Analysis Technique.* Light Metals, 131st TMS Annual Meeting, Seattle, Washington, USA, 2002: p. 889-896.

8. MacKay, R., et al. *Using the Method of an In-situ Thermal Analysis Array in a Cast Section of an Engine Block Casting to Diagnose the Cause of Shrinkage Porosity.* in *131st TMS Annual Meeting, Seattle, Washington, USA*. 2002. Seattle Washington, U.S.A.

9. Francis, R. and J.H. Sokolowski, *Effect of Fe and Mn on the Shrink porosity in 3.0L Engine Blocks*. 2004, University of Windsor: Windsor Ontario, Canada.

10. Kasprzak, W. and J. Sokolowski, *Determination of Type of Porosity In the Sample Taken from the Bulkhead Region of the WAP Engine Block*. 2001, University of Windsor: Windsor Ontario, Canada. p. 8.

11. Kierkus, J. and J. Sokolowski, *Strontium-chloride Pump Clogging Work.* 1998, University of Windsor: Windsor.

12. Isawa, T. and J. Campbell, *Initial Filling Transient of the Running System.* Trans. Japan Foundrymen's Soc., 1994. **13**: p. 38-49.

13. Sulaiman, S. and Keen, T.C., *Flow Analysis Along the Runner and Gating System of a Casting Process.* Journal of Materials Processing Technology, 1997. **63**: p. 690-695.

14. Jorstad, J.L. and W. Rasmussen, *Aluminum Casting Technology.* 2nd ed, ed. A. Donna L. Zalensas. 1993, Des Paines, Illinois USA: American Foundry Society. 356.

15. Campbell, J., *Castings Practice The 10 Rules of Castings.* 1 ed. 2004, Oxford, England: Elsevier Butterworth-Heinemann. 205.

16. Campbell, J., *Castings.* 1991, Oxford: Butterworth-Heinemann.

17. Champan, C., *Practical Tips on Gating Iron Castings*, in *Modern Casting.* 2005. p. 28-30.

18. Thiele, W., *Aluminum.* Vol. 38. 1962.

19. Drouzy, M. and Mascre, C., Metallurgical Reviews, 1969. **14**: p. 25-46.

20. Divandari, M. and J. Campbell, *A New Technique for the Study of Aluminum Oxide Films.* Aluminium Transactions, 2000. **2**(2): p. 233-238.

21. Nyahumwa, C., Green, N.R. and J. Campbell, *Effect of Mold-Filling Turbulence on Fatigue Properties of Cast Aluminum Alloys (98-58).* AFS Transactions, 1998(106): p. 215-224.

22. Dignam, M.J., *Oxide films on Aluminum.* Journal of the Electrochemical Society, 1962. **109**(3): p. 184-198.

23. Huang, L.W., Shu, W.J. and Shih, T.S., *Diagnonsis and Analysis of Oxide film in Al-Si-Mg Alloys.* AFS Transactions, 2003. **00-40**: p. 547-560.

24. Silva, M.P. and Talbot, D.E.J., *Oxidation of Liquid Aluminum - Magnesium Alloys.* Light Metals, edited by P.G. Campbell (The Minerals, Metals & Materials Society), 1989: p. 1035-1040.

25. Impey, S.A., Stephenson, D.J. and Nicholls, J.R., *Mechanism of Scale Growth on Liquid Aluminium.* Materials Science and Technology, 1988. **4**(December): p. 1126-1132.

26. Wightman, G. and D.J. Fray, *The Dynamic Oxidation of Aluminum and its Alloys.* Metallurgical Transactions B, 1983. **14B**(December): p. 625-631.

27. Halvaee, A. and Campbell, J., *Critical Mold Entry Velocity for Aluminum Bronze Castings.* AFS Transactions, 1997. **97-18**: p. 35-46.

28. Runyoro, J., Boutorabi, S. and Campbell, J., *Critical Gate Velocity for Film-Forming Casting Alloys: A Basic for Process Specification.* AFS Transactions, 1997. **100**: p. 225-234.

29. Martindale, D.G., et al., *Fundamentals of Physics: An Introductory Course.* 1987: D.C. Heath Canada Ltd.

30. Campbell, J. *The origin of porosity in castings.* in *Asian foundry congress.* 1996: Upper Mount Gravatt.

31. Fox, S. and J. Campbell, *Visualization of Oxide Film Defects During Solidification of Aluminium Alloys.* Scripta Materialia, 2000. **43**(10): p. 881-886.

32. Fuoco, R. and Correa, E.R., *The Effect of Gating System Design in the Quality of Alumunum Gravity Castings.* p. 1-30.

33. Rezvani, M., X. Yang, and J. Campbell. *The Effect of Ingate Design on the Strength & Reliability of Al Castings.* in *AFS Cast Expo '99.* 1999. St. Louis, Missouri: AFS inc.

34. Campbell, J. *The Entrainment Defect: The New Metallurgy.* in *ASM International Aluminum Casting Technology Symposium.* 2001. Ohio.

35. Miller, I. and J. Freund, *Probability and Statistics for Engineers.* Prentice-Hall Mathematics Series, ed. D.A.A. Bennett. 1965, Englewood Cliffs, N.J.: Prentice-Hall. 432.

36. Dodson, B., *Weibull analysis.* 1962, Milwaukee, Wi: A.S.Q.C. Quality Press.

37. Green, N.R. and J. Campbell, *Influence of Oxide Film Filling Defects on the Strength of Al-7Si-Mg Alloy Castings.* AFS Transactions, 1994(102): p. 341-348.

38. Baldini, Nichole, et. al., N.C.B. ed. *ASTM Standard Designation E 155 Standard Reference Radiographs for Inspection of Aluminum and Magnesium Castings.* Annual Book of ASTM Standards 2001, ed. R.F.B. Allen, Nicole C.; Gutman, Elizabeth L. Vol. 03.01. 2001, ASTM: West Conshohocken, Pa., USA.

39. Baldini, Nicole C., et. al., N.B., ed. *ASTM Standard Designation: E-94 Standard Guide for Radiographic Examination.* Annual Book of ASTM Standards 2001, ed. G. Baldini, Keefe, Leinweber, Mayer, McGee, Peters Whealen, Wilhelm. Vol. 03.03. 2001, ASTM: Conshohocken, PA. 1-12.

40. Sirrell, B. and Campbell, J., *Mechanism of Filtration in Reduction of Casting Defects Due to Surface Turbulence During Mold Filling.* AFS Transactions, 1997. **97-11**(105): p. 645-654.

41. Divandari, M. and Campbell, J., *The mechanism of bubble damage in castings.* in *1st international Conference on Gating, Filling and Feeding of Aluminum Castings.* 1999. Nashville, Tennessee: AFS.

42. EKK Inc., *Software and Consulting Services for the Metal Casting Industry.* 2004: Chicago Ill. USA 2004 AFS Casting Congress.

43. Finite Solutions Inc, *FLOW CAST - Flow Modeling for Mold Filling using Computational Fluid Dynamics.* 2004: Chicago, Ill. USA 2004 AFS Casting Congress.

44. Magmasoft, 2005.

45. Roy, N., Louchez, P.R., and Samuel, F.H., *Statistical analysis of porosity in Al-9wt%Si-3wt%Cu-X alloys systems.* Journal of Material Science, 1996. **31**: p. 4725-4740.

46. Burford, J.C., *Conversations with Flow3D, and Magma Representatives at Cast Expo 2004.* 2004: St. Louis Missouri.

47. Burford, J.C., *Personal Communication with B. Brosnan, K. Bonds, J. Keep, J. Counihan.* 1990-1992: Dearborn, Michigan U.S.A.

48. Mitrasinovic, A., Development of Thermal Analysis and Analytical Techniques for the Assessment of Porosity and Metallurgical Characteristics in 3XX Aluminum Alloys, in Engineering Materials. 2004, University of Windsor: Windsor. p. 130.

49. Rasmussen, W. and E. Eckert. *RPT Gauges Aluminum Porosity.* in *AFS Casting Congress.* 1991. Birmingham, Alabama: AFS.

50. Gruzleski, J.E. and B.M. Closset, *The treatment of liquid aluminum-silicon alloys.* 1990, Des Plaines, Ill.: American Foundrymen's Society. xiii, 256.

51. Baldini, Nicole C., et. al., R.F.A., ed. *ASTM Standard Designation E 8-00 Standard Test Methods for Tension Testing of Metallic Materials.* Annual Book of ASTM Standards, ed. R.F.B. Allen, Nicole C, ;Gutman, Elizabeth L. Vol. 03.01. 2001, ASTM: Baltimore Maryland. 56-76.

52. AFS, *Basic Principles of Gating*. Cast Metals Technology Series. 2000, Des Plaines, Illinois 60016-8399: American Foundrymen's Society Inc. 66.

53. Suschil, A.L. and L.A. Plutshack, *ASM Handbook, Casting*, In-*Gating Design*, L.A. Abel, et al., Editors. 1998, ASM International. p. 937

Appendix A
Early Work Results

Table A1: Results of Run #217 Mega Gas Generation Experiment.

Run # 217 "Mega Gas Generation" experiment
X-Ray Analysis Sheet

* = Left hand side upper 1/2 of liner

April 4/30/99

\+ = Sand present @ head deck

				Section 1			Section 2			Section 3			Section 4			Section 5			Section 6			Section 7			Section 8			Section 9			Section 10						Section 11			
Severity Ranking	Cast order	Debris	Casting ID	P1	P2	G1	P1	P2	G1	P1	P2	G1	P1	P2	G1	P1	P2	G1	P1	P2	G1	P1	P2	G1	P1	P2	G1	P1	P2	G1	P1	P2	G1	G2	G6	CB	P1	P2	G1	S
1	6	Spray	859045	2			2			2			3	1		2			2			3	1		2			2			2			13	*			3			
1	11	Spray	860170	2			2			2			4	1		2			2			4			2			2			3			12	*			3			
			AVG	2	0	0	2	0	0	2	0	0	3.5	1	0	2	0	0	2	0	0	3.5	0.5	0	2	0	0	2	0	0	2.5	0	13		0	0	0	3	0	0	0
2	4	Oxides	859047	2			2			2			4	3	1	2			2			3	1		2			2			3		8	*			2	3			
2	10	Oxides	860171	2			2			2			4			2			2			4			2			2			2		10	*		G6		2			
			AVG	2	0	0	2	0	0	2	0	0	4	1.5	0.5	2	0	0	2	0	0	3.5	0.5	0	2	0	0	2	0	0	2.5	0	9		0	0	1	2.5	0	0	0
3	3	Sand	859048	1			2			2			4	2		2			2			4			2			2			3		6	*+				3			
3	9	Sand	859060	2			2			2			4			2			2			4			2			2			3		10	*	1			1		4	
			AVG	1.5	0	0	2	0	0	2	0	0	4	1	0	2	0	0	2	0	0	4	0	0	2	0	0	2	0	0	3	0	8		0.5	0	0	2	0	2	0
4	2	Chips	860167	2			2			2			4	1		2			2			4			2			2			1*		9	*				3			
4	7	Chips	860168	2			2			2			4			2			2			5	1		2			2			3		2	+	1			3			
			AVG	2	0	0	2	0	0	2	0	0	4	0.5	0	2	0	0	2	0	0	4.5	0.5	0	2	0	0	2	0	0	1.5	0	5.5		0.5	0	0	3	0	0	0
5	5	Wet Boron	859046	2			2			2			4			2			2			4	2		2			2			3		6	*				2			
5	8	Wet Boron	860169	2			1			1			2			1			1			1	2		1			1			2*	2	4	*				1	3		1
			AVG	2	0	0	1.5	0	0	1.5	0	0	3	0	0	1.5	0	0	1.5	0	0	2.5	2	0	1.5	0	0	1.5	0	0	1.5	1	5		0	0	0	1.5	1.5	0	0.5
6	12	Control	859059	2		1	2			2			4			2			2			4			2			2			3		2					2			
3	1	1st casting	860166	2		1	2			2			4			2			2			5			2			2			3	1	8	*	2	G3		2		1	1

Appendix B
Runner Velocity Measurements

Baseline (Production) Runner Velocity (Vavg.=0.7 ms-1)

Connector No	Dist between probes (m)	Dist to probe from 0 (m)	Time made	Time between probes (s)	Cumulative time to probe (s)	Velocity between probes (ms-1)	Average Velocity to Probe (ms-1)
PL-0	0.000	0.000	2.30	0.00	0.00	0.00	0.00
PL-1	0.148	0.148	2.50	0.20	0.20	0.738	0.74
PL-2	0.114	0.262	2.70	0.40	0.40	0.286	0.65
PL-3	0.106	0.368	2.80	0.50	0.50	0.213	0.74
PL-4	0.138	0.507	3.00	0.70	0.70	0.198	0.72
PL-5	0.045	0.551	3.10	0.80	0.80	0.056	0.69

Vavg = 0.7 ms^{-1}

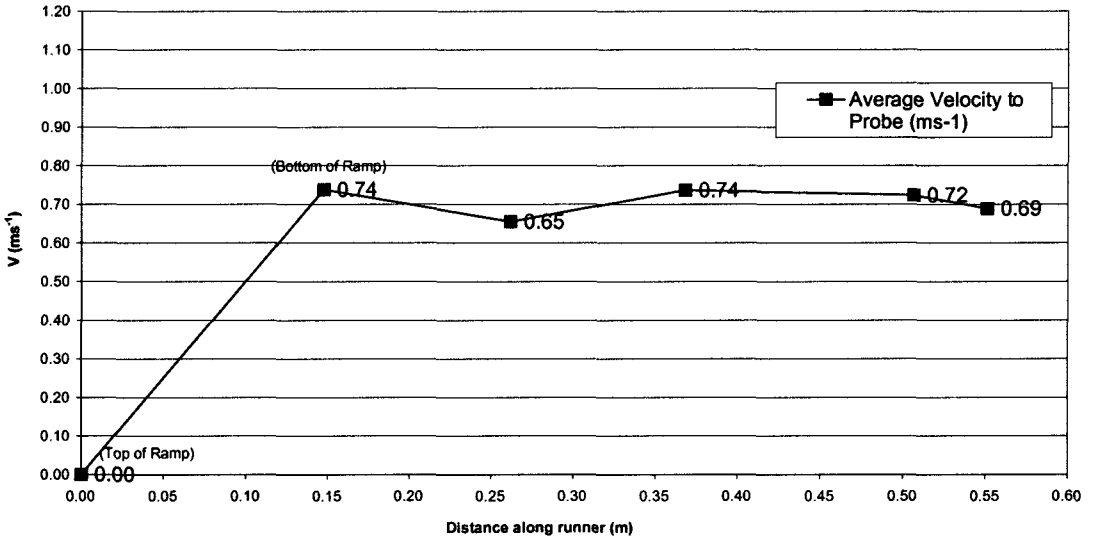

Figure A1: Baseline Runner Velocity Measurements and Plot.

Phase I - 0° (Horizontal) to Match Baseline Production Condition (Vavg.=0.7ms-1)

Connector No	Dist between probes (m)	Dist to probe from 0 (m)	Time made	Time between probes (s)	Cumulative time to probe (s)	Ph I V between probes (ms-1)	Average Velocity to Probe (ms-1)
PL-0	0.000	0.000	39.0	0.0	0.0	0.0	0.0
PL-1	0.145	0.145	39.2	0.2	0.2	0.7	0.7
PL-2	0.117	0.263	39.4	0.2	0.4	0.6	0.7
PL-3	0.106	0.369	39.5	0.1	0.5	1.1	0.7
PL-4	0.098	0.468	39.7	0.2	0.7	0.5	0.7
PL-5	0.073	0.541	39.8	0.1	0.8	0.7	0.7

Vavg = 0.7 ms^{-1}

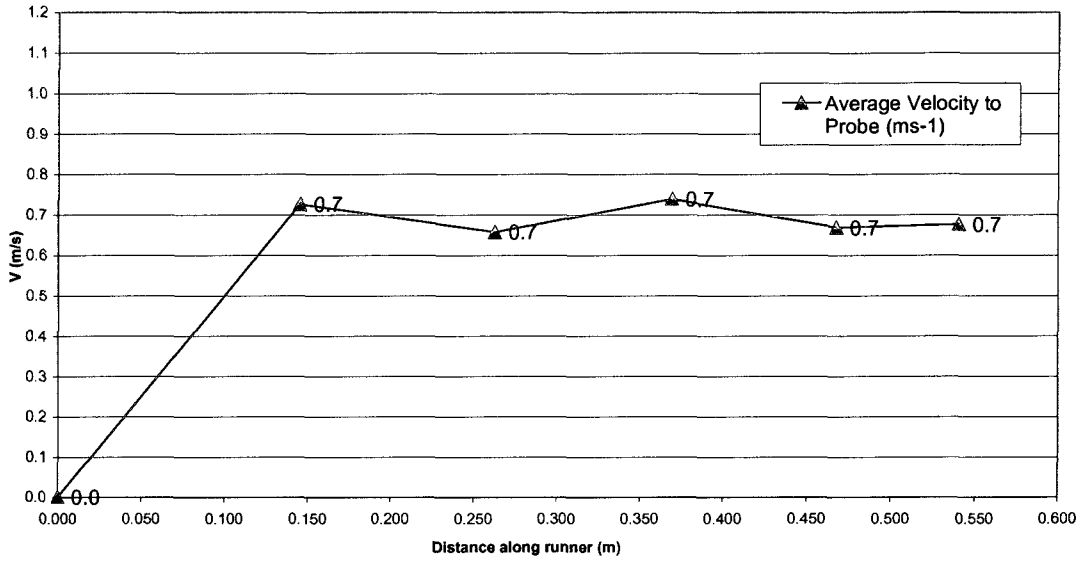

Figure A2: Phase I Runner Velocity Measurements and Plot.

Phase II - 18° Slope With Same Pour Rate as Phase I (Vavg.=1.1ms^{-1})

Connector No	Dist between probes (m)	Dist to probe from 0 (m)	Time made	Time between probes (s)	Cumulative time to probe (s)	Ph II V between probes (ms-1)	Average Velocity to Probe (ms-1)
PL-1	0.000	0.000	35.4	0.0	0.0	0.0	0.0
PL-2	0.147	0.147	35.6	0.2	0.2	0.7	0.7
PL-3	0.138	0.284	35.7	0.1	0.3	1.4	0.9
PL-4	0.127	0.412	35.8	0.1	0.4	1.3	1.0
PL-5	0.121	0.533	35.9	0.1	0.5	1.2	1.1

Vavg = 1.1 ms^{-1}

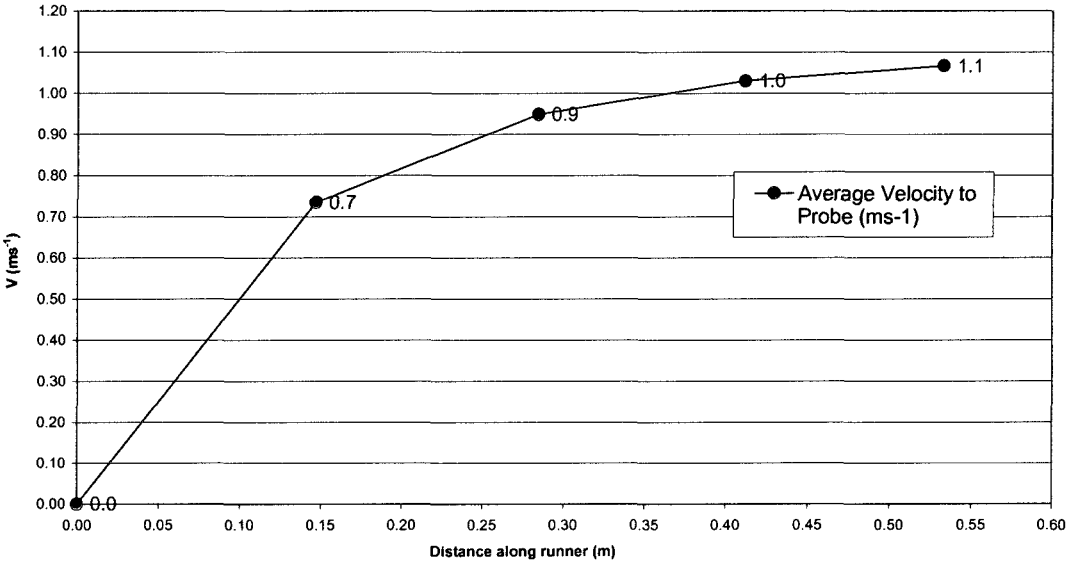

Figure A3: Phase II Runner Velocity Measurements and Plot.

Phase III - 5° Slope with Slow Pour (Vavg. = 0.3ms^{-1})

Connector No	Dist between probes (m)	Dist to probe from 0 (m)	Time made	Time between probes (ms-1)	Cumulative time to probe (s)	Ph III V between probes (ms-1)	Average Velocity to Probe (ms^{-1})
PL-0	0.000	0.000	13.0	0.0	0.0	0.0	0.0
PL-1	0.126	0.126	13.3	0.3	0.3	0.4	0.4
PL-2	0.128	0.254	13.6	0.3	0.6	0.4	0.4
PL-3	0.141	0.395	14.1	0.5	1.1	0.3	0.4
PL-4	0.128	0.523	14.6	0.5	1.6	0.3	0.3

Vavg = 0.3 ms^{-1}

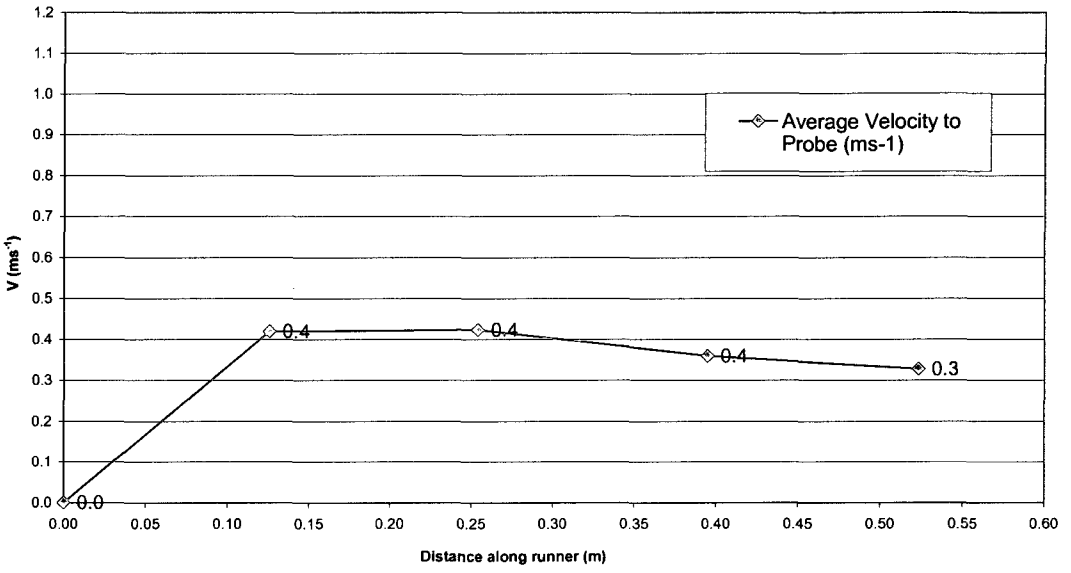

Figure A4: Phase III Runner Velocity Measurements and Plot.

Appendix C
Aluminum Alloy Specification

All test bars were cast from a hybrid of 319 aluminum, whose chemistry is specified in Table A2.

Table A2: Alloy Specification.

ELEMENT	SYMBOL	Nominal (%)
SILICON	Si	7.5
COPPER	Cu	3.5
IRON	Fe	0.40 max
MAGNESIUM	Mg	0.30
MANGANESE	Mn	0.25
ZINC	Zn	0.25 max
TITANIUM	Ti	0.12
STRONTIUM	Sr	0.002 max
NICKEL	Ni	0.10 max
TIN	Sn	0.008 max
LEAD	Pb	0.10 max
SODIUM	Na	0.002 max
CALCIUM	Ca	0.002 max
CHROMIUM	Cr	0.1 max
PHOSPHOROUS	P	0.01 max
LITHIUM	Li	0.0008 max
BISMUTH	Bi	0.010 max
BORON	B	0.01 max
GALLIUM	Ga	0.01 max
ANTIMONY	Sb	0.01 max
ARSENIC	As	0.01 max
Others Each		0.05 max
Others Total		0.5 max

Appendix D

Chemistry Sampling Data (Spectrometer Analysis)

The data Table A3 was obtained on aluminum samples taken from the furnace well within ten minutes of pouring each runner series.

Table A3: Spectrometer Analysis for Phase I Chemistry Checks.

Sample 1 (Phase I)

Try	Si	Cu	Fe	Mg	Mn	Zn	Ti	Sr	Ni	Sn	Pb
1	7.72	3.48	0.44	0.27	0.27	0.20	0.12	0.0028	0.035	0.0032	0.011
2	7.65	3.45	0.43	0.26	0.27	0.20	0.12	0.0028	0.034	0.0030	0.010
3	7.62	3.43	0.43	0.26	0.27	0.20	0.12	0.0028	0.034	0.0031	0.010
Avg	7.66	3.45	0.44	0.26	0.27	0.20	0.12	0.0028	0.034	0.0031	0.010

Out of specification: Fe (.44) Sr (.0028)

Try	Na	Ca	Cr	P	Li	B	Sb	Be	Bi	Cd	V	Zr	Al
1	0.0001	0.0005	0.061	0.002	0.0001	0	0.001	0	0.0015	0	0.01	0.003	87.36
2	0.0001	0.0005	0.060	0.002	0.0001	0	0.001	0	0.0014	0	0.01	0.003	87.49
3	0.0001	0.0005	0.060	0.002	0.0001	0	0.001	0	0.0020	0	0.01	0.003	87.53
Avg	0.0001	0.0005	0.060	0.002	0.0001	0	0.001	0	0.0014	0	0.01	0.003	87.46

Sample 2 (Phase I)

Try	Si	Cu	Fe	Mg	Mn	Zn	Ti	Sr	Ni	Sn	Pb
1	7.68	3.46	0.45	0.26	0.28	0.20	0.12	0.0028	0.035	0.0031	0.010
2	7.65	3.46	0.44	0.27	0.27	0.22	0.12	0.0028	0.035	0.0032	0.010
3	7.61	3.44	0.43	0.26	0.27	0.20	0.12	0.0027	0.034	0.0030	0.010
Avg	7.65	3.45	0.44	0.26	0.27	0.20	0.12	0.0028	0.034	0.0031	0.010

Out of specification: Fe (.45) Sr (.0028)

Try	Na	Ca	Cr	P	Li	B	Sb	Be	Bi	Cd	V	Zr	Al
1	0.0001	0.0005	0.061	0.002	0.0001	0	0.001	0	0.0015	0	0.01	0.0030	87.42
2	0.0001	0.0005	0.060	0.002	0.0001	0	0.001	0	0.0014	0	0.01	0.0003	87.46
3	0.0001	0.0005	0.060	0.001	0.0001	0	0.001	0	0.0013	0	0.01	0.0003	87.54
Avg	0.0001	0.0005	0.060	0.002	0.0001	0	0.001	0	0.0014	0	0.01	0.003	87.48

Sample 3 (Phase I)

Try	Si	Cu	Fe	Mg	Mn	Zn	Ti	Sr	Ni	Sn	Pb
1	7.61	3.45	0.44	0.22	0.27	0.20	0.12	0.0023	0.034	0.0032	0.010
2	7.65	3.39	0.44	0.22	0.27	0.20	0.12	0.0023	0.034	0.0030	0.010
3	7.56	3.38	0.43	0.22	0.26	0.20	0.12	0.0023	0.034	0.0030	0.010
Avg	7.61	3.41	0.44	0.22	0.27	0.20	0.12	0.0023	0.034	0.0031	0.010

Out of specification: Fe (.44) Mg (.22) Sr (.0023)

Try	Na	Ca	Cr	P	Li	B	Sb	Be	Bi	Cd	V	Zr	Al
1	0.0001	0.0006	0.060	0.002	0.0001	0	0.001	0	0.0015	0	0.01	0.0003	87.55
2	0.0001	0.0006	0.060	0.002	0.0001	0	0.001	0	0.0014	0	0.01	0.003	87.58
3	0.0001	0.0006	0.059	0.002	0.0001	0	0.001	0	0.0013	0	0.01	0.003	87.69
Avg	0.0001	0.0006	0.060	0.002	0.0001	0	0.001	0	0.0014	0	0.01	0.003	87.61

Table A4: Spectrometer Analysis for Phase II Chemistry Checks.

Sample 4 (Phase II)

Try	Si	Cu	Fe	Mg	Mn	Zn	Ti	Sr	Ni	Sn	Pb
1	7.56	3.54	0.45	0.23	0.27	0.20	0.12	0.0023	0.035	0.0032	0.011
2	7.67	3.37	0.44	0.22	0.27	0.20	0.12	0.0023	0.034	0.0030	0.010
3	7.65	3.36	0.44	0.22	0.27	0.20	0.12	0.0023	0.034	0.0029	0.010
Avg	7.63	3.42	0.44	0.22	0.27	0.20	0.12	0.0023	0.034	0.0031	0.010

Out of specification: Fe (.44) Mg (.22) Sr (.0023)

Try	Na	Ca	Cr	P	Li	B	Sb	Be	Bi	Cd	V	Zr	Al
1	0.0001	0.0007	0.061	0.001	0.0001	0	0.001	0	0.0015	0	0.01	0.003	87.49
2	0.0001	0.0006	0.060	0.002	0.0001	0	0.001	0	0.0014	0	0.01	0.003	87.59
3	0.0001	0.0006	0.060	0.002	0.0001	0	0.001	0	0.0013	0	0.01	0.003	87.63
Avg	0.0001	0.0006	0.060	0.002	0.0001	0	0.001	0	0.0014	0	0.01	0.003	87.57

Sample 5 (Phase II)

Try	Si	Cu	Fe	Mg	Mn	Zn	Ti	Sr	Ni	Sn	Pb
1	7.56	3.50	0.45	0.22	0.27	0.20	0.12	0.0023	0.035	0.0032	0.011
2	7.61	3.42	0.44	0.21	0.27	0.20	0.12	0.0022	0.034	0.0032	0.010
3	7.69	3.33	0.43	0.21	0.26	0.20	0.12	0.0022	0.034	0.0030	0.010
Avg	7.62	3.42	0.44	0.22	0.27	0.20	0.12	0.0023	0.034	0.0032	0.010

Out of specification: Fe (.44) Mg (.22) Sr (.0023)

Try	Na	Ca	Cr	P	Li	B	Sb	Be	Bi	Cd	V	Zr	Al
1	0.0001	0.0007	0.061	0.002	0.0001	0	0.001	0	0.0016	0	0.01	0.003	87.54
2	0.0001	0.0006	0.060	0.002	0.0001	0	0.001	0	0.0014	0	0.01	0.003	87.60
3	0.0001	0.0006	0.059	0.002	0.0001	0	0.001	0	0.0013	0	0.01	0.003	87.62
Avg	0.0001	0.0006	0.060	0.002	0.0001	0	0.001	0	0.0014	0	0.01	0.003	87.59

Table A5: Spectrometer Analysis for Phase III Chemistry Checks.

Sample 6 (Phase III)

Try	Si	Cu	Fe	Mg	Mn	Zn	Ti	Sr	Ni	Sn	Pb
1	7.68	3.47	0.44	0.23	0.27	0.20	0.12	0.0024	0.035	0.0032	0.011
2	7.64	3.44	0.44	0.23	0.27	0.20	0.12	0.0024	0.034	0.0032	0.010
3	7.53	3.39	0.43	0.23	0.26	0.20	0.12	0.0024	0.034	0.0031	0.010
Avg	7.61	3.43	0.44	0.23	0.27	0.20	0.12	0.0024	0.034	0.0032	0.100

Out of specification: Fe (.44) Mg (.22) Sr (.0024)

Try	Na	Ca	Cr	P	Li	B	Sb	Be	Bi	Cd	V	Zr	Al
1	0.0001	0.0006	0.060	0.002	0.0001	0	0.001	0	0.0015	0	0.01	0.003	87.45
2	0.001	0.0006	0.060	0.002	0.0001	0	0.001	0	0.0014	0	0.01	0.003	87.54
3	0.0001	0.0006	0.059	0.002	0.0001	0	0.001	0	0.0013	0	0.01	0.003	87.72
Avg	0.0001	0.0006	0.060	0.002	0.0001	0	0.001	0	0.0014	0	0.01	0.003	87.57

Sample 7 (Phase III)

Try	Si	Cu	Fe	Mg	Mn	Zn	Ti	Sr	Ni	Sn	Pb
1	7.63	3.42	0.45	0.23	0.27	0.20	0.12	0.0024	0.034	0.0032	0.010
2	7.62	3.34	0.44	0.22	0.26	0.20	0.12	0.0024	0.034	0.0030	0.010
3	7.52	3.46	0.44	0.23	0.27	0.20	0.12	0.0024	0.035	0.0031	0.011
Avg	7.59	3.41	0.44	0.23	0.27	0.20	0.12	0.0024	0.034	0.0031	0.010

Out of specification: Fe (.44) Mg (.23) Sr (.0024)

Try	Na	Ca	Cr	P	Li	B	Sb	Be	Bi	Cd	V	Zr	Al
1	0.0001	0.0006	0.061	0.001	0.0001	0	0.001	0	0.0016	0	0.01	0.003	8755
2	0.0001	0.0006	0.060	0.002	0.0001	0	0.001	0	0.0015	0	0.01	0.003	87.67
3	0.0001	0.0006	0.060	0.002	0.0001	0	0.001	0	0.0014	0	0.01	0.003	87.63
Avg	0.0001	0.0006	0.060	0.002	0.0001	0	0.001	0	0.0015	0	0.01	0.003	87.62

Appendix E
Radiographic Results

Table A6: Table of Radiographic Results.

Gas (G1-G8) ratings are according to ASTM E-155 standard (G1 =small and G8 =large bubble sizes).
Numbers represent the quantities of bubbles found in the test bar at the respective rating.

	Phase I								Phase II								Phase III							
Sample no.	G1	G2	G3	G4	G5	G6	G7	G8	G1	G2	G3	G4	G5	G6	G7	G8	G1	G2	G3	G4	G5	G6	G7	G8
1	2								4	1	2	3	1											
2									1	1				1										
3									3															
4	2	1							1	1	2		1	1										
5	1								1	1	2	4			1									
6									1	1	3	2	1											
7	3								1	1	3		1											
8		1							3	4	1	1	2		1	1								
9									8	2		2												
10				1					3	3	1	2				1								
11	1		2						4	1	1	1												
12	1	1	2	1					4	3	1	1												
13									4	1	3			1										
14									1	1	1		1	1										
15	1		1						2	3	6													
16									1	1	1		2		1									
17									5	2			1	1	1									
18									7	1	1		1											
19	2	1							1	2	2		1	1										
20	0	1							2		2	1		1										
Total bubbles/size	13	5	5	2	0	0	0	0	57	30	32	17	12	7	4	2	0	0	0	0	0	0	0	0
Total bubble count	25								161								0							
Overall average Initial Transient velocity (ms^{-1})	0.68								1.07								0.33							

Radiographs of test bars 1-6, Phase I

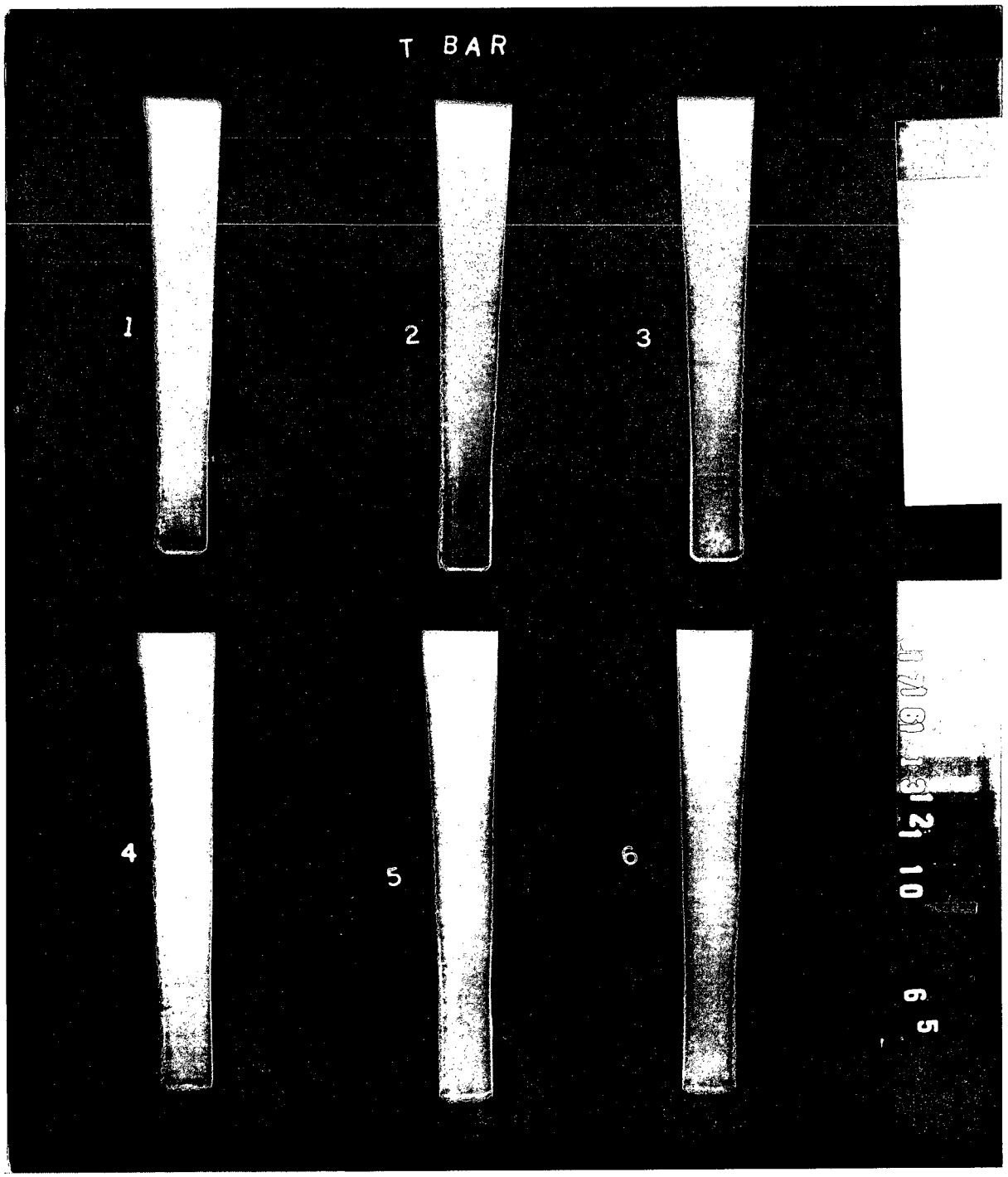

Figure A5: Radiographs of Phase I Test Bars 1 to 6.

Radiographs of test bars 7-13, Phase I

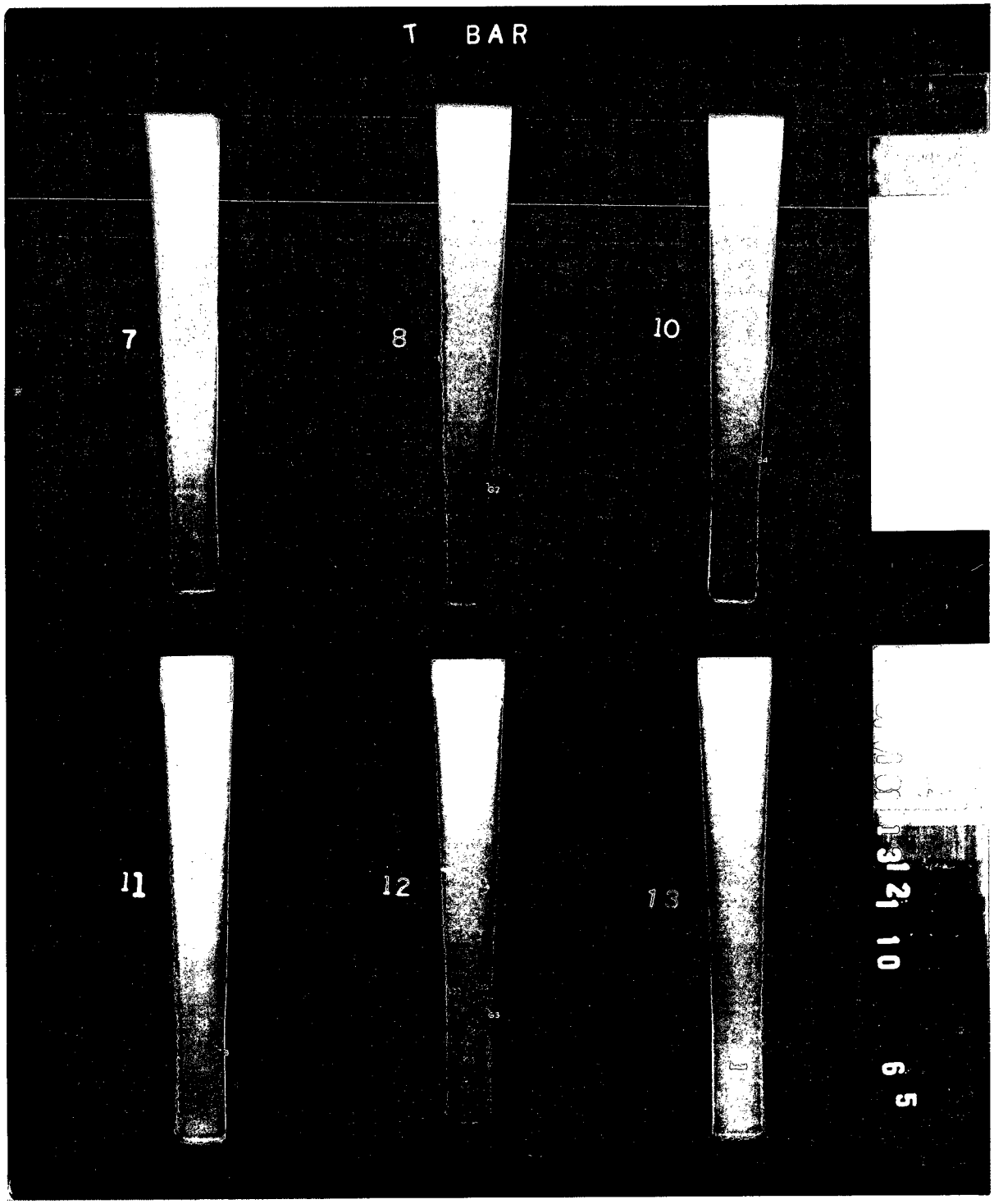

Figure A6: Radiographs of Phase I Test Bars 7 to 13.

Radiographs of test bars 14-20, Phase I

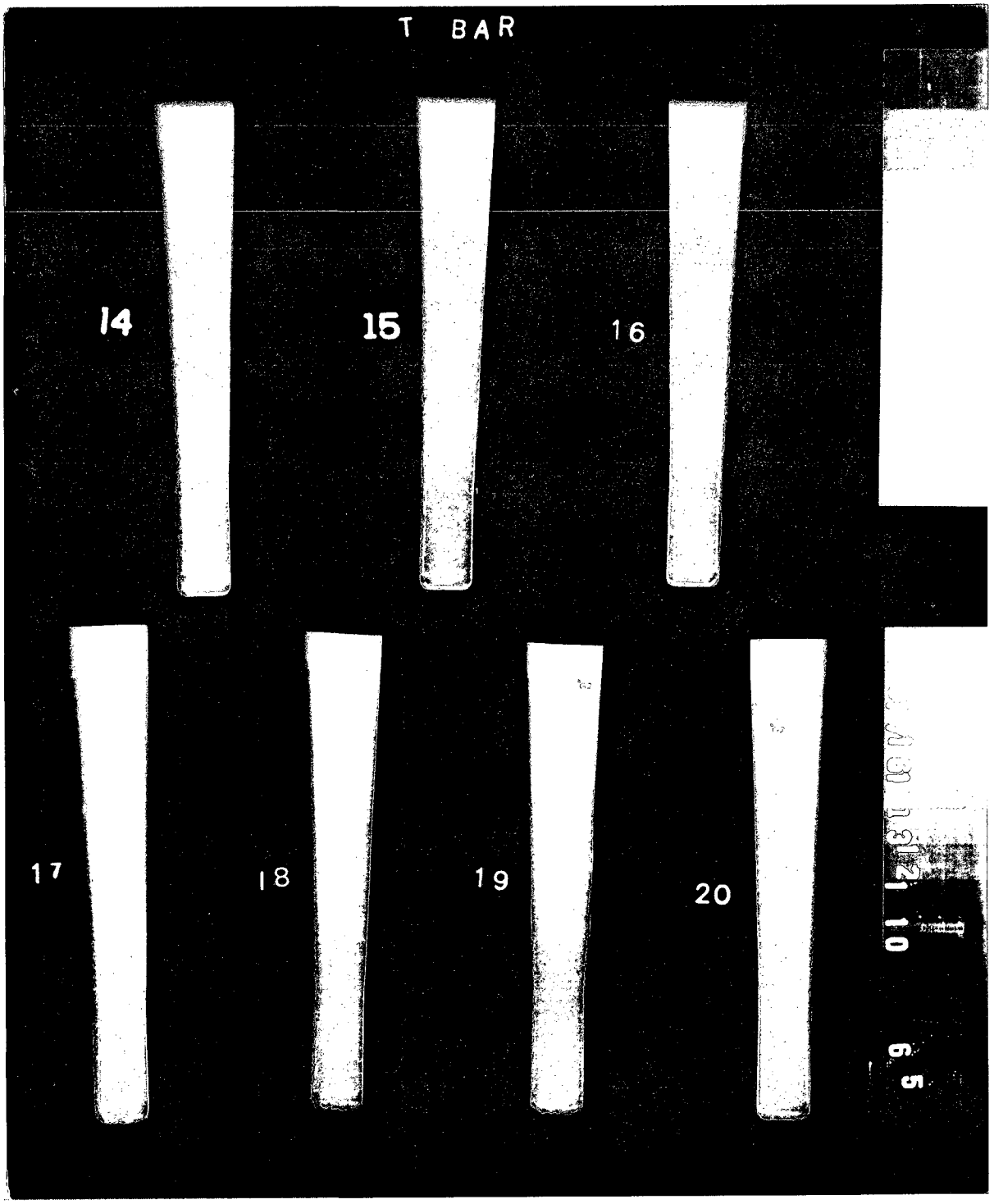

Figure A7: Radiographs of Phase I Test Bars 14 to 20.

Radiographs of test bars 1-6, Phase II

Figure A8: Radiographs of Phase II Test Bars 1 to 6.

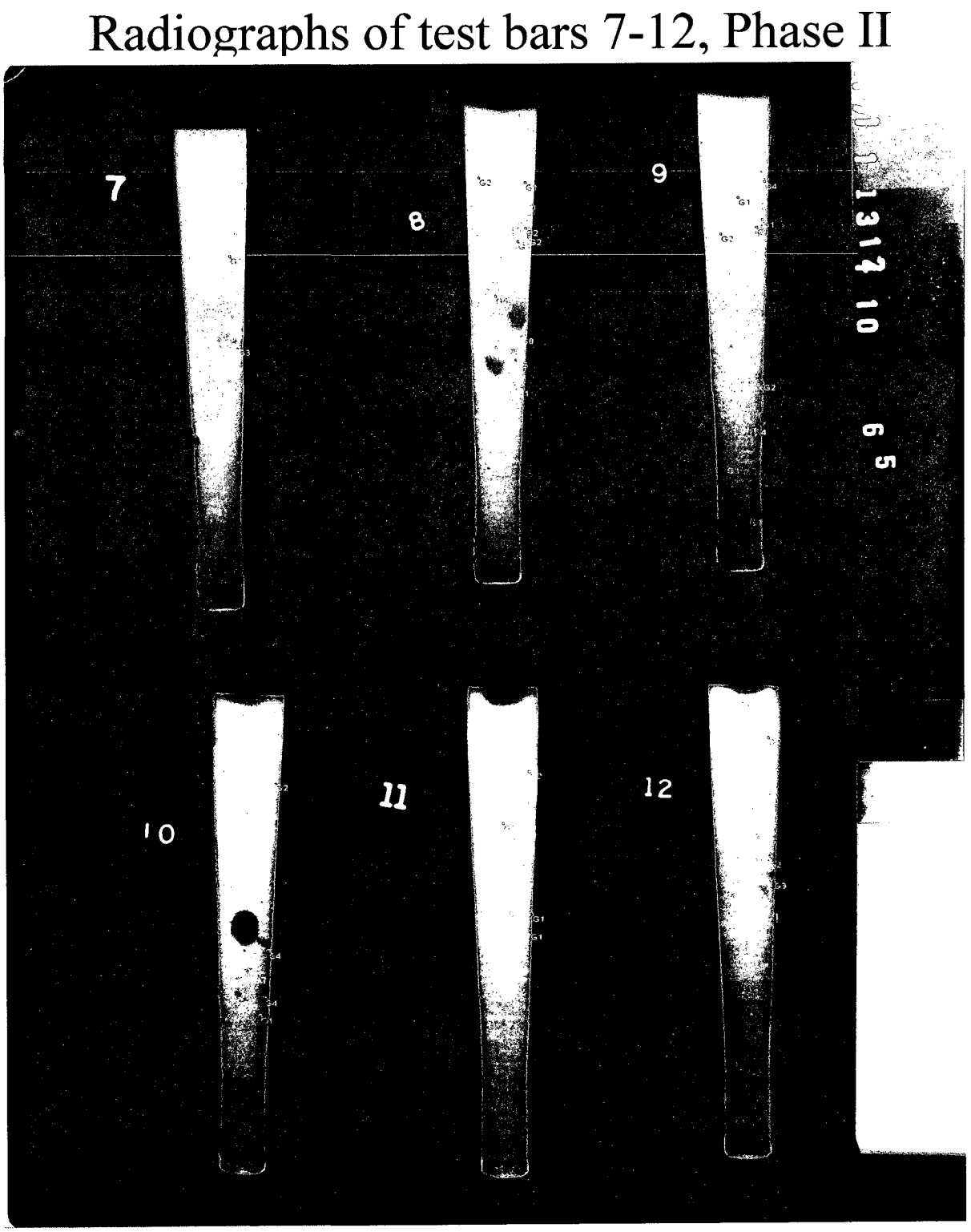

Figure A9: Radiographs of Phase II Test Bars 7 to 12.

Radiographs of test bars 13-18, Phase II

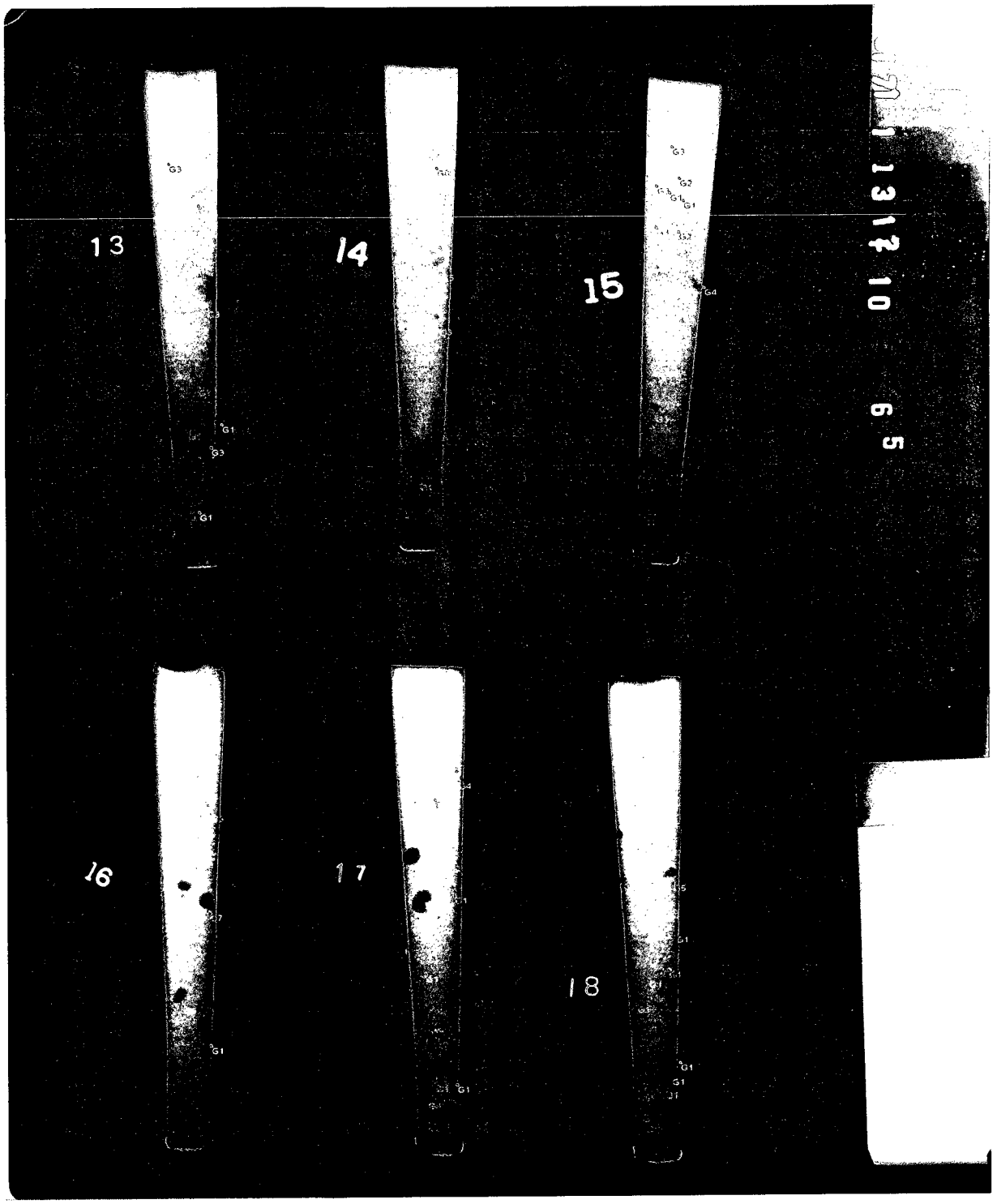

Figure A10: Radiographs of Phase II Test Bars 13 to 18.

Radiographs of test bars 1-4, Phase III

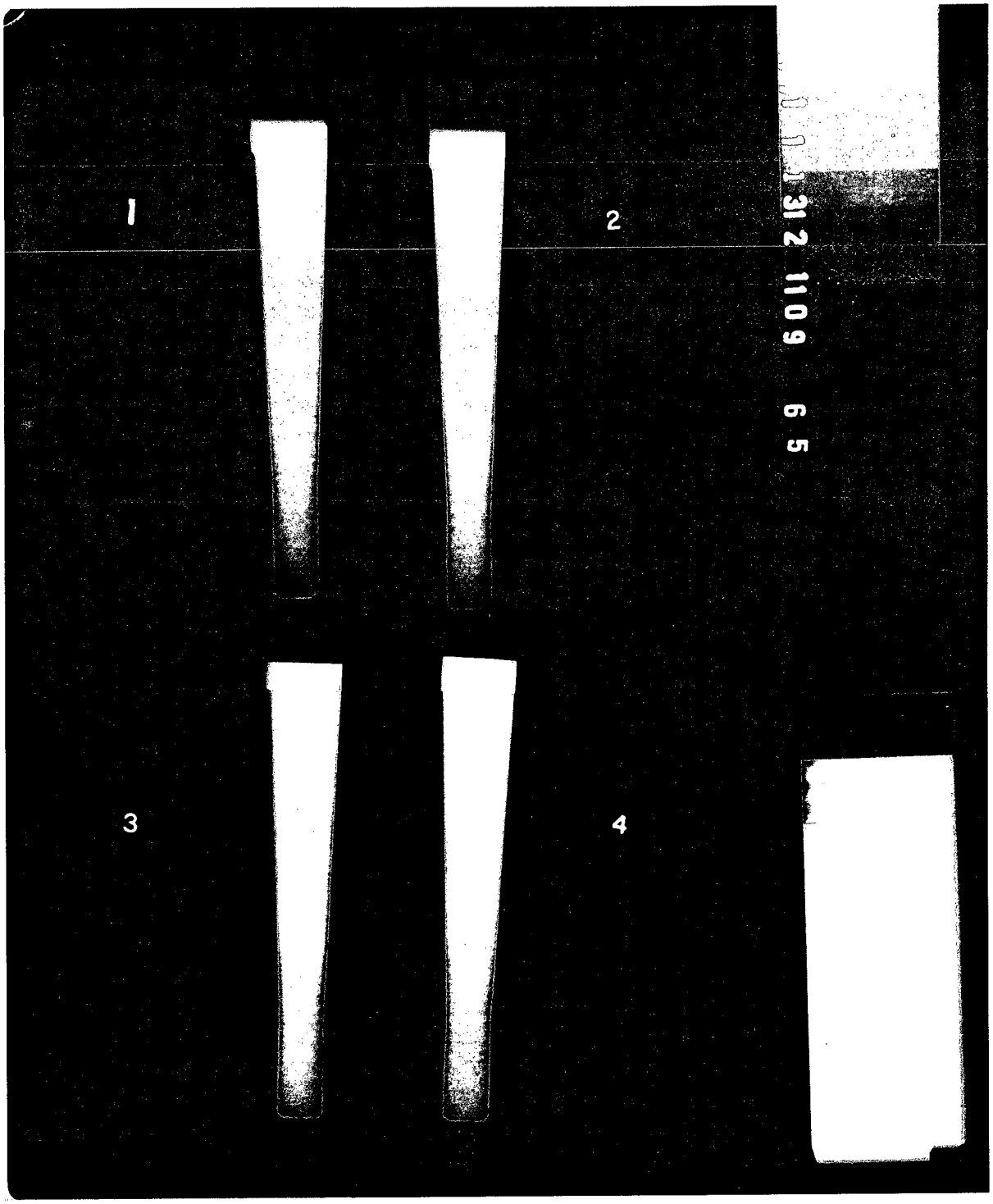

Figure A11: Radiographs of Phase III Test Bars 1 to 4.

Radiographs of test bars 5-8, Phase III

Figure A12: Radiographs of Phase III Test Bars 5 to 8.

Radiographs of test bars 9-12, Phase III

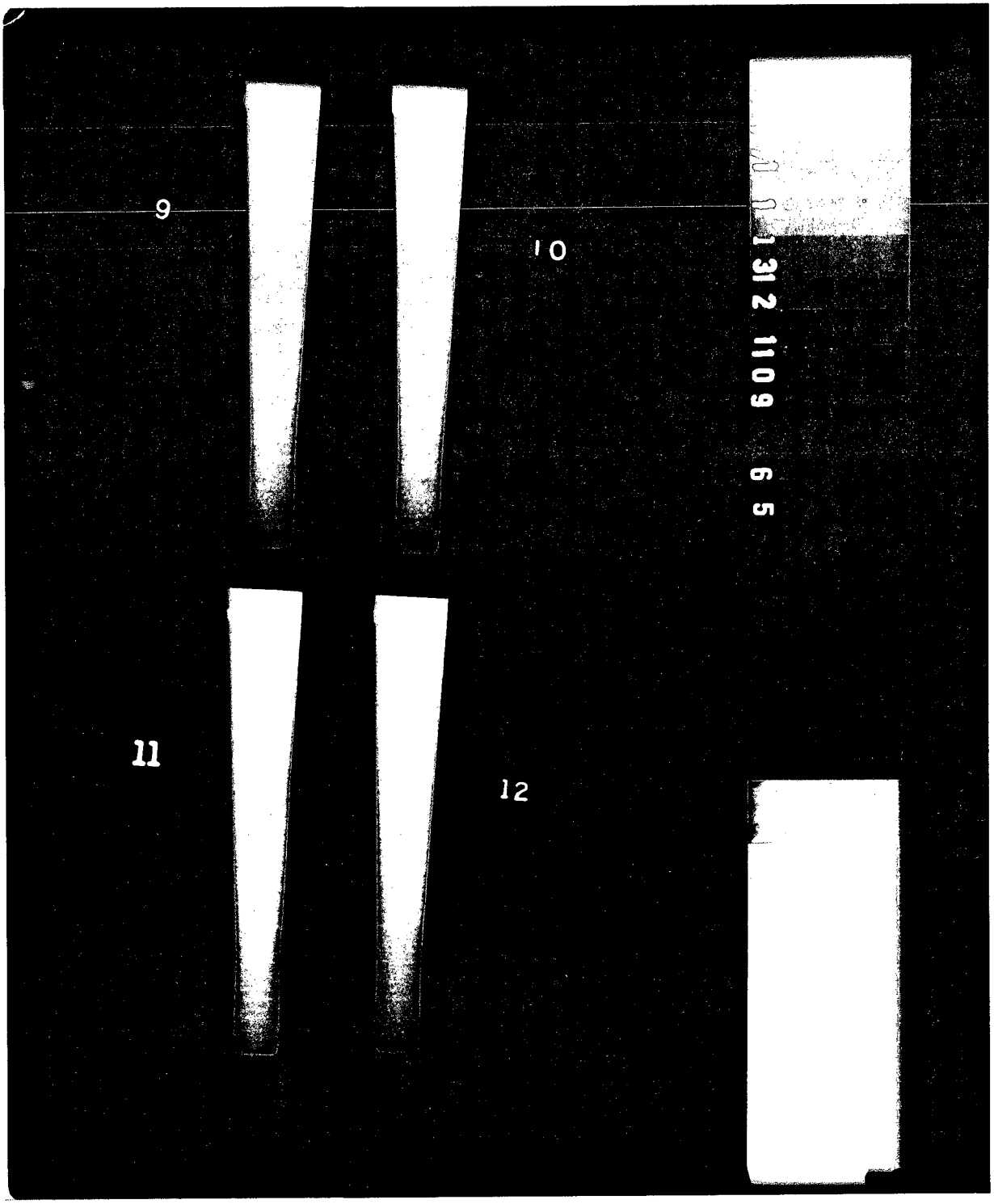

Figure A13: Radiographs of Phase III Test Bars 9 to 12.

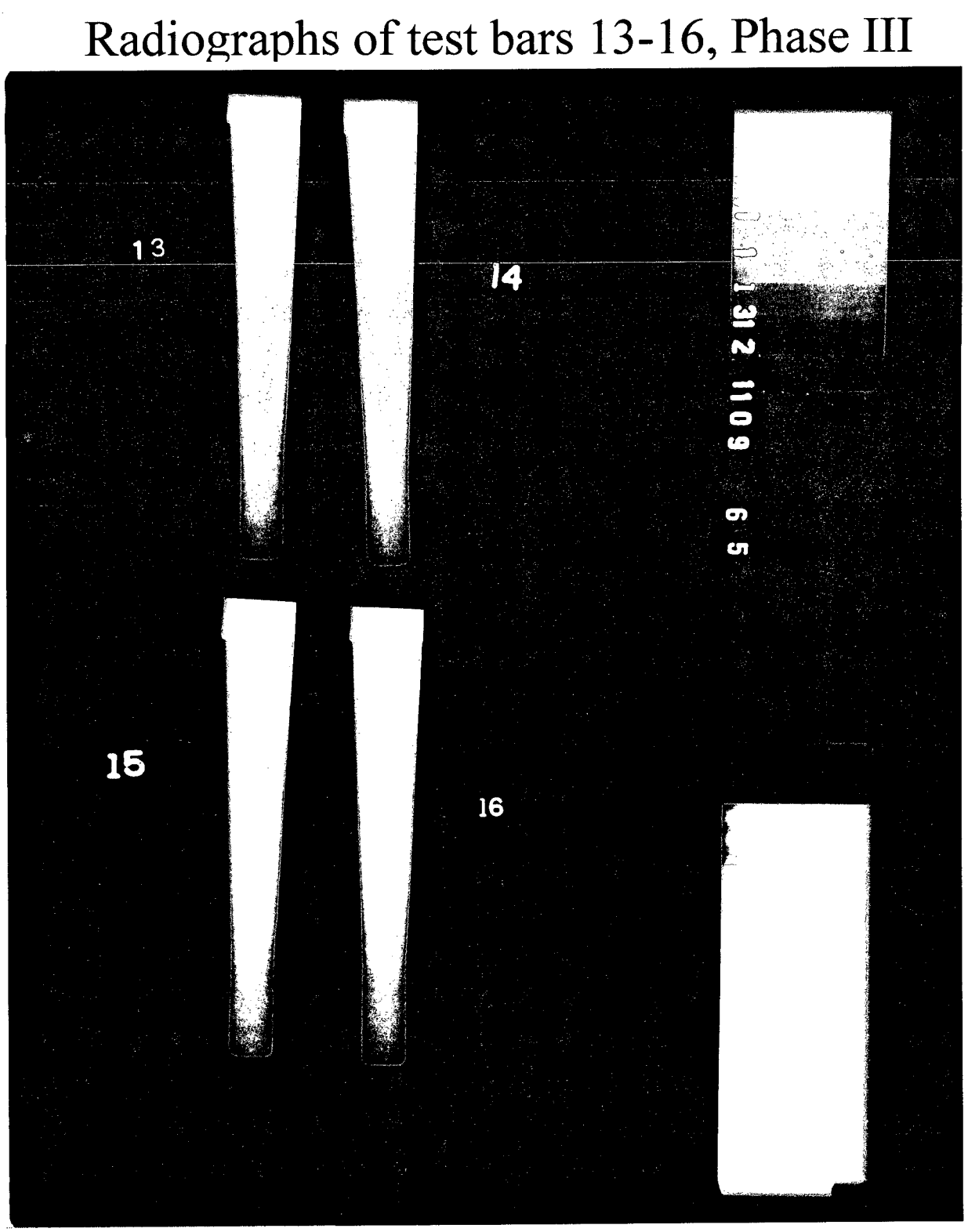

Figure A14: Radiographs of Phase III Test Bars 13 to 16.

Radiographs of test bars 17-20, Phase III

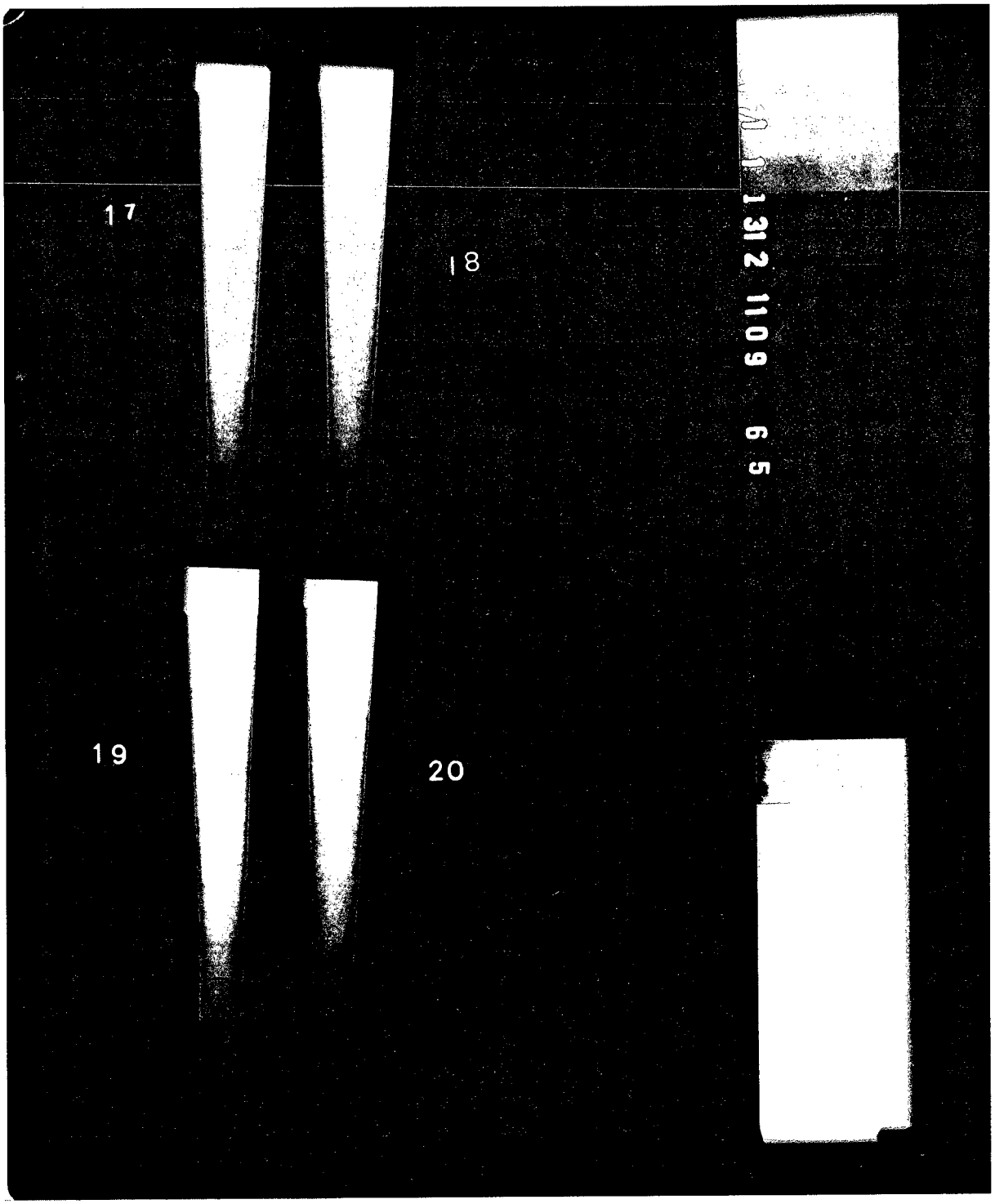

Figure A15: Radiographs of Phase III Test Bars 17 to 20.

Appendix F
Production Casting Tensile Testing Data

Table A7: Mechanical Properties of Production Castings (non-aged).

Sample Location within production casting	Yield Strength -2% offset (MPa)	Ultimate Tensile Strength (MPa)
Bulkhead properties (average) for samples in solution treated, non aged condition.	192	229

Appendix G
SEM Results

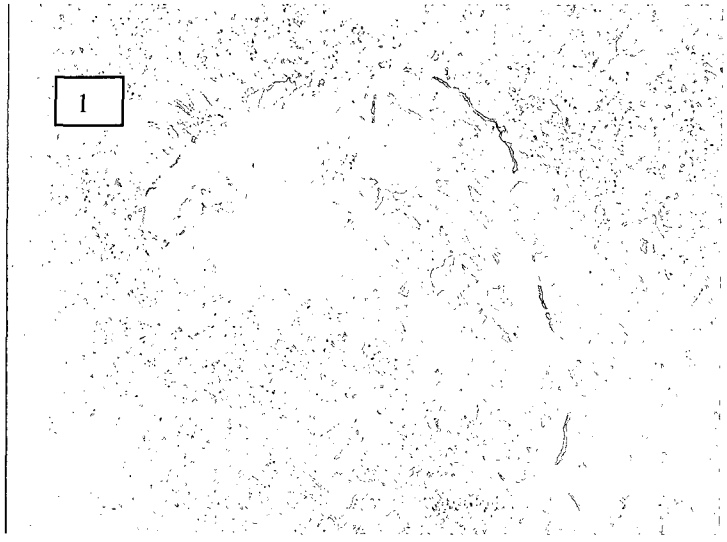

Figure A16: SEM Micrograph of Sample I-4 location 1 (120x magnification).

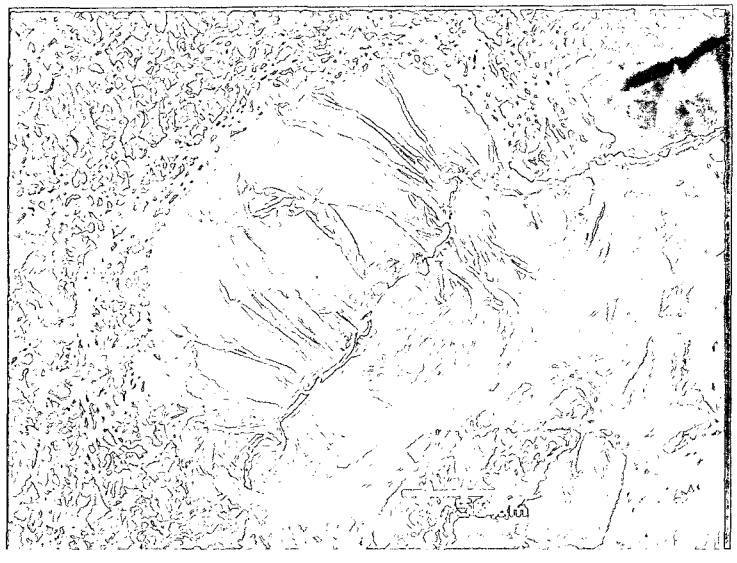

Figure A17: SEM Micrograph of Sample I-4 location 1 (450x magnification).

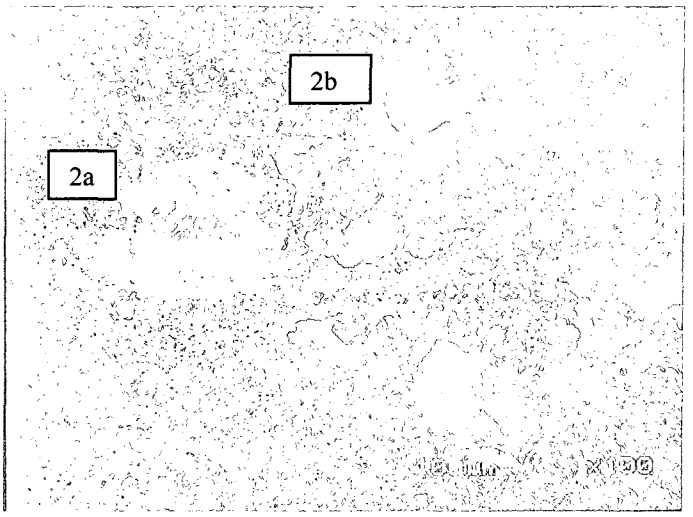

Figure A18: SEM Micrograph of Sample I-4 location 2 (100x magnification).

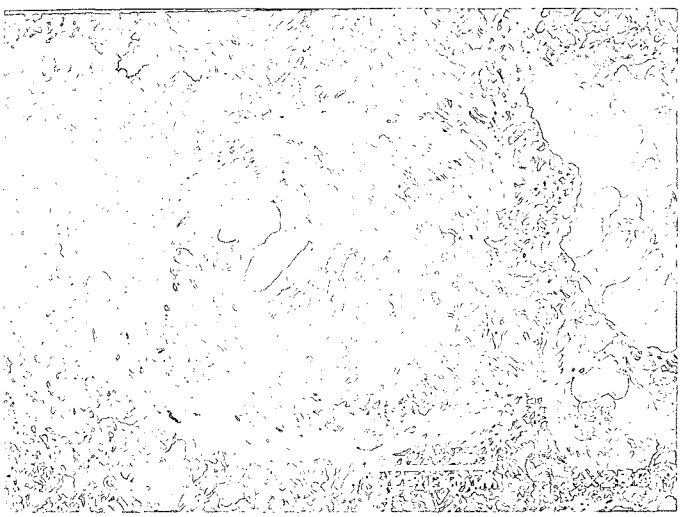

Figure A19: SEM Micrograph of Sample I-4 location 2a (450x magnification).

Figure A20: SEM Micrograph of Sample I-4 location 2b (450x magnification).

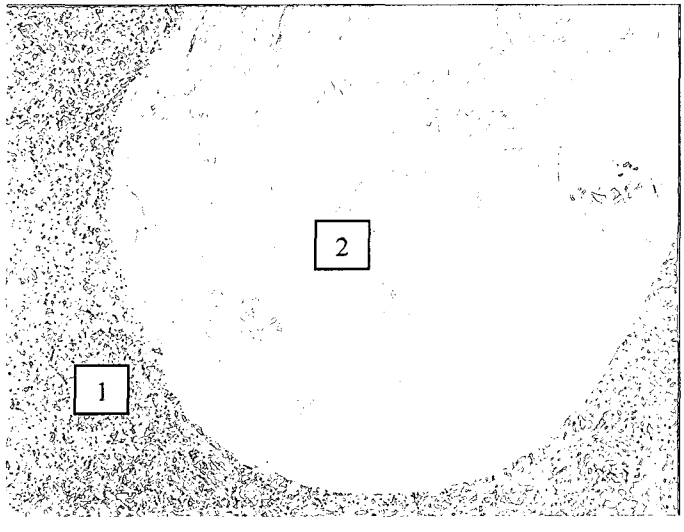

Figure A21: SEM Micrograph of Sample II-6 (50x magnification).

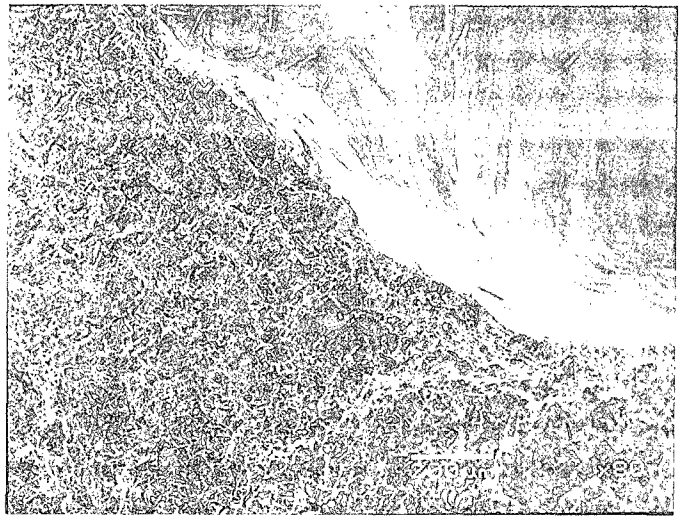

Figure A22: SEM Micrograph of Sample II-6 location 1 (80x magnification).

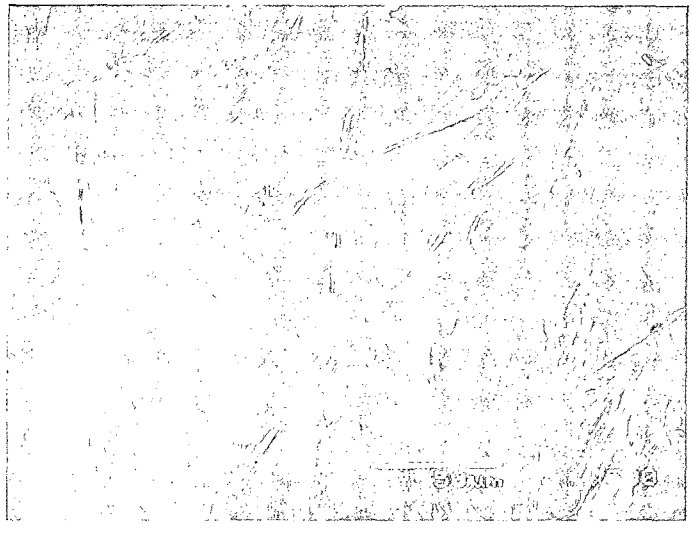

Figure A23: SEM Micrograph of Sample II-6 location 2 (500x magnification).

Appendix H
MagmaSoft Simulation Results

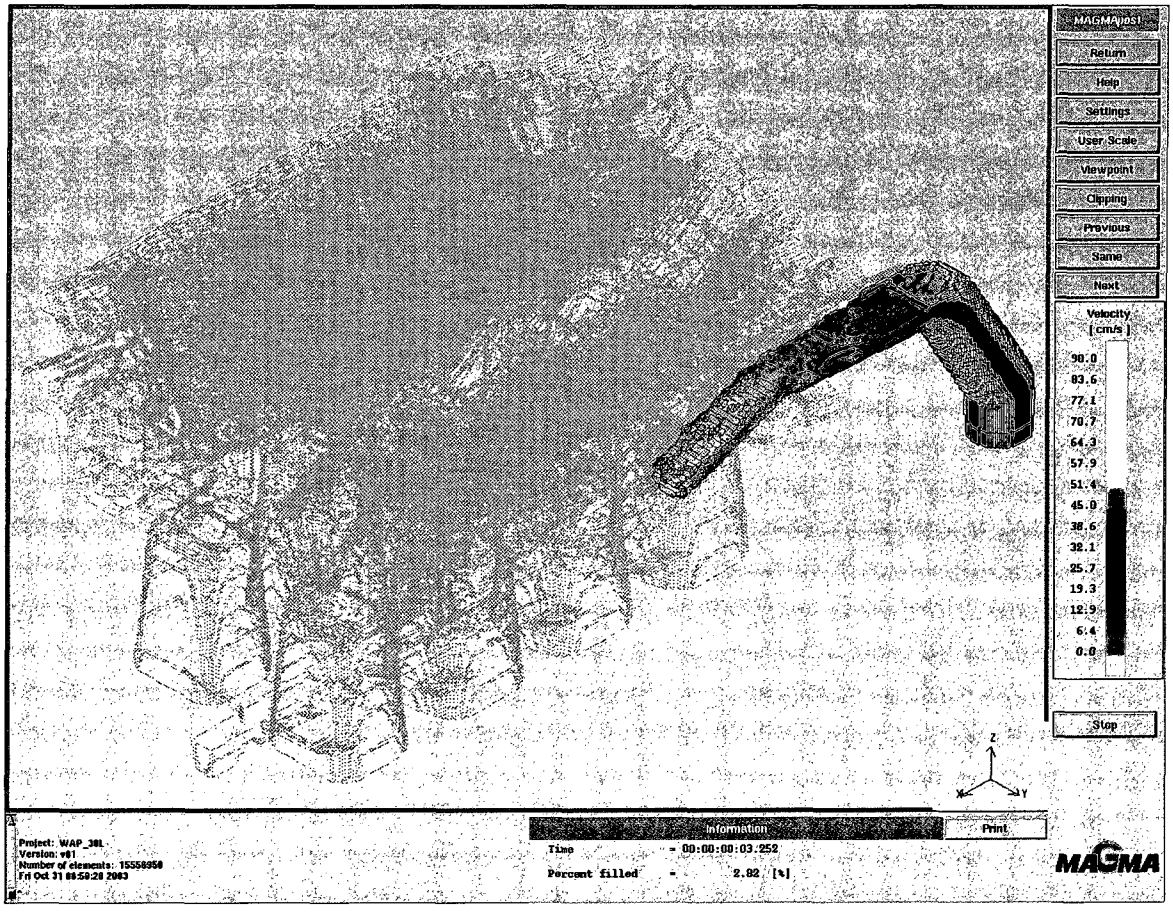

Figure A24: MAGMA 3.0L cylinder block fill simulation-current runner@ 3.2 seconds; Initial Transient is half way down the ramp; V_{IT} is approx 0.7 ms^{-1}.

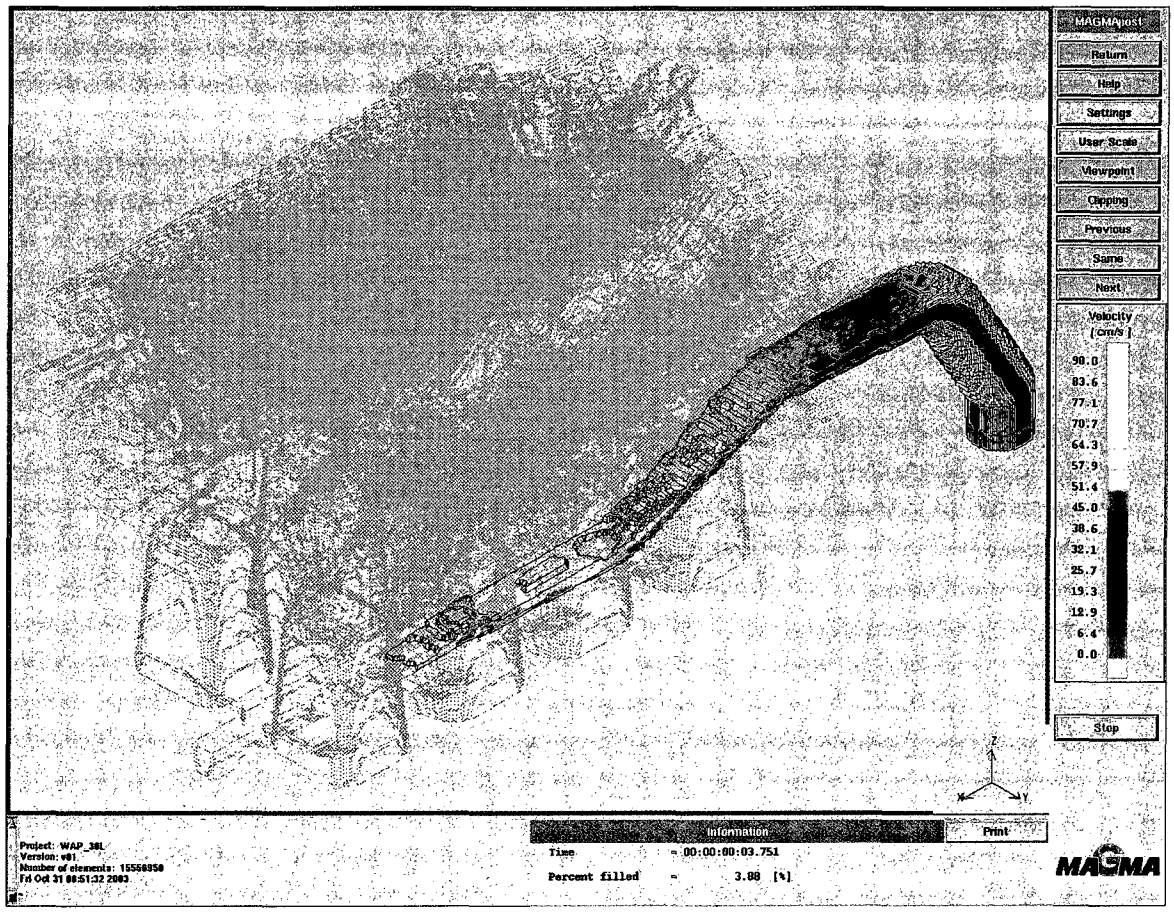

Figure A25: MAGMA 3.0L cylinder block fill simulation-current runner@ 3.2 seconds; Initial Transient is more than half way down the runner's length. V_{IT} remains at approx. 0.7 ms^{-1}. Note the higher velocity nearest the bottom of the ramp during a time when the aluminum in the runner is exposed to air (white).

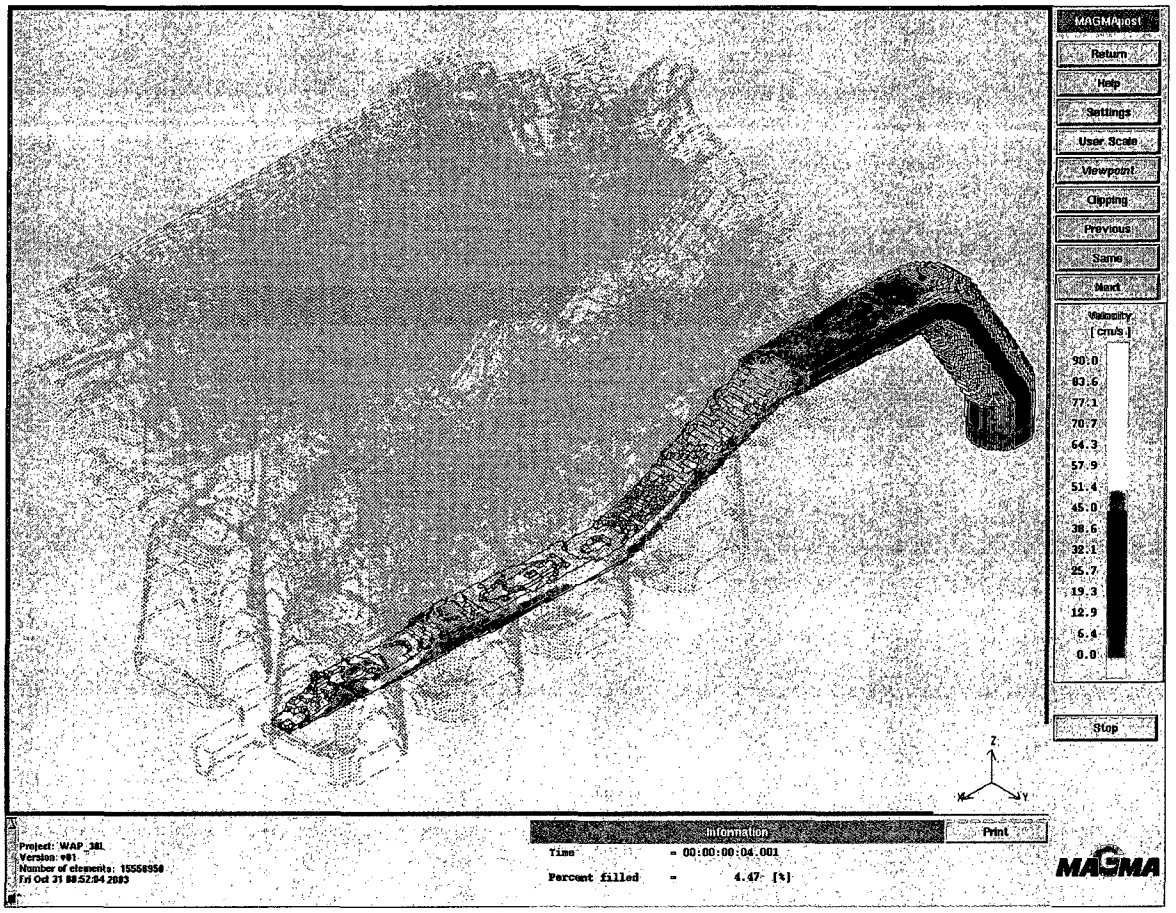

Figure A26: MAGMA 3.0L cylinder block fill simulation-current runner@ 4.0 seconds; Initial Transient is nearing the end of the runner. VIT remains at approx. 0.7 ms^{-1}.

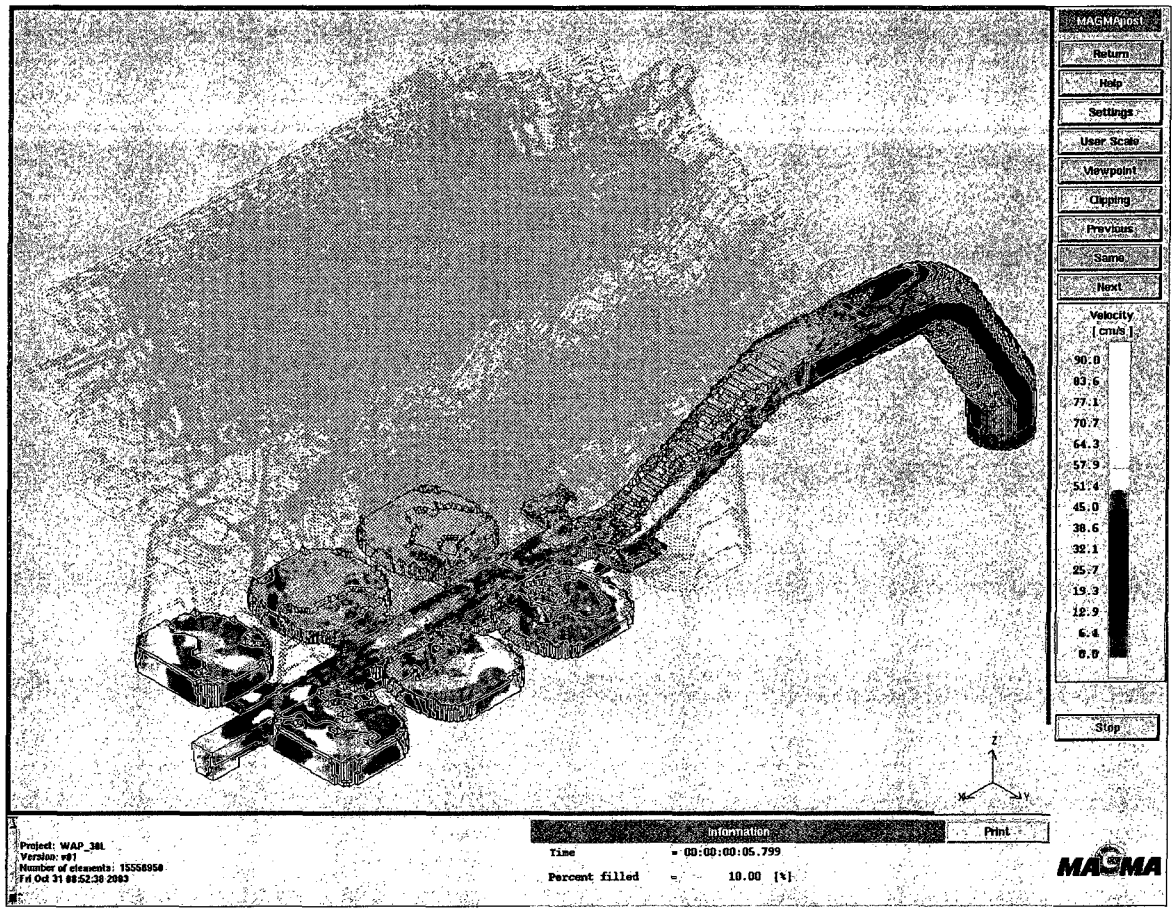

Figure A27: MAGMA 3.0L cylinder block fill simulation-current runner@ 5.8seconds; Simulation of riser fill. V_{IT} is now well below $V_{critical}$

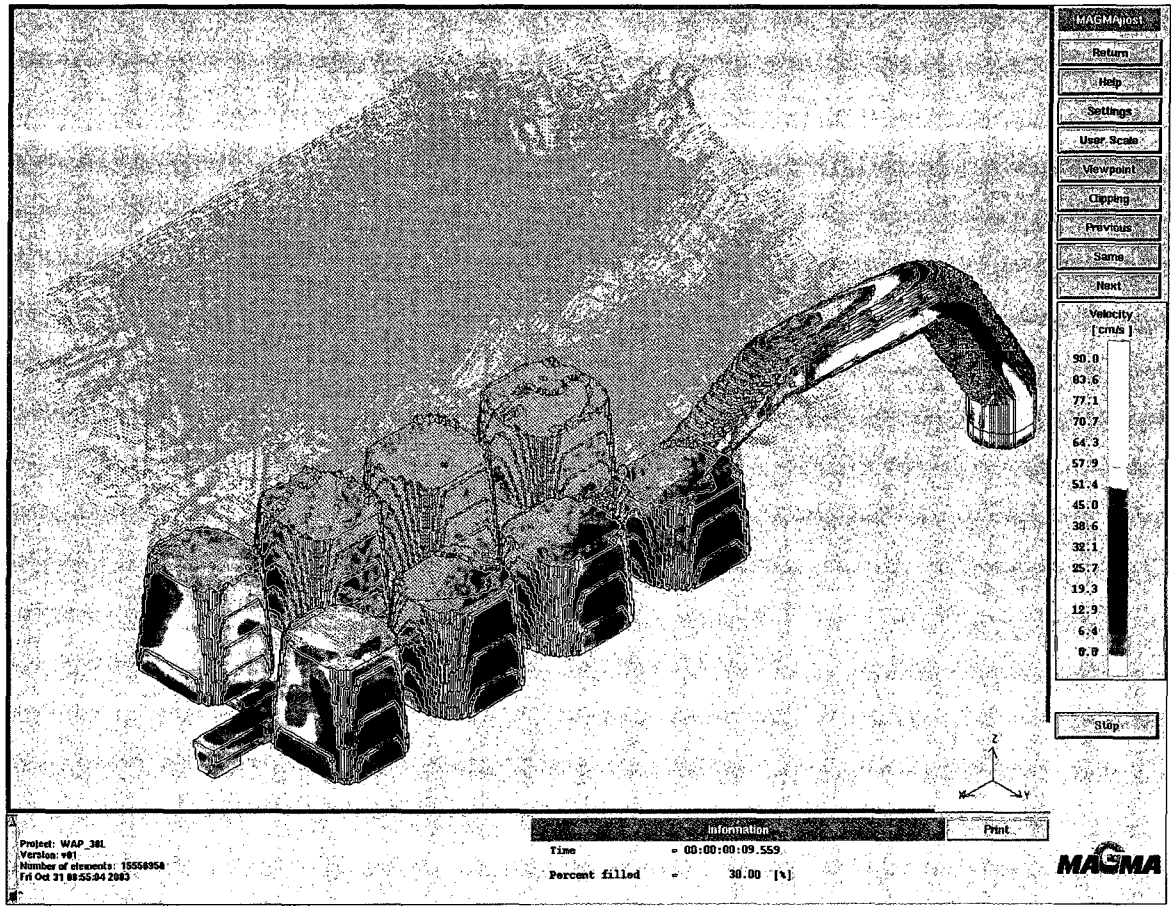

Figure A28: MAGMA 3.0L cylinder block fill simulation-current runner@ 9.6 seconds; risers nearing full.

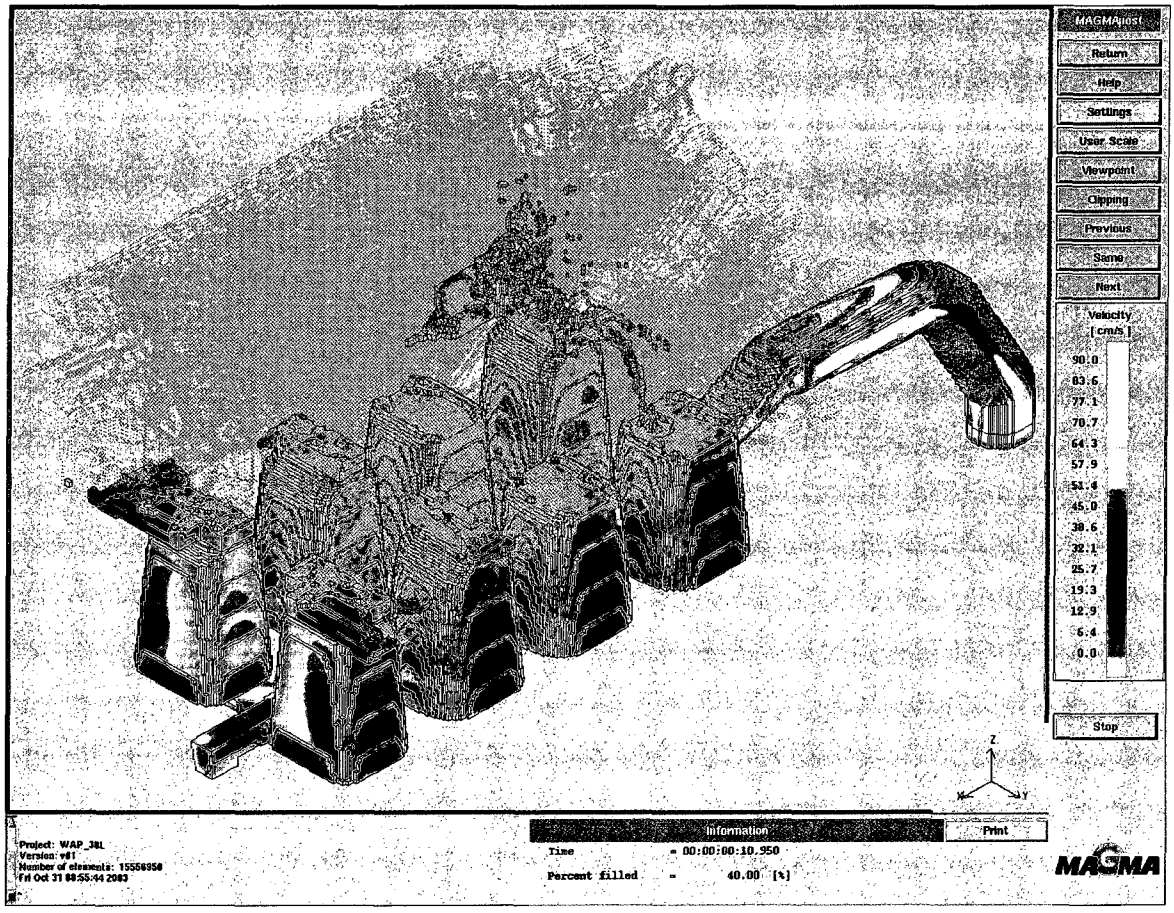

Figure A29: MAGMA 3.0L cylinder block fill simulation-current runner@ 10.9 seconds; fountain effect from one riser contributes to bubbles and oxides within the casting.

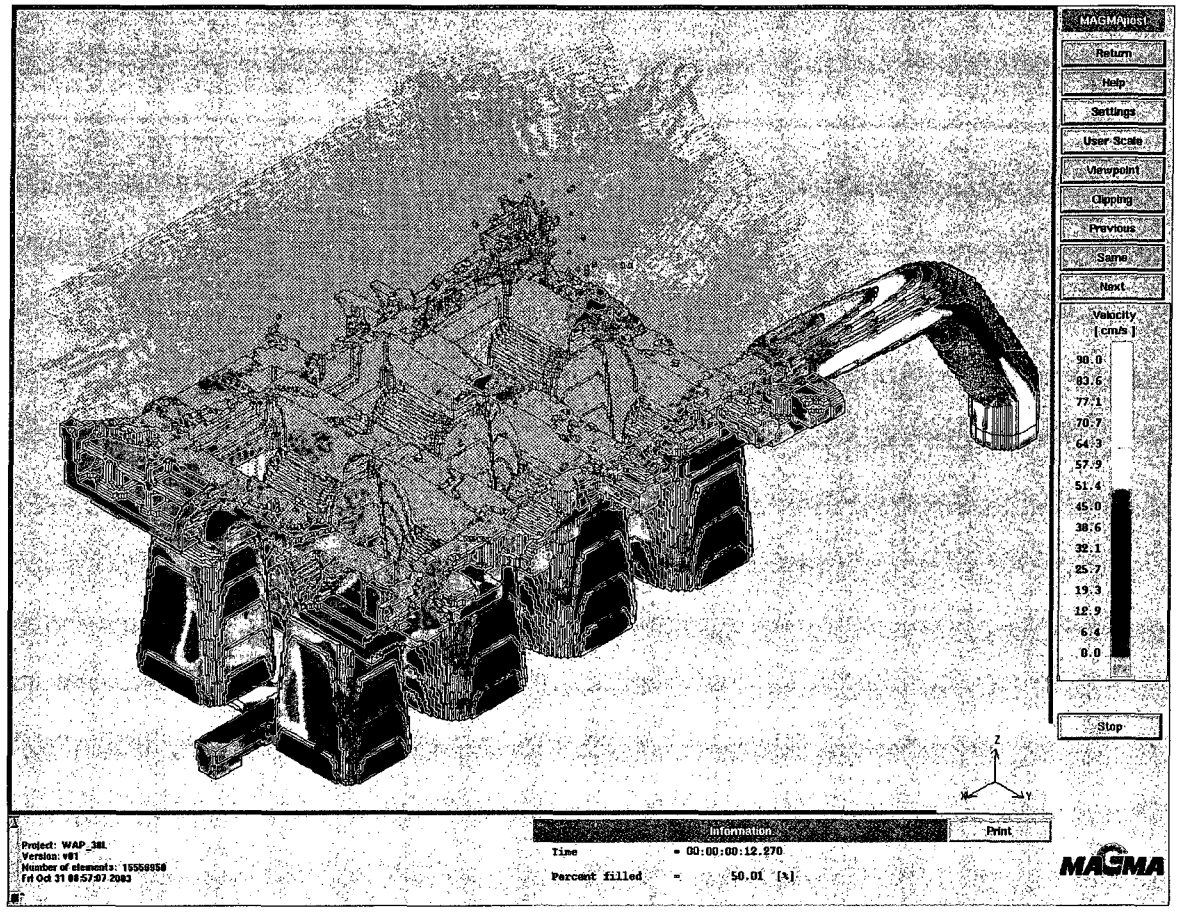

Figure A30: MAGMA 3.0L cylinder block fill simulation-current runner@ 12.2 seconds; Further evidence of fountain effect.

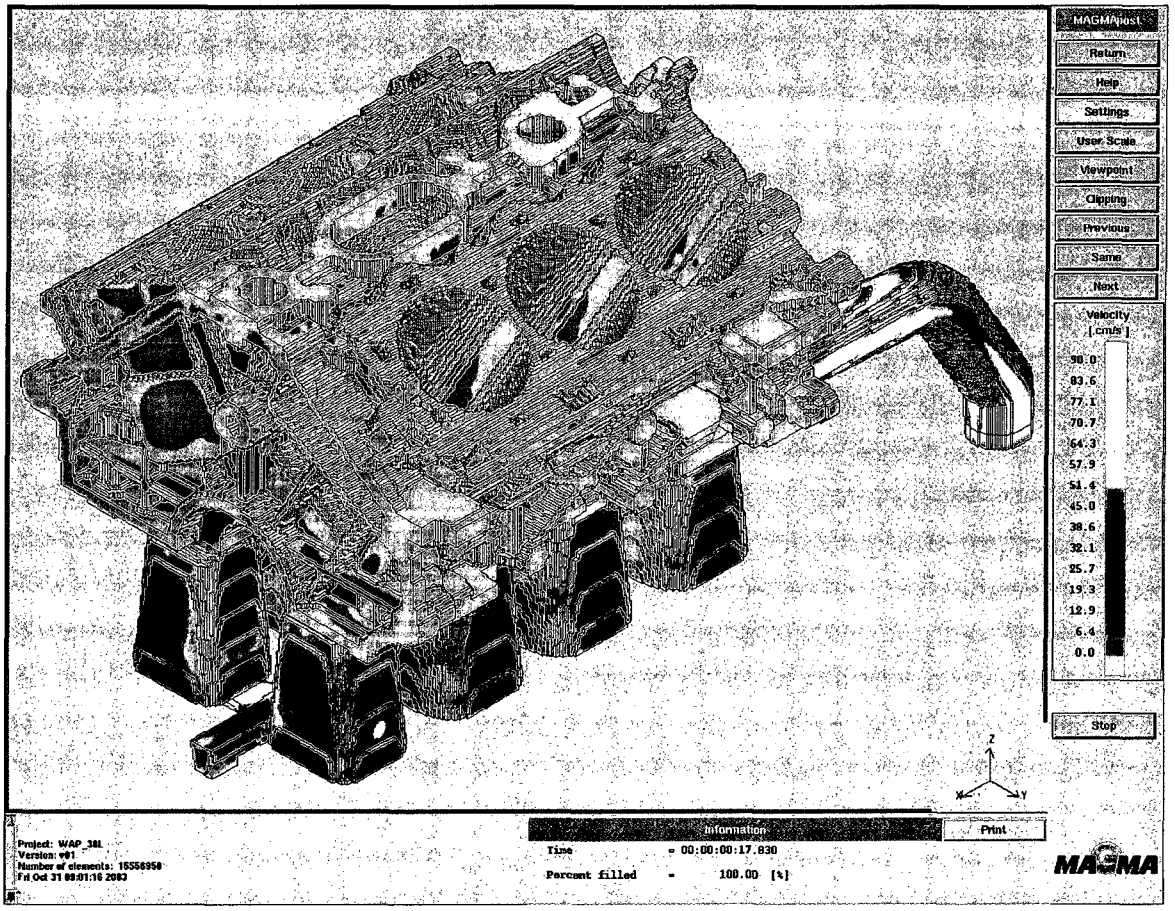

Figure A31: MAGMA 3.0L cylinder block fill simulation-current runner@ 17.8 seconds; complete casting.

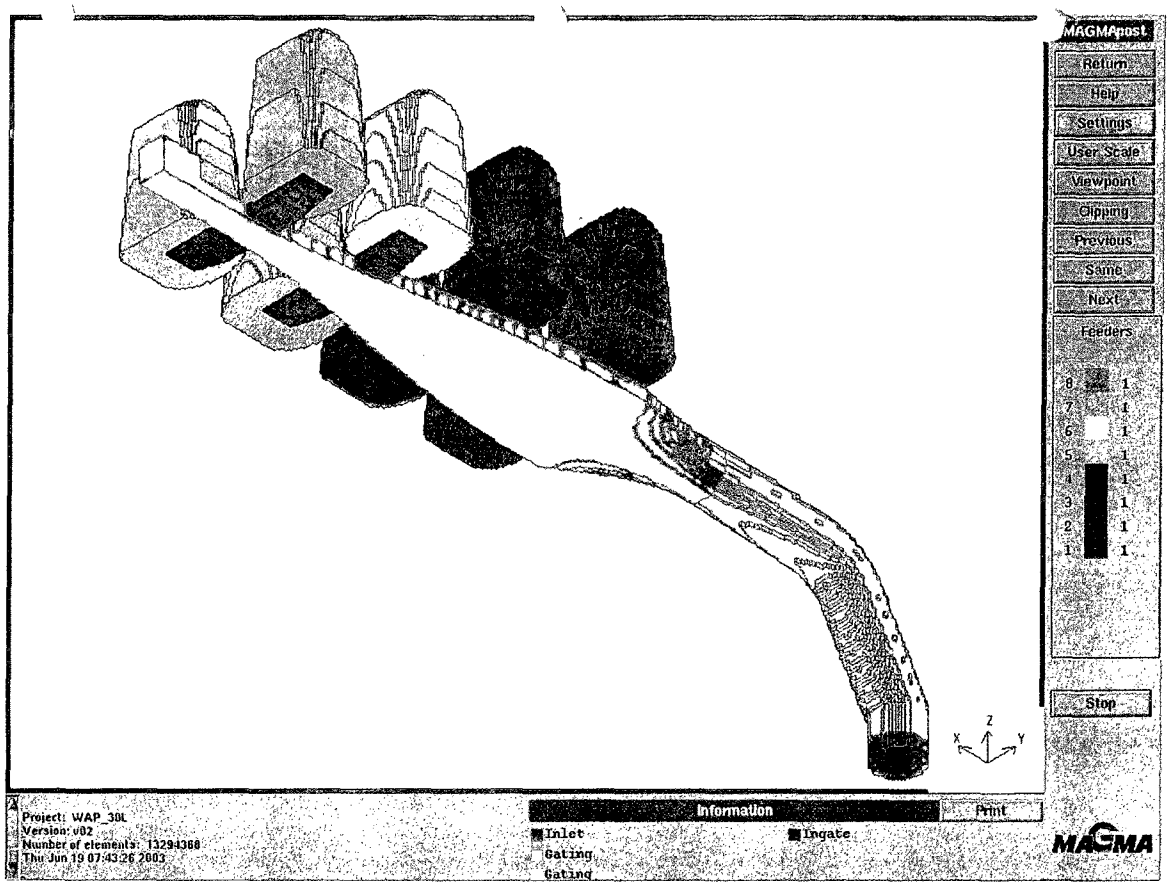

Figure A32: Solid Model of Sessile Runner Design.

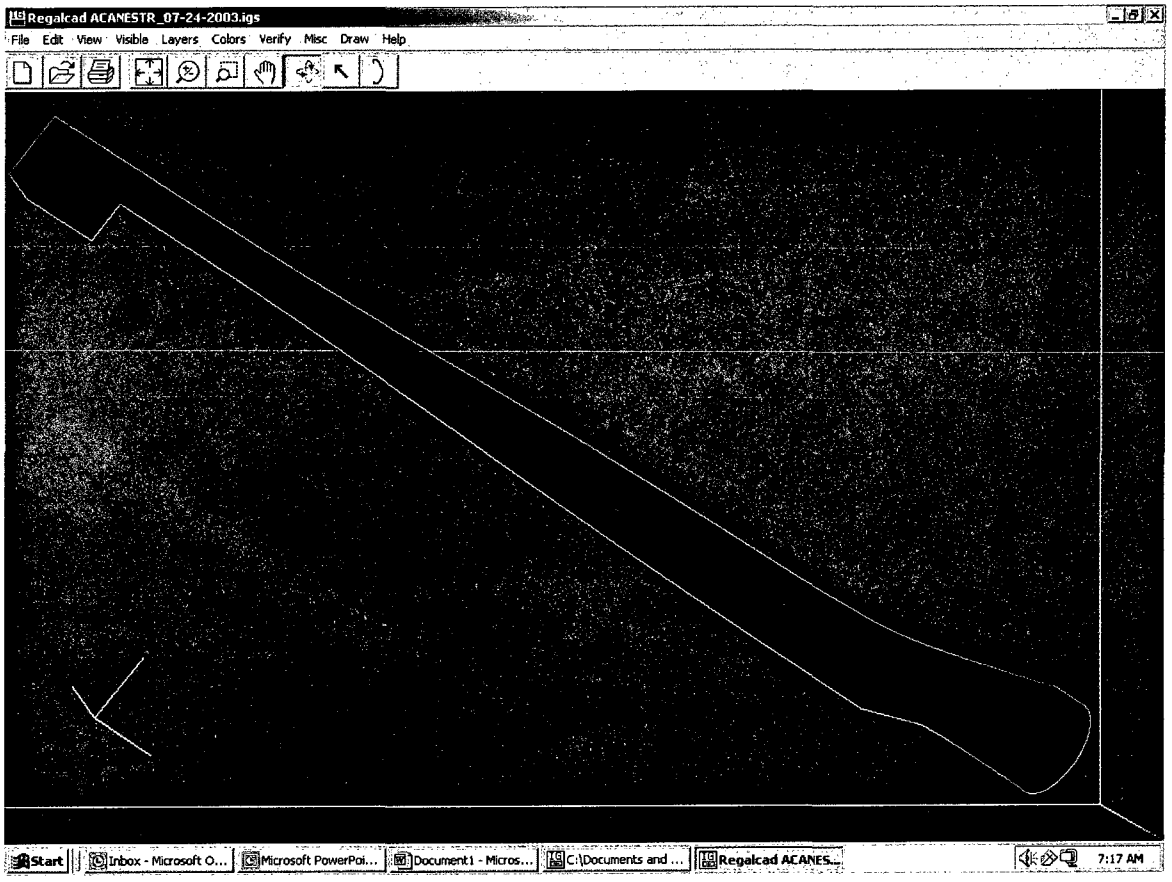

Figure A33: Sessile runner -view of bottom/right side.

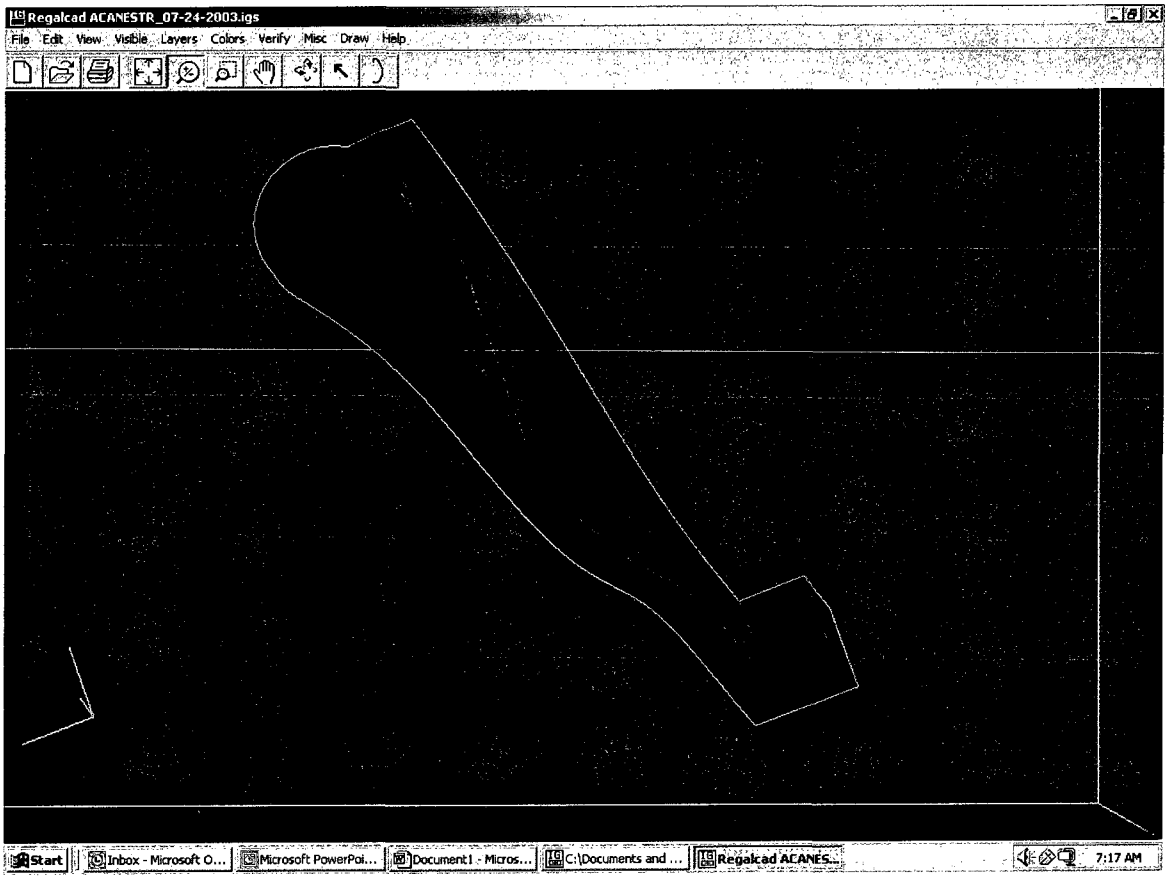

Figure A34: Sessile runner -view of top & right side.

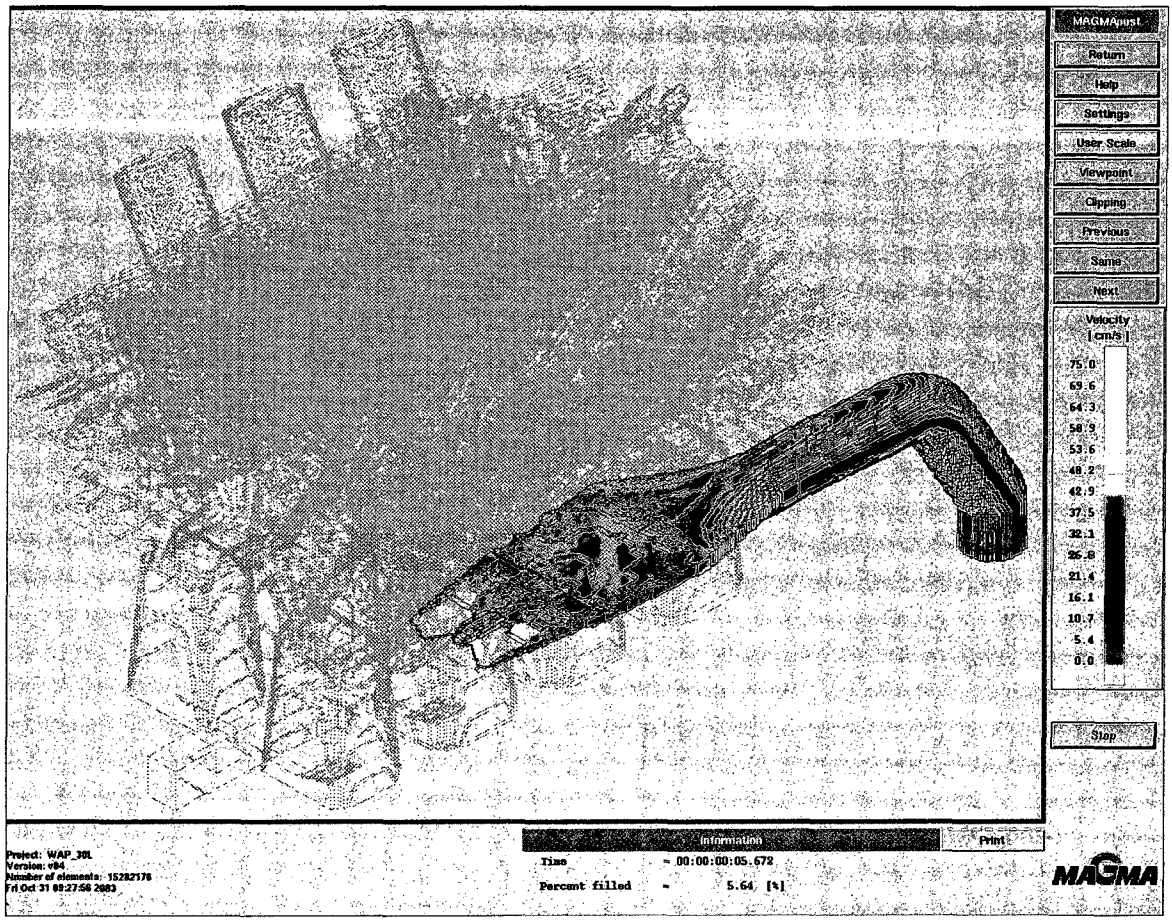

Figure A35: MAGMA 3.0L cylinder block fill simulation -sessile runner@ 5.7 seconds; $V_{IT} < V_{critical}$.

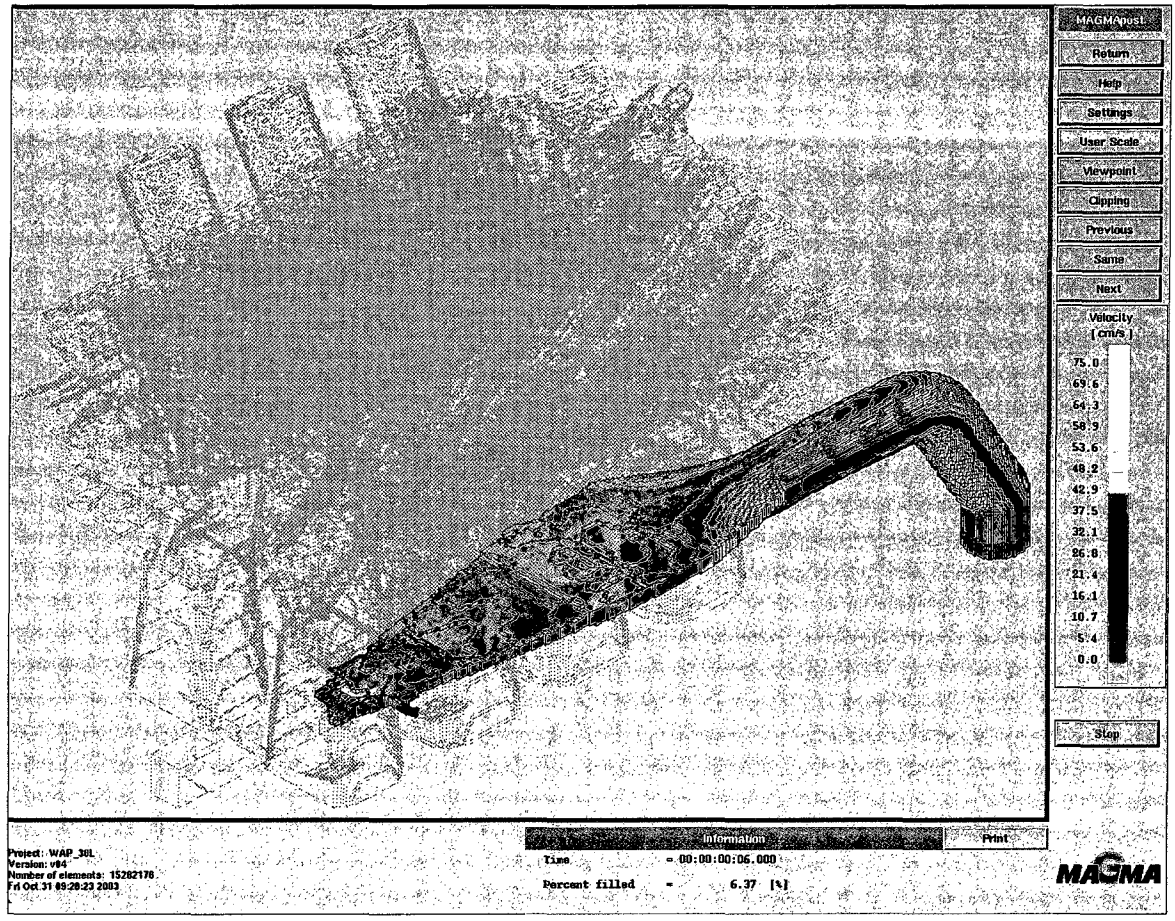

Figure A36: MAGMA 3.0L cylinder block fill simulation -sessile runner@ 6.0 seconds; $V_{IT} < V_{critical}$.

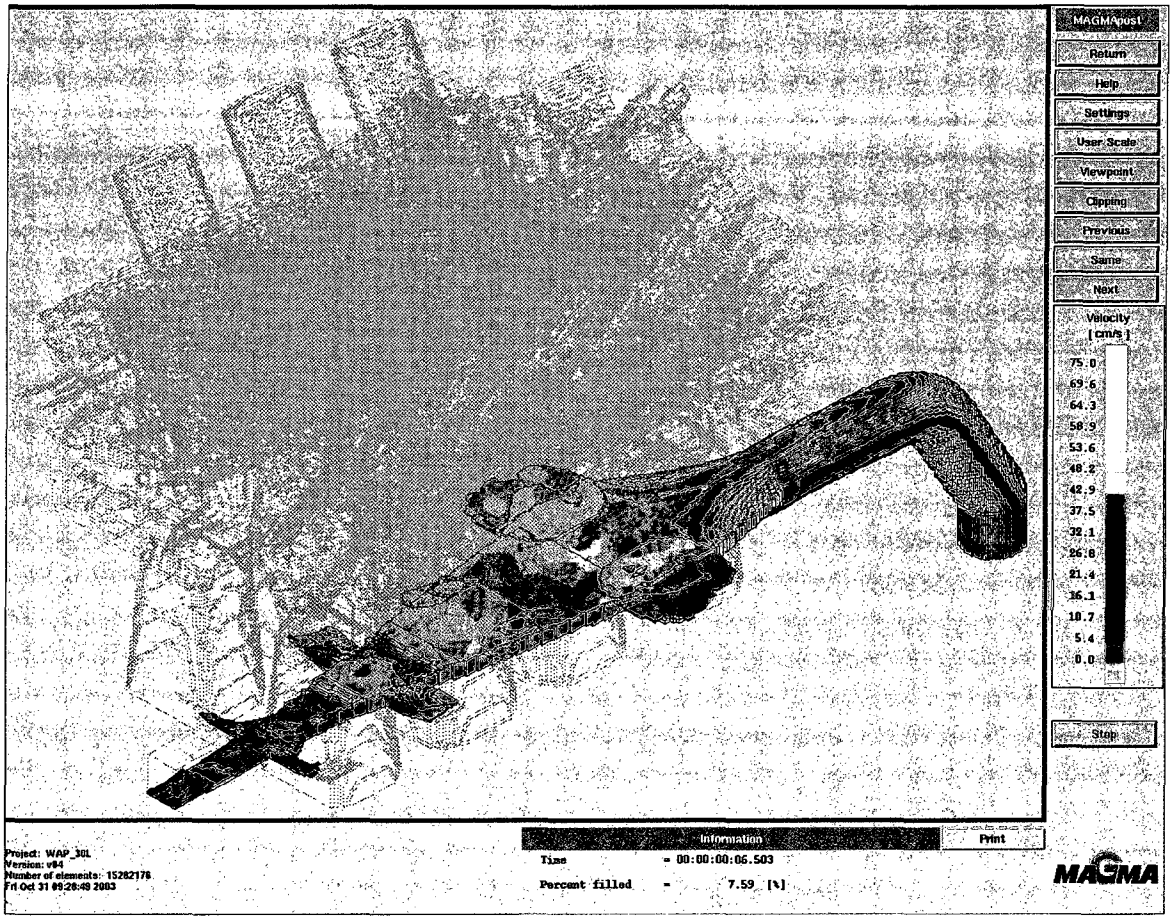

Figure A37: MAGMA 3.0L cylinder block fill simulation -sessile runner@ 6.5 seconds; $V_{IT} < V_{critical}$.

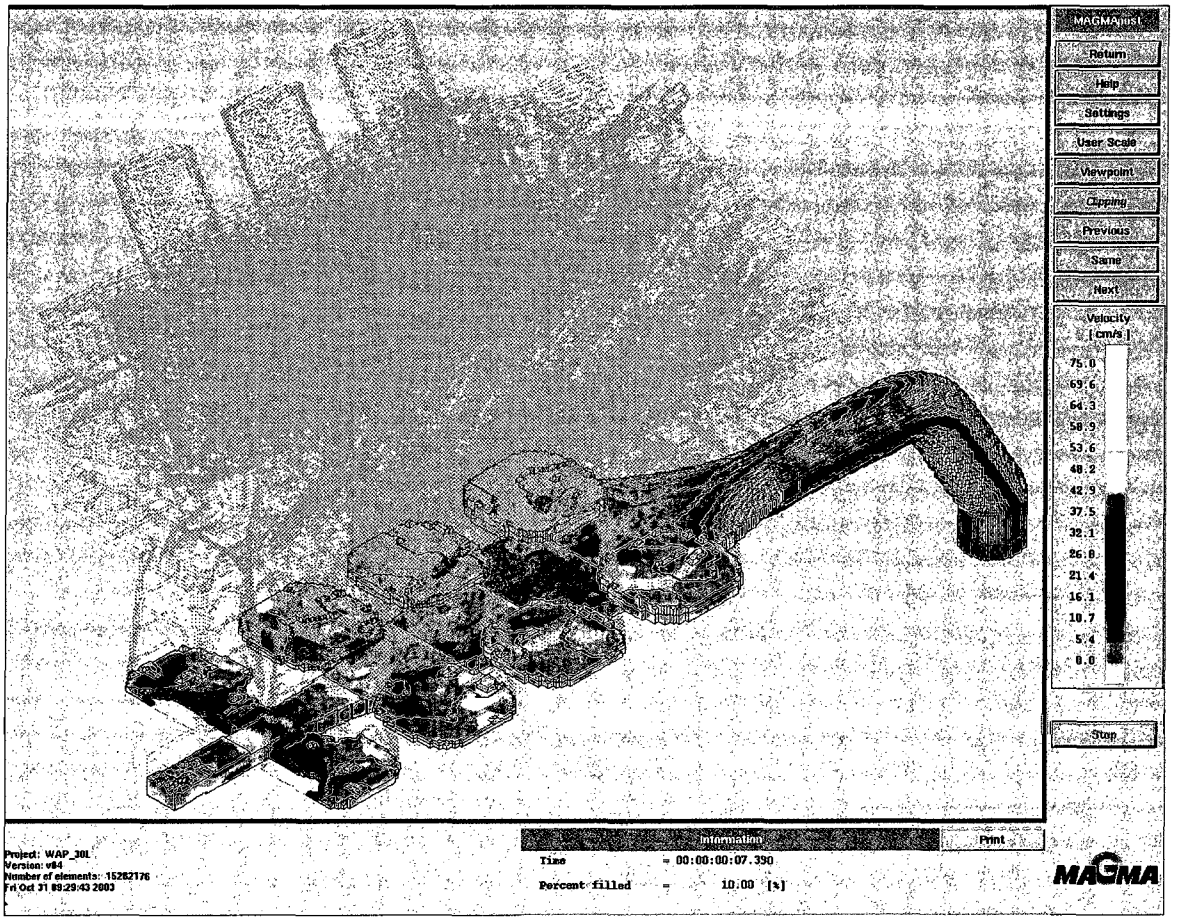

Figure A38: MAGMA 3.0L cylinder block fill simulation -sessile runner@ 7.0 seconds; $V_{IT} < V_{critical}$.

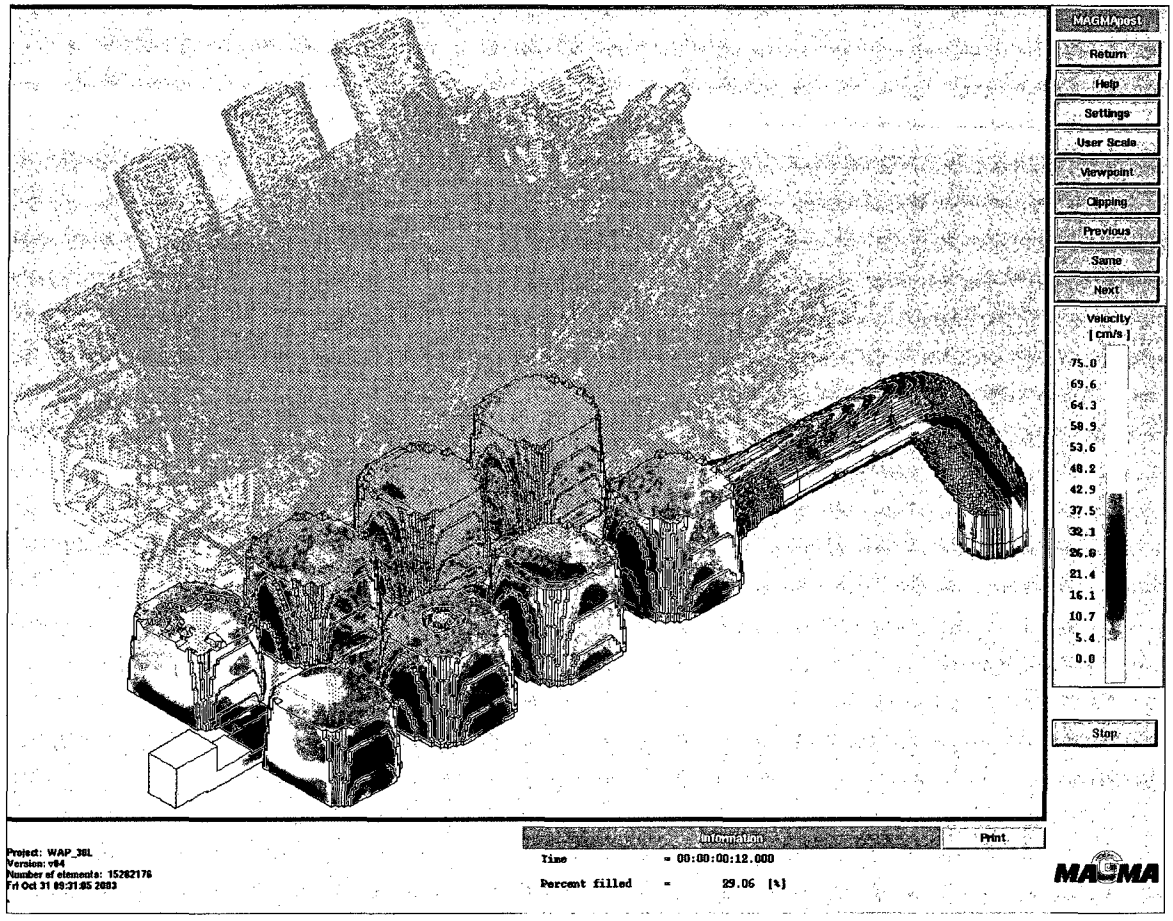

Figure A39: MAGMA 3.0L cylinder block fill simulation -sessile runner@ 12.2 seconds.

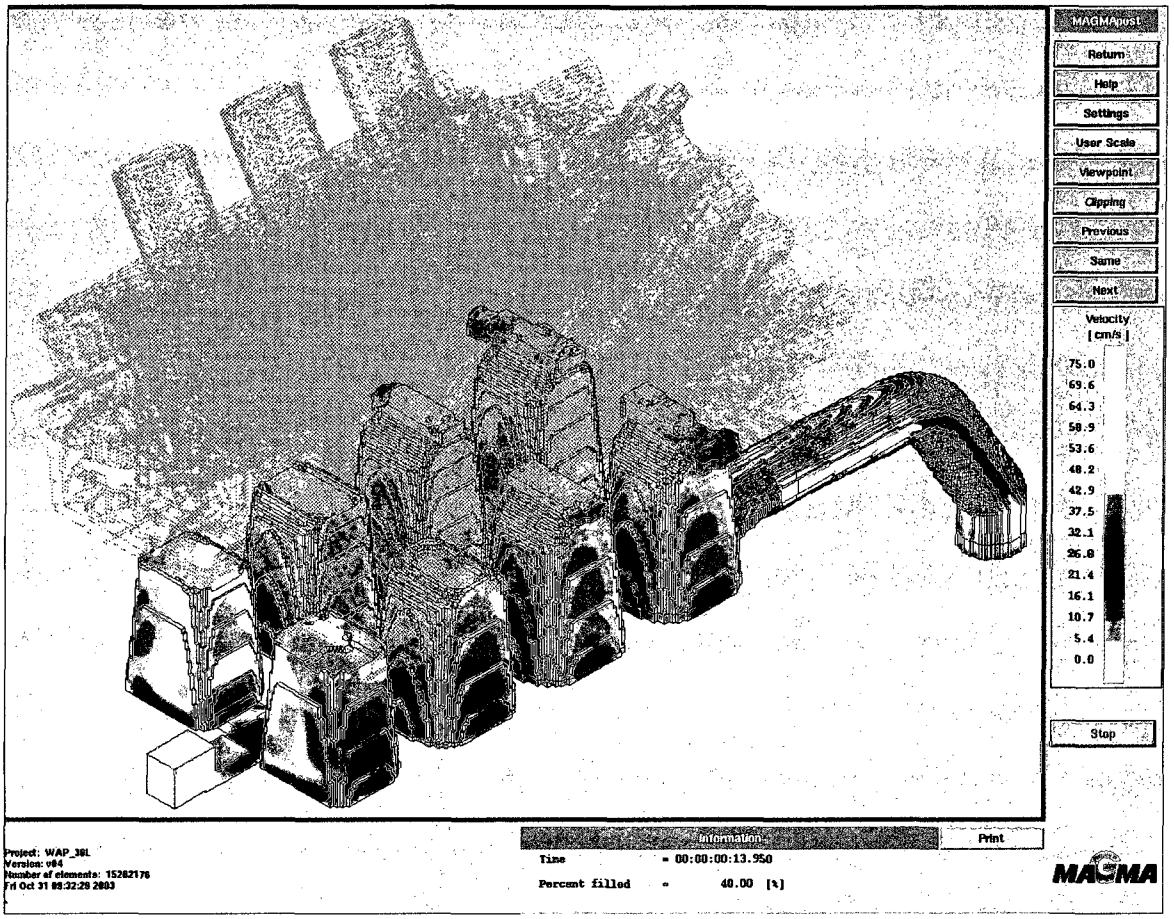

Figure A40: MAGMA 3.0L cylinder block fill simulation -sessile runner@ 13.9 seconds -No fountain effect.

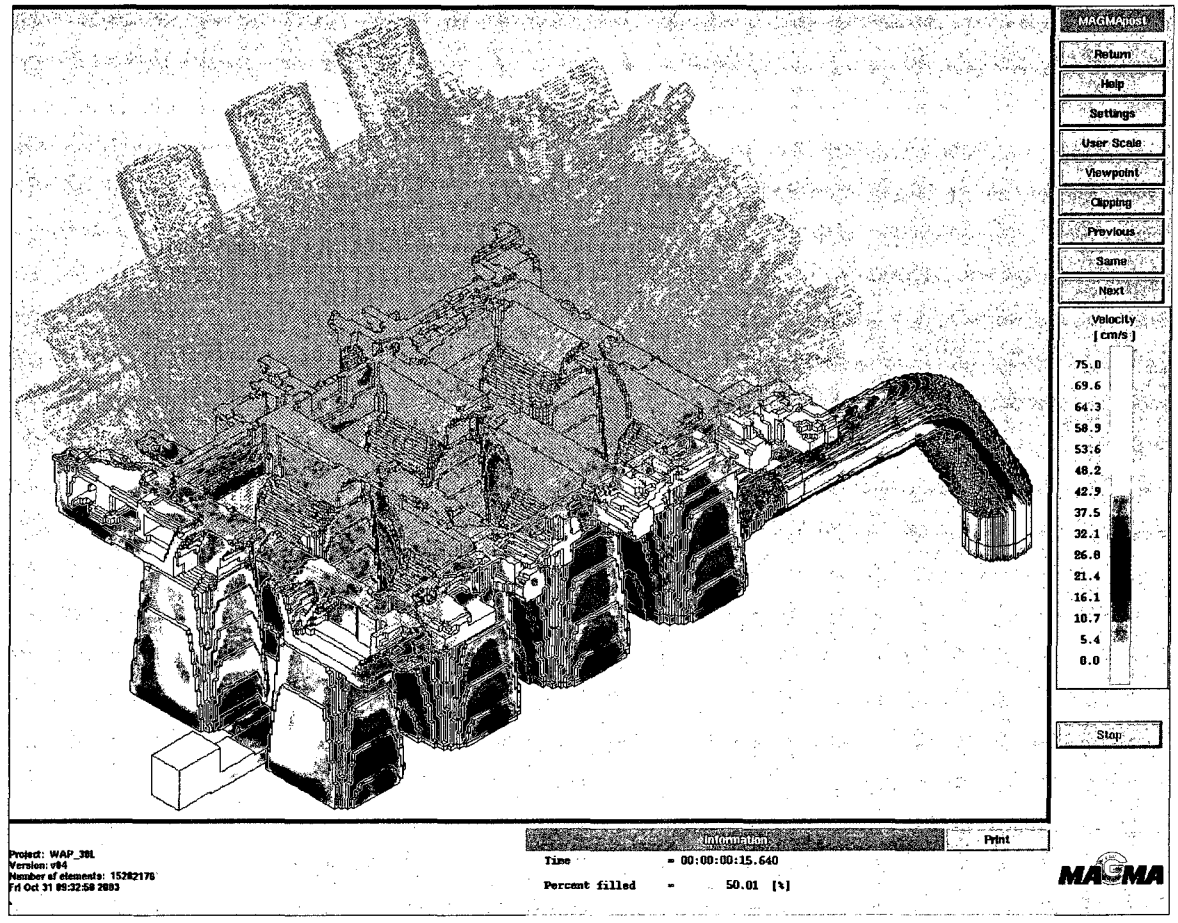

Figure A41: MAGMA 3.0L cylinder block fill simulation -sessile runner@ 15.6 seconds.

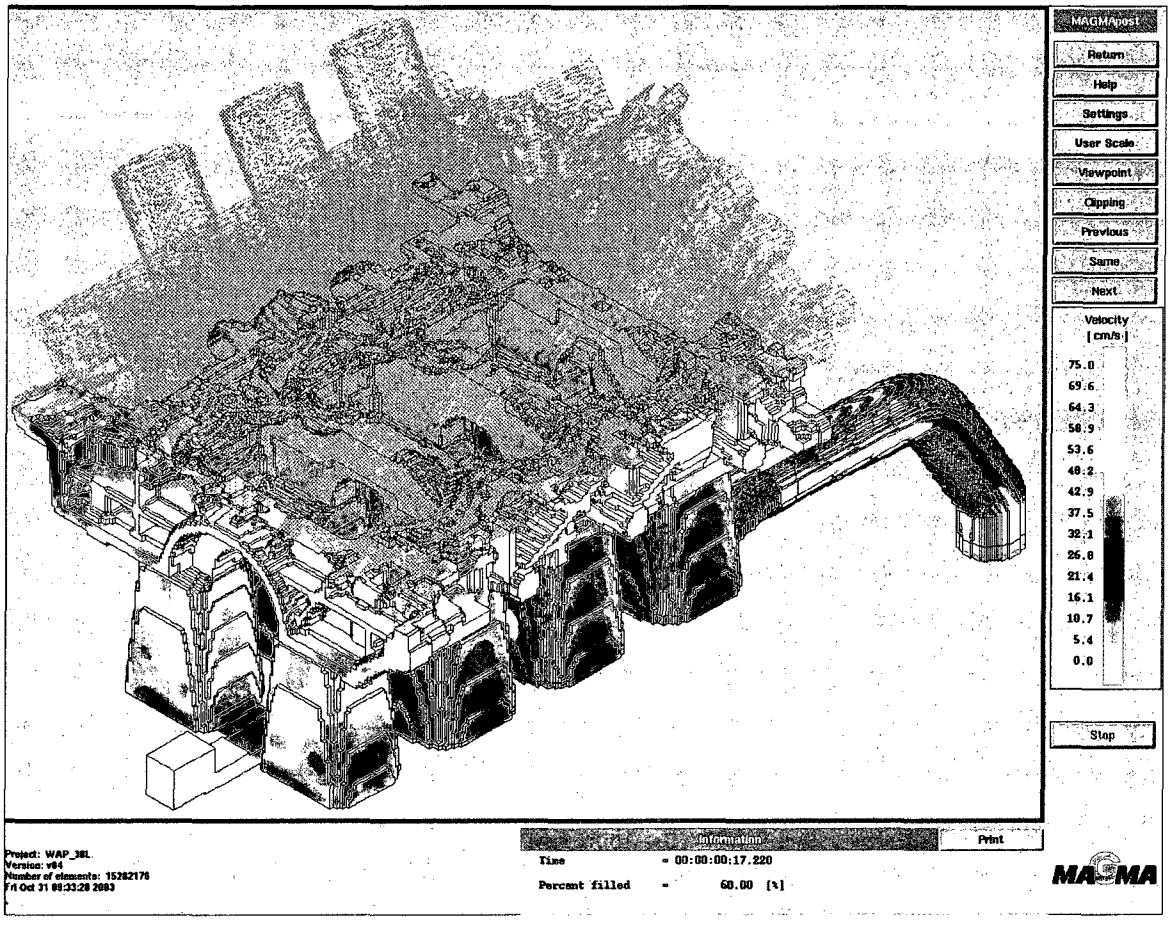

Figure A42: MAGMA 3.0L cylinder block fill simulation -sessile runner@ 17.2 seconds.

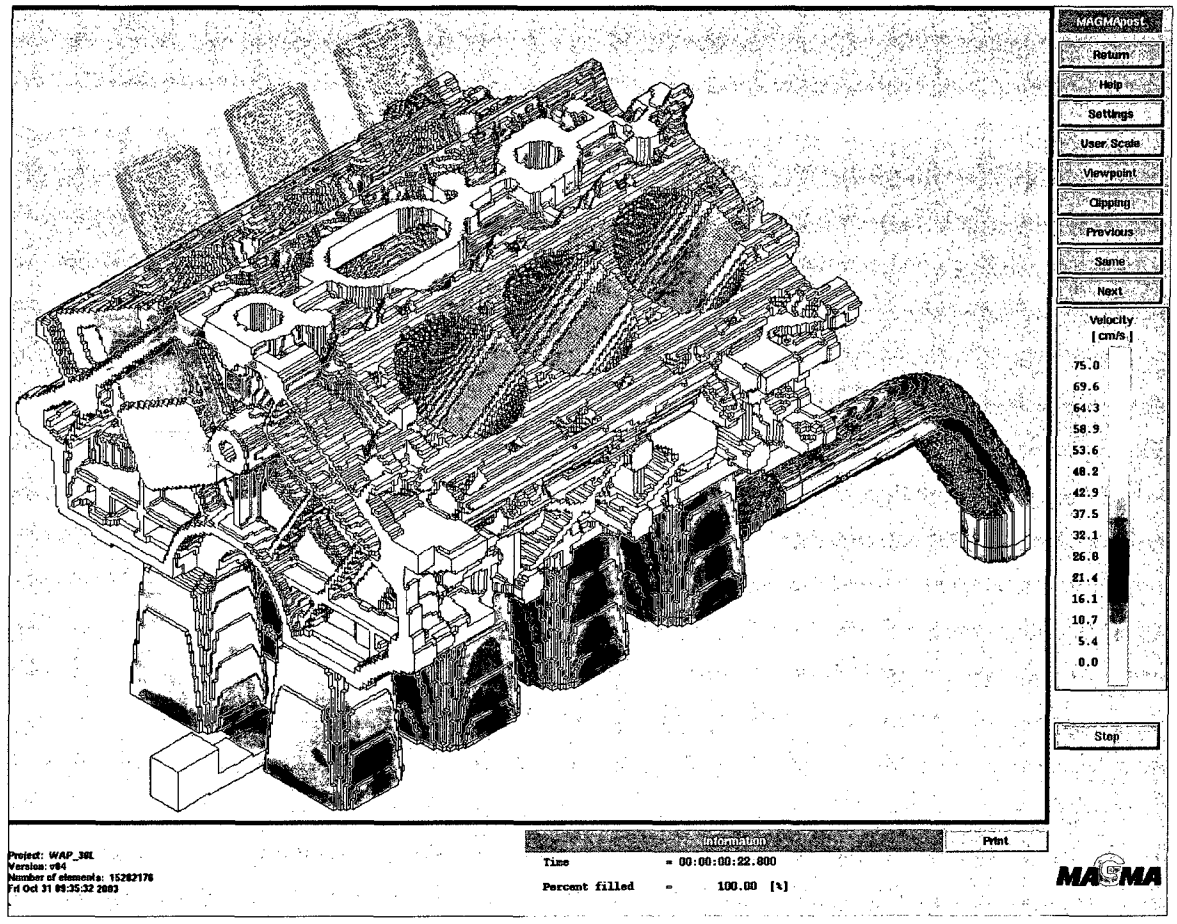

Figure A43: MAGMA 3.0L cylinder block fill simulation -sessile runner@ 22.8 seconds; Fill complete.

Appendix I
Weibull Modulus Calculations

Table A8: Weibull Modulus Calculations (A+B Samples).

UTS Phase I A+B samples (Modulus =28.9) — 23 samples

j		UTS	Ranked	F(j) = (j-0.5)/N	ln(x)	ln(ln(1/(1-F(j))))
1	1-1a	249.5	236.6	0.0217	5.4664	-3.8177
2	1-2a	255.2	243.9	0.0652	5.4968	-2.6965
3	1-3a	243.9	249.5	0.1087	5.5195	-2.1622
4	1-5a	257.3	255.2	0.1522	5.5420	-1.8013
5	1-7a	261.4	255.9	0.1957	5.5448	-1.5245
6	1-8a	270.3	257.3	0.2391	5.5502	-1.2972
7	1-12a	265.0	260.3	0.2826	5.5618	-1.1022
8	1-13a	255.9	260.7	0.3261	5.5634	-0.9297
9	1-14a	263.9	261.4	0.3696	5.5661	-0.7736
10	1-16a	260.7	263.9	0.4130	5.5756	-0.6296
11	1-18a	271.3	264.8	0.4565	5.5790	-0.4947
12	1-19a	272.4	265.0	0.5000	5.5797	-0.3665
13	1-20a	264.8	265.0	0.5435	5.5797	-0.2432
14	1-1b	273.8	268.9	0.5870	5.5943	-0.1231
15	1-2b	269.4	269.4	0.6304	5.5962	-0.0046
16	1-3b	284.7	270.3	0.6739	5.5995	0.1139
17	1-5b	236.6	271.3	0.7174	5.6032	0.2340
18	1-7b	278.0	271.6	0.7609	5.6043	0.3582
19	1-8b	271.6	272.4	0.8043	5.6073	0.4894
20	1-12b	276.7	273.8	0.8478	5.6124	0.6327
21	1-14b	268.9	276.7	0.8913	5.6229	0.7971
22	1-16b	260.3	278.0	0.9348	5.6276	1.0043
23	1-19b	265.0	284.7	0.9783	5.6514	1.3425

UTS Phase II A+B samples (Modulus =35.4) — 17 samples

j		UTS	Ranked	F(j) = (j-0.5)/N	ln(x)	ln(ln(1/(1-F(j))))
1	11-4a	244.3	235.2	0.0294	5.4604	-3.5115
2	11-5a	192.2	235.4	0.0882	5.4613	-2.3819
3	11-7a	252.5	238.5	0.1471	5.4744	-1.8384
4	11-8a	235.2	238.9	0.2059	5.4760	-1.4674
5	11-9a	254.7	243.9	0.2647	5.4968	-1.1793
6	11-11a	262.2	244.3	0.3235	5.4984	-0.9394
7	11-13a	252.4	248.1	0.3824	5.5138	-0.7301
8	11-14a	243.9	251.5	0.4412	5.5274	-0.5414
9	11-16a	238.9	251.6	0.5000	5.5278	-0.3665
10	11-1b	265.0	252.4	0.5588	5.5310	-0.2005
11	11-2b	238.5	252.4	0.6176	5.5310	-0.0394
12	11-5b	262.0	252.5	0.6765	5.5314	0.1209
13	11-6b	260.0	254.7	0.7353	5.5401	0.2845
14	11-7b	186.2	256.1	0.7941	5.5456	0.4577
15	11-8b	268.9	257.2	0.8529	5.5499	0.6507
16	11-9b	257.2	260.0	0.9118	5.5607	0.8870
17	11-11b	256.1	262.0	0.9706	5.5683	1.2603

UTS Phase III A+B samples (Modulus =27.7) — 29 samples

j		UTS	Ranked	F(j) = (j-0.5)/N	ln(x)	ln(ln(1/(1-F(j))))
1	111-1a	220.0	208.2	0.0172	5.3385	-4.0518
2	111-2a	226.8	209.9	0.0517	5.3466	-2.9354
3	111-3a	225.5	214.2	0.0862	5.3669	-2.4063
4	111-4a	238.2	216.0	0.1207	5.3753	-2.0509
5	111-6a	209.9	217.4	0.1552	5.3817	-1.7801
6	111-7a	227.5	217.9	0.1897	5.3840	-1.5592
7	111-8a	208.2	218.2	0.2241	5.3854	-1.3713
8	111-10a	217.4	218.6	0.2586	5.3872	-1.2065
9	111-11a	214.2	220.0	0.2931	5.3936	-1.0588
10	111-12a	223.1	220.4	0.3276	5.3954	-0.9241
11	111-13a	216.0	222.5	0.3621	5.4049	-0.7996
12	111-16a	218.2	223.1	0.3966	5.4076	-0.6830
13	111-17a	217.9	225.5	0.4310	5.4183	-0.5728
14	111-18a	220.4	225.9	0.4655	5.4201	-0.4677
15	111-19a	218.6	226.8	0.5000	5.4241	-0.3665
16	111-20a	237.7	227.5	0.5345	5.4272	-0.2684
17	111-1b	234.3	233.0	0.5690	5.4510	-0.1725
18	111-2b	234.3	233.8	0.6034	5.4545	-0.0780
19	111-3b	263.8	234.0	0.6379	5.4553	0.0158
20	111-4b	240.6	234.2	0.6724	5.4562	0.1098
21	111-6b	225.9	234.3	0.7069	5.4566	0.2048
22	111-7b	240.6	234.3	0.7414	5.4566	0.3019
23	111-8b	238.6	237.7	0.7759	5.4710	0.4025
24	111-10b	245.4	238.2	0.8103	5.4731	0.5084
25	111-11b	222.5	238.6	0.8448	5.4748	0.6223
26	111-12b	274.4	238.9	0.8793	5.4760	0.7488
27	111-13b	233.0	239.9	0.9138	5.4802	0.8965
28	111-16b	238.9	240.6	0.9483	5.4831	1.0858
29	111-17b	234.2	240.6	0.9828	5.4831	1.4013

Table A9: Weibull Modulus Calculations (A Samples).

UTS Phase I A samples (Modulus =34.4) 13 samples

j		UTS	Ranked	F(j) = (j-0.5)/N	ln(x)	ln(ln(1/(1-F(j))))
1	1-1a	249.5	236.6	0.0385	5.4664	-3.2386
2	1-2a	255.2	243.9	0.1154	5.4968	-2.0988
3	1-3a	243.9	249.5	0.1923	5.5195	-1.5438
4	1-5a	257.3	255.2	0.2692	5.5420	-1.1595
5	1-7a	261.4	255.9	0.3462	5.5448	-0.8559
6	1-8a	270.3	257.3	0.4231	5.5502	-0.5978
7	1-12a	265.0	260.3	0.5000	5.5618	-0.3665
8	1-13a	255.9	260.7	0.5769	5.5634	-0.1506
9	1-14a	263.9	261.4	0.6538	5.5661	0.0591
10	1-16a	260.7	263.9	0.7308	5.5756	0.2717
11	1-18a	271.3	264.8	0.8077	5.5790	0.5000
12	1-19a	272.4	265.0	0.8846	5.5797	0.7699
13	1-20a	264.8	265.0	0.9615	5.5797	1.1811

UTS Phase II A samples (Modulus =43.1) 9 samples

j		UTS	Ranked	F(j) = (j-0.5)/N	ln(x)	ln(ln(1/(1-F(j))))
1	11-4a	244.3	235.2	0.0556	5.4604	-2.8619
2	11-5a	192.2	235.4	0.1667	5.4613	-1.7020
3	11-7a	252.5	238.5	0.2778	5.4744	-1.1226
4	11-8a	235.2	238.9	0.3889	5.4760	-0.7083
5	11-9a	254.7	243.9	0.5000	5.4968	-0.3665
6	11-11a	262.2	244.3	0.6111	5.4984	-0.0571
7	11-13a	252.4	248.1	0.7222	5.5138	0.2476
8	11-14a	243.9	251.5	0.8333	5.5274	0.5832
9	11-16a	238.9	251.6	0.9444	5.5278	1.0614

UTS Phase III A samples (Modulus =47.7) 16 samples

j		UTS	Ranked	F(j) = (j-0.5)/N	ln(x)	ln(ln(1/(1-F(j))))
1	111-1a	220.0	208.2	0.0313	5.3385	-3.4499
2	111-2a	226.8	209.9	0.0938	5.3466	-2.3183
3	111-3a	225.5	214.2	0.1563	5.3669	-1.7726
4	111-4a	238.2	216.0	0.2188	5.3753	-1.3989
5	111-6a	209.9	217.4	0.2813	5.3817	-1.1079
6	111-7a	227.5	217.9	0.3438	5.3840	-0.8646
7	111-8a	208.2	218.2	0.4063	5.3854	-0.6514
8	111-10a	217.4	218.6	0.4688	5.3872	-0.4580
9	111-11a	214.2	220.0	0.5313	5.3936	-0.2775
10	111-12a	223.1	220.4	0.5938	5.3954	-0.1045
11	111-13a	216.0	222.5	0.6563	5.4049	0.0656
12	111-16a	218.2	223.1	0.7188	5.4076	0.2378
13	111-17a	217.9	225.5	0.7813	5.4183	0.4186
14	111-18a	220.4	225.9	0.8438	5.4201	0.6186
15	111-19a	218.6	226.8	0.9063	5.4241	0.8617
16	111-20a	237.7	227.5	0.9688	5.4272	1.2429

Table A10: Weibull Modulus Calculations (B Samples).

UTS Phase I B samples (Modulus =59.2) 10 samples

j		UTS	Ranked	F(j) = (j-0.5)/N	ln(x)	ln(ln(1/(1-F(j))))
1	1-1b	273.8	268.9	0.0500	5.5943	-2.9702
2	1-2b	269.4	269.4	0.1500	5.5962	-1.8170
3	1-3b	284.7	270.3	0.2500	5.5995	-1.2459
4	1-5b	236.6	271.3	0.3500	5.6032	-0.8422
5	1-7b	278.0	271.6	0.4500	5.6043	-0.5144
6	1-8b	271.6	272.4	0.5500	5.6073	-0.2250
7	1-12b	276.7	273.8	0.6500	5.6124	0.0486
8	1-14b	268.9	276.7	0.7500	5.6229	0.3266
9	1-16b	260.3	278.0	0.8500	5.6276	0.6403
10	1-19b	265.0	284.7	0.9500	5.6514	1.0972

UTS Phase II B samples (Modulus =76.2) 8 samples

j		UTS	Ranked	F(j) = (j-0.5)/N	ln(x)	ln(ln(1/(1-F(j))))
1	11-1b	265.0	252.4	0.0625	5.5310	-2.7405
2	11-2b	238.5	252.4	0.1875	5.5310	-1.5720
3	11-5b	262.0	252.5	0.3125	5.5314	-0.9816
4	11-6b	260.0	254.7	0.4375	5.5401	-0.5528
5	11-7b	186.2	256.1	0.5625	5.5456	-0.1903
6	11-8b	268.9	257.2	0.6875	5.5499	0.1511
7	11-9b	257.2	260.0	0.8125	5.5607	0.5152
8	11-11b	256.1	262.0	0.9375	5.5683	1.0198

UTS Phase III B samples (Modulus =91.7) 13 samples

j		UTS	Ranked	F(j) = (j-0.5)/N	ln(x)	ln(ln(1/(1-F(j))))
1	111-1b	234.3	233.0	0.0385	5.4510	-3.2386
2	111-2b	234.3	233.8	0.1154	5.4545	-2.0988
3	111-3b	263.8	234.0	0.1923	5.4553	-1.5438
4	111-4b	240.6	234.2	0.2692	5.4562	-1.1595
5	111-6b	225.9	234.3	0.3462	5.4566	-0.8559
6	111-7b	240.6	234.3	0.4231	5.4566	-0.5978
7	111-8b	238.6	237.7	0.5000	5.4710	-0.3665
8	111-10b	245.4	238.2	0.5769	5.4731	-0.1506
9	111-11b	222.5	238.6	0.6538	5.4748	0.0591
10	111-12b	274.4	238.9	0.7308	5.4760	0.2717
11	111-13b	233.0	239.9	0.8077	5.4802	0.5000
12	111-16b	238.9	240.6	0.8846	5.4831	0.7699
13	111-17b	234.2	240.6	0.9615	5.4831	1.1811

Appendix J
Uncertainty Analysis

Table A11: Analysis of Uncertainty in Velocity Calculations.

Uncertainty Analysis for V_{IT}

Precision of distance measuremet = +/- 0.5mm = +/-.0005m

Precision of time measurement = +/-.05s

	Dist to probe from 0 (m)	Cumulative time to probe (s)	Average Velocity to Probe (ms-1)	Distance Measurement Error (m)	Time Measurement Error (s)	Measurement Error (ms^{-1})	Percent Error in Velocity
Phase I Measurement 1	0.000	0.0	0.0	0.000000	0.000000	0.000	0.0%
Phase I Measurement 2	0.145	0.2	0.7	0.000012	0.062500	0.182	25.0%
Phase I Measurement 3	0.263	0.4	0.7	0.000004	0.015625	0.082	12.5%
Phase I Measurement 4	0.369	0.5	0.7	0.000002	0.010000	0.074	10.0%
Phase I Measurement 5	0.468	0.7	0.7	0.000001	0.005102	0.048	7.1%
Phase I Measurement 6	0.541	0.8	0.7	0.000001	0.003906	0.042	6.3%
Phase I Measurement 1	0.000	0.0	0.0	0.000000	0.000000	0.000	0.0%
Phase I Measurement 2	0.147	0.2	0.7	0.000012	0.062500	0.184	25.0%
Phase I Measurement 3	0.284	0.3	0.9	0.000003	0.027778	0.158	16.7%
Phase I Measurement 4	0.412	0.4	1.0	0.000001	0.015625	0.129	12.5%
Phase I Measurement 5	0.533	0.5	1.1	0.000001	0.010000	0.107	10.0%
Phase III Measurement 1	0.000	0.0	0.0	0.000000	0.000000	0.000	0.0%
Phase III Measurement 2	0.126	0.3	0.4	0.000016	0.027778	0.070	16.7%
Phase III Measurement 3	0.254	0.6	0.4	0.000004	0.006944	0.035	8.3%
Phase III Measurement 4	0.395	1.1	0.4	0.000002	0.002066	0.016	4.5%
Phase III Measurement 5	0.523	1.6	0.3	0.000001	0.000977	0.010	3.1%

Claim of Intellectual Property

The concepts listed below represent original thinking used in the planning and execution of the experimentation performed in this work. The author claims ownership of these concepts as intellectual property;

1. "Timer Package" concept.
2. "Timer Package" data collection device and associated software.
3. Copper chill plate assembled onto runner mould for purpose of capturing entrained defects.
4. Mould holding fixture adjustable to facilitate variable flow velocity

Vita Auctoris

Name: John Christopher Burford

Place of Birth: Windsor Ontario, Canada

Year of Birth: 1955

Education:

University of Windsor, Windsor, Ontario, Canada
Department of Mechanical materials and Automotive Engineering
M.A.Sc. Engineering Materials
June 2006

University of Windsor, Windsor, Ontario, Canada
Department of Education
B.Ed. Intermediate/Senior Math and Science
June 1990

University of Windsor, Windsor, Ontario, Canada
Department of Mechanical Engineering
B.A.Sc. Mechanical Engineering
June 1979

Assumption High School, Windsor Ontario, Canada
1968 - 1973